Laser Processing of Ga_2O_3 Micro- and Nanostructures

Lam Hwee Ming, Jenny

School of Materials Science and Engineering

A thesis submitted to the Nanyang Technological University
in fulfilment of the requirement for the degree of
Doctor of Philosophy

2007

ACKNOWLEDGEMENTS

First and foremost, I would like to express my utmost gratitude and appreciation to both my supervisors, Dr. Gan Chee Lip (MSE, NTU) and Dr. Ong Teng San (DSI) for their valuable advice, patience and constant guidance in many areas of my research. Despite their busy schedules, they have often found time to answer my questions and review my work.

In particular, I want to thank Dr. Dong Zhili (MSE, NTU) and Dr. Tang Xiaohong (EEE, NTU) for taking the time to go through my thesis with me as well as giving me their helpful and insightful viewpoints on my work.

Special thanks to Dr. Yuan Shu and Dr. Hong Minghui for their past support and assistance in this project to make this work a smooth and beneficial experience. Part of the major contributions and results obtained in this study would not be achieved without the collaborative effort and vibrant discussions with many people. For that, I would like to thank all research staff, technical staff and students from the Electronics and Magnetic Materials laboratory, NTU and DSI Laser laboratory, particularly Dr. Liu Chongyang, Dr. Song Wendong, Dr. Wu Dongjiang, Ms Lin Ying, Dr. Chen Guoxin, Dr. Wang Zengbo, Ms Van Li Hui and Mr Lan Bin for their help and friendship.

I am deeply grateful to my family and close friends, especially Xie Jing, Christine Choo, Lydia Yeo and Inez Ang for believing in me and giving me continual support and encouragement throughout this challenging journey that requires much mental strength and perseverance. Finally, I thank my Lord and savior Jesus Christ for granting me the opportunity to embark on this project and the wisdom and strength to overcome all obstacles and challenges to complete this project in due time.

TABLE OF CONTENTS

ABSTRACT

A novel synthesis route has been developed for the growth of monoclinic Ga_2O_3 nanoparticles, nanoclusters and nanowires by pulsed laser ablation of GaN (99.99% purity), using pulsed KrF excimer laser (λ = 248 nm). Room-temperature synthesis of Ga_2O_3 nanoparticles and nanoclusters was carried out in N_2 or O_2 gas ambient. The effects of laser fluence, deposition pressure, deposition ambient on the size, shape, degree of aggregation and crystallinity of the as-deposited products were studied accordingly. Transmission electron microscopy (TEM) results revealed an aggregation of Ga_2O_3 nanoparticles that proceeds one-dimensionally to form chain-like nanostructures. The relatively spherical nanoparticles typically have diameters of 8.5nm and 6.5 nm when deposited at 10 Torr in N_2 and O_2 ambient respectively. Next, optical properties, including photoluminescence (PL) and absorption in the UV-visible range of the as-deposited Ga_2O_3 nanoparticles and nanoclusters were studied in great detail. It is evident from the PL studies that the Ga_2O_3 nanoparticles and nanoclusters exhibit blue and UV luminescence at 2.65 eV and around 3.41 to 3.44 eV respectively. In addition, significant blueshift of the absorption edge was also observed. The blueshift of the absorption edge is attributed to strong quantum confinement effects.

Next, a study of the effect of KrF excimer (λ = 248 nm) laser annealing on the crystallinity and photoluminescence of amorphous Ga_2O_3 nanoparticles was performed. In KrF excimer laser annealing, morphological changes from one-dimensional chain-like nanostructure to grain-like and film-like morphologies were observed with increasing laser fluence. Significant surface melting was also observed on Ga_2O_3 samples when annealed at a laser fluence of 80 mJ/cm^2. The effect of laser

annealing on the PL emission of Ga_2O_3 nanoparticles and nanoclusters was also investigated. By optimizing the laser annealing conditions, Ga_2O_3 nanomaterials with high crystallinity and tailored PL emissions can be achieved.

Ga_2O_3 nanowires were successfully synthesized via a low temperature growth (600-800°C) method, initiated by pulsed laser ablation of GaN. Diameter and length control of the Ga_2O_3 nanowires were achieved by varying the growth conditions such as growth pressure, growth temperature and laser fluence. FESEM and TEM images revealed that the nanowires have diameters ranging from 30-100 nm and lengths of up to several microns. Photoluminescence spectrum of the nanowires shows blue and ultraviolet (UV) emission at 2.65 eV and around 3.42 to 3.44 eV respectively. In this work, the growth process of β-Ga_2O_3 nanowires has been interpreted as vapor-liquid-solid (VLS) mechanism. Various metal catalysts including Au, Ag and Pd have been shown to be effective catalysts for the growth of β-Ga_2O_3 nanowires and nanotubes in this work. Amongst Au, Pd and Ag, Pd-catalyzed β-Ga_2O_3 nanowires displays the smallest diameter, while Ag catalyst aids in the formation of Ga_2O_3 nanotubes.

In conclusion, this study has successfully demonstrated that pulsed laser ablation of GaN is a viable and effective method for the growth of Ga_2O_3 nanoparticles, nanoclusters and nanowires for potential applications in the exciting new field of nanodevices such as UV detectors and gas sensors.

LIST OF FIGURES

LIST OF TABLE

CHAPTER 1

Introduction

1.1 Nanotechnology

The advancement of science and technology over the last decade has unleashed new areas of scientific research and exploration that cross the borders between physical sciences and engineering. One of which is the rapidly expanding interest and research in nanotechnology. Nanotechnology analyses and manipulates materials, devices and systems on a nanoscale regime. Nanoscale materials have fascinated scientists as it has made their dream of tailoring materials according to their requirement much closer to reality, with instruments to observe and manipulate materials at such minute scale. Nanoscale materials can be defined as systems in which their dimensions are less than or equal to 100 nm and they include 0-dimensional (D) (e.g. quantum dots [1]), 1-D (e.g. nanotubes and nanowires [2]) and 2-dimensional (e.g. quantum wells [3]) nanostructures. A distinctive feature of nanoscale material in comparison to bulk material is the quantum confinement effect due to reduced size and/or dimensionality. Dimensionality plays a significant role in determining the electronic and optical properties of nanoscale materials due to the different electron interactions in low dimensional structures. For this reason, tremendous effort has been made to fabricate nanoscale materials and devices as the desirable properties of the nanoscale materials can be achieved by the control of dimension, size, morphology and composition, often achieved by using physical or chemical synthesis methods.

Many different routes have led to successful synthesis of various nanoscale material systems such as carbon [4], oxides [5], nitrides [6] and semiconductors [7]. Synthesis routes such as gas condensation [8], chemical precipitation including

colloidal sol solution [9] and reversed micelle methods [10], synthesis in matrices such as glass [11] and polymers [12], chemical vapor deposition [13], metal-catalyzed growth assisted by laser [14], metal-organic chemical vapor deposition (MOCVD) [15], template confined growth [16] and solvothermal [17] techniques have successfully fabricated various semiconductor nanoparticles and nanowires. However, these established synthesis methods for the growth of semiconductor nanoparticles and nanowires suffer from several drawbacks such as a complex process control, purity of materials produced, limitations to specific materials systems, particle size distribution and/or low yield. Therefore, there is an incentive to find new methods of synthesis as well as to overcome some limitations in the current synthesis methods, so that high quality growth of semiconductor nanoparticles and nanowires can be attained.

Pulsed laser ablation (PLA) is a promising technique of producing nanoscale materials. This method employs a high-intensity laser pulse to remove material from a target in a vapor/plasma plume. The plume material re-condenses and is subsequently collected on a cooled substrate. PLA for nanoparticle and nanowire growth has many advantages: (i) the energy source (laser) is outside the vacuum chamber which, in contrast to vacuum-installed equipment, provides a much greater degree of flexibility in materials use and geometrical arrangements; (ii) almost any condensed matter material can be ablated; (iii) a much larger flux of evaporated material can be created; (iv) the amount of evaporated source material is localized only to that defined by the laser focus; (v) plumes of evaporated materials with stoichiometry congruent to the target even for complex chemical systems can be produced; (vi) the ability to produce species with electronic states far from chemical equilibrium opens up the potential to produce novel or metastable materials that would be unattainable under equilibrium

conditions; (vii) fast and easy control. Thus, PLA offers a fast, high-yield and versatile process that introduces little or no contaminants and synthesizes equilibrium or non-equilibrium materials with complex chemical structures. In this study, a novel synthesis route for the growth of Ga_2O_3 nanoparticles, nanoclusters and nanowires via PLA of GaN is developed for the first time.

1.2 Crystal Structure of Ga_2O_3

Ga_2O_3 has been reported to have five allotropes: α, β, γ, δ and ε [18-22]. However, β-Ga_2O_3 is the only stable crystalline modification [21, 22], whereas all the other polymorphs are metastable and transform to the β form at sufficiently high temperatures. Table 1-1 summarizes the crystal lattice of the Ga-O system. β-Ga_2O_3 belongs to the monoclinic system, space group *C2/m* [23], with lattice parameters a = 12.23 Å, b = 3.04 Å, c = 5.80 Å and β = 103.7°. Figure 1-1 illustrates three different oxygen sites, denoted as O(1), O(2) and O(3), and two Ga sites, Ga(1) and Ga(2) of β-Ga_2O_3. The co-ordinations are 3-fold for O(1) and O(3), 4-fold for O(2) and Ga(1) and 6-fold for Ga(2). The symmetry is depicted in Fig. 1-1 which shows the projections along the 3 crystallographic axis. It presents 2 cleavage planes: the main (100) plane corresponding to the plane formed by O(3) atoms and the secondary (001) plane that is linked to the O(1) atoms. The natural habits of β-Ga_2O_3 have been reported as prismatic, rod or needle and platelets [24]. The growth mainly takes place along the b-axis, where O and Ga atoms are aligned, respectively. Beside the (010) plane, other planes of preferred growth such as (101), (110), $(\bar{1}01)$ planes have been proposed [25]. More recently, other growth directions like $(21\bar{2})$ and (111) have been observed for β-Ga_2O_3 nanosheets [26] and nanorods [27].

Table 1-1 Solid Phases in the Ga-O System [28].

Phase	Composition (at % O)	Pearson symbol	Space Group	Prototype	Lattice parameters (nm, deg)
α-Ga_2O_3[#]	60	*hR*30	$R\bar{3}c$	α-Al_2O_3	a = 0.49791 (6) c = 1.3437 (4)
β-Ga_2O_3	60	*mC*20	*C*2/*m*	β-Ga_2O_3	a = 1.2214(3) b = 0.30371 (9) c = 0.57981 (9) β = 103.7
γ-Ga_2O_3[#]	60	*cF*56	$Fd\bar{3}m$	Al_2MgO_4	a = 0.822
δ-Ga_2O_3[#]	60	*cI*80	$Ia\bar{3}$	Tl_2O_3	a = 1.000
ε-Ga_2O_3[#]	60	*oP*40	*Pna*2$_1$	κ- Al_2O_3	
Ga_2O	33.3			Amorphous	

[#]Metastable phase.

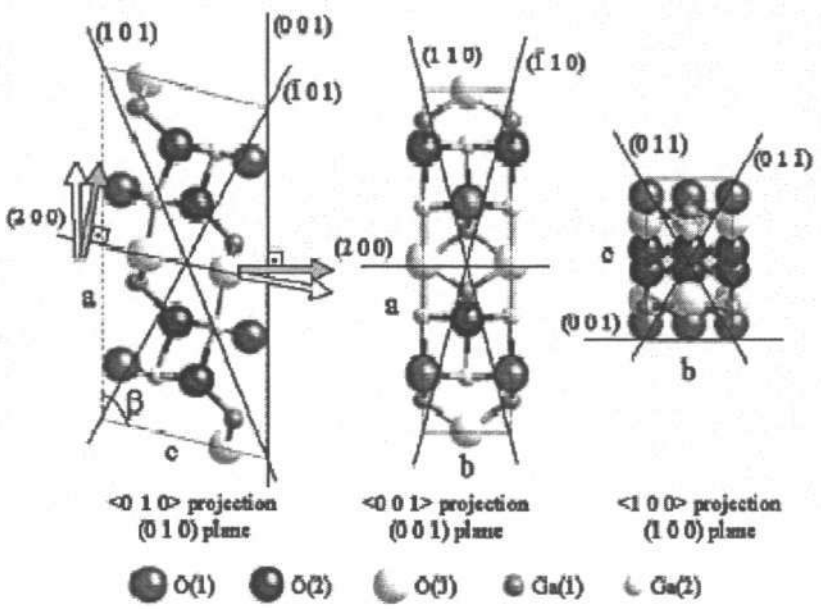

Figure 1-1 Projections of the β-Ga_2O_3 unit cell along the *b*-(left), *c*-(middle) and *a*-axis (right) [24].

1.2.1 Gallium oxide Bulk Crystal and Thin Film

Monoclinic gallium oxide (β-Ga_2O_3) is a wide bandgap semiconductor material ($E_g \approx 4.9$ eV) [29] that exhibits conduction [30, 31] and luminescence properties [32]. Due to its transparency from the visible into the UV region, it is a very promising candidate for optoelectronic devices operating at short wavelengths [33]. The electrical conductivity of β-Ga_2O_3 is attributed to oxygen vacancies. The amount of oxygen vacancies induced depends mainly on the growth conditions, and the electrical conductivity varies from insulating to n-type semiconducting. β-Ga_2O_3 bulk single crystals have been grown using the float zone [34] and Verneuil [35] methods.

Many techniques have also been employed to prepare Ga_2O_3 thin films, e.g. evaporation [36], sol-gel [37], sputtering [38-40], pulsed laser deposition [41], molecular beam epitaxy [42], metal organic chemical vapor deposition (MOCVD) [43] and oxidation of surfaces of GaAs [44]. In particular, Ga_2O_3 thin films are grown on Si (100) [45], (111) [46] and sapphire substrates by MOCVD. The growth rate and surface roughness of Ga_2O_3 thin films increases with increasing growth temperature at 500-600°C. Ji *et al.* has also demonstrated the deposition of Ga_2O_3 on quartz substrates by spray pyrolysis techniques for filter and solar blind UV detectors [47]. In general, the deposited Ga_2O_3 thin films are typically annealed between 750-1050°C to attain the most stable monoclinic phase of Ga_2O_3 for device applications [46].

Photoluminescence (PL) spectra of β-Ga_2O_3 thin films show blue-green emission at 470 nm (2.645 eV) and an ultraviolet emission at 365 nm (3.405 eV) [46]. Therefore, it has useful application as luminescent phosphors because of its interesting luminescence properties [48]. Due to its high bandgap, Ga_2O_3 thin films can be used as a deep UV transparent conducting oxide [49], antireflection coating for

GaAs [50], and passivation coating [29]. Furthermore, β-Ga_2O_3 thin films, when synthesized under reducing conditions exhibit n-type semiconductor properties and due to β-Ga_2O_3's high melting point (1800°C) and high temperature stability, it has potential application in high temperature gas sensors [51]. Below 700°C, Ga_2O_3 exhibits sensitivity to reducing gases such as CO, H_2 and CH_x [52-54]. Above 900°C, Ga_2O_3 thin films are effective O_2 sensors due to the presence of oxygen vacancies in the material [55-56]. Recently, Matsuzaki *et al.* has successfully fabricated top gate field effect transistors (FET) structures using tin-doped Ga_2O_3 epitaxial films as n-channel layers which may find potential applications as active layers of optoelectronic devices in the deep UV regime in biotechnology and nanotechnology [57].

1.2.2 Gallium oxide Nanomaterials

Nanomaterials possess unique and interesting physical properties that have great potential for application in nanodevices. Hence, tremendous efforts and interest have been focused on the growth and characterization of Ga_2O_3 nanomaterials including nanorings [58], nanobelts [59], nanowires [60], nanocolumns [61], and nanosheets [62]. A large variety of synthesis techniques have been employed for the one-dimensional (1-D) growth of Ga_2O_3 nanomaterials (e.g. nanorods, nanobelts, nanowires) such as microwave plasma chemical vapor deposition [59], thermal evaporation [63], chemical vapor deposition (CVD) [64], metal organic chemical vapor deposition (MOCVD) [65], DC arc plasma [66] hydrothermal process [67] and laser ablation [68]. Most of the 1-D growth of Ga_2O_3 nanomaterials proceed either via vapor-solid (VS) or vapor-liquid-solid (VLS) mechanism. The detailed mechanism of VLS growth will be discussed in section 1.5.1. Catalysts such as Au [69], Sn [70], Pt [71] and Ir [72] have been successfully utilized to initiate the growth of single

crystalline 1-D Ga_2O_3 nanomaterials via the VLS mechanism. In order to establish a better understanding of the VLS growth of nanowires, new catalysts (Ag and Pd) were selected for the first time to investigate and study the catalyst-assisted growth of Ga_2O_3 nanowires. Furthermore, a comparison of the optical quality of the Au-, Ag- and Pd-catalyzed Ga_2O_3 nanowires was performed.

It is also of interest to study Ga_2O_3 nanoparticles and nanoclusters due to their high surface-to-volume ratio, which is useful for sensing applications. To date, Ga_2O_3 nanoparticles had been synthesized from mechanically ground GaN powders by thermal annealing in oxygen [73]. Here, a study of the room-temperature growth of Ga_2O_3 nanoparticles and nanoclusters using the PLA technique in N_2 and O_2 ambients was performed. The effect of growth parameters such laser fluence, deposition pressure, deposition gas and UV laser annealing on the size, crystallinity and optical properties of the Ga_2O_3 nanomaterials were investigated and analyzed.

1.3 Nanostructures and Quantum Mechanics in Reduced Dimensionality

In bulk semiconductor material, the charge carriers are free to move in a three directions. Carrier confinement in one dimension produces quantum wells. Confinement in two dimensions produces quantum wires or nanowires whereas confinement in three dimensions produces quantum dots or nanoparticles. Figure 1-2 illustrates the three regimes of quantization with the corresponding density of states.

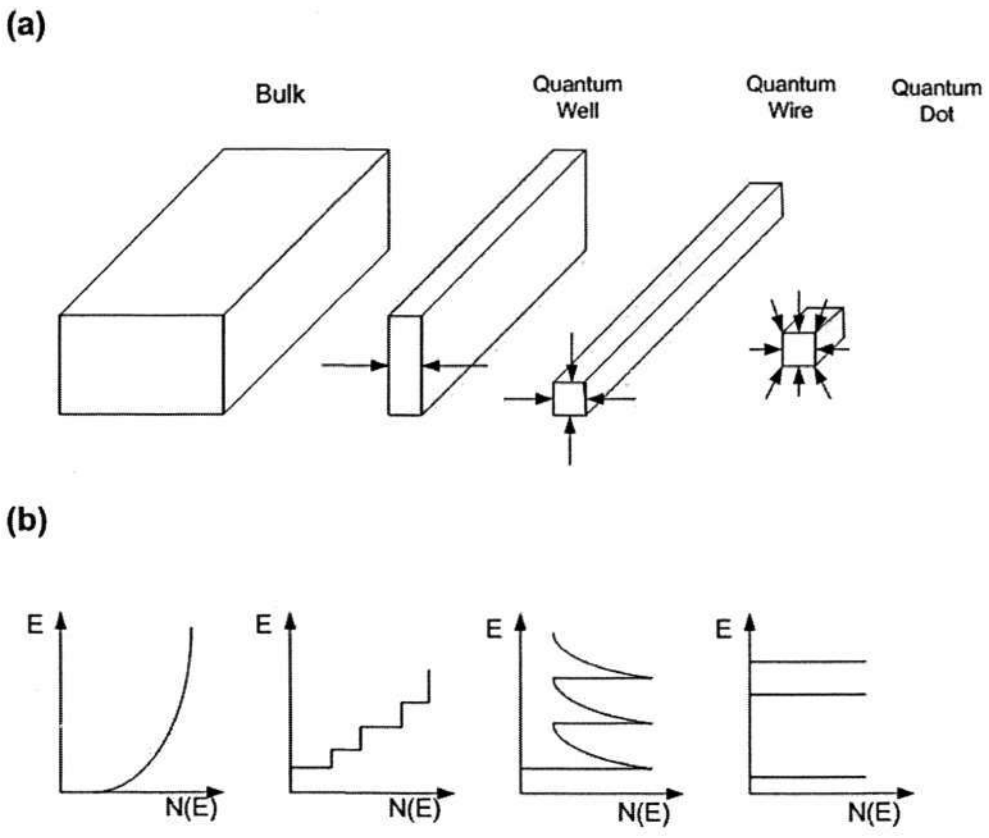

Figure 1-2 (a) 3 regimes of quantization with (b) corresponding density of states.

In bulk crystalline solids, the stationary Schrödinger equation for a particle of mass, m confined in an infinite potential well of width W in one dimension is expressed as

$$\left[-\frac{\hbar^2}{2m}\delta_x^2 + U(x)\right]\psi(x) = E\psi(x), \tag{1.1}$$

where ψ(x) is the wave function that gives the probability of finding a particle at the position x, and

$$U(\mathrm{x}) \begin{cases} 0 & \text{if } |\mathrm{x}| \le \mathrm{W}/2 \\ \infty & \text{if } |\mathrm{x}| > \mathrm{W}/2\,. \end{cases} \tag{1.2}$$

The wave function ψ(x) and energies E_n can be calculated analytically when the above potential is inserted into equation (1.1). The size dependence is now seen from the allowed energy levels of the particle in the potential well,

$$E_n = \frac{\hbar^2\pi^2 n^2}{2mW^2} = \frac{h^2 n^2}{8mW^2} \tag{1.3}$$

where n = 1, 2, 3,.. and the energy of these levels is inversely proportional to the square of the potential well size, W.

When a semiconductor crystal is illuminated with photons of sufficiently high energy, light can be absorbed by the material. The absorption of light by the semiconductor material promotes an electron from the valence band to the conduction band and results in the creation of an electron-hole pair. Such an electron-hole pair is defined as 'Mott-Wannier' exciton or simply 'exciton'. With reference to the solutions of equation (1.1), it is understood that the electron and hole, as well as bound state of the electron and hole, will have spatial extension. To put it simply, one can treat the exciton as a single particle with a center mass of motion and ignore the fact that an exciton is actually a composite particle. Due to center of mass motion, the reduced mass of an exciton is expressed as

$$\mu \equiv \left[\frac{1}{1/m_e^* + 1/m_h^*} \right] \tag{1.4}$$

where m_e^* and m_h^* are the effective masses of the electron and hole respectively. This is also known as the effective mass approximation, whereby one assumes that the electron with mass m_e is free but the effective mass m_e^* accounts for the interaction with the periodic potential. Since the exciton behaves as a single particle, the exciton Bohr radius can be written as [74]:

$$a_b = \varepsilon_r m_0 \mu^{-1} a_0 = \frac{4\pi\varepsilon_0 \varepsilon_r \hbar^2}{m_0 e^2} \left(\frac{m_e^* + m_h^*}{m_e^* m_h^*} \right), \tag{1.5}$$

where m_0 is the free electron mass, a_0 is the Bohr radius of hydrogen and ε_r is the dielectric constant of the semiconductor.

When a semiconductor becomes sufficiently small, the exciton Bohr radius becomes comparable to or larger than the crystal dimensions. Due to the potential step present at the surface of the crystal, the exciton wave function cannot extend fully beyond the edge of the crystal. As a result, the total exciton wave function has to be squeezed to fit into the crystal. This results in an increase in the kinetic energy of the exciton which is also known as the confinement energy. When this occurs, there will be a change in the band structure of the semiconductor (see Fig. 1-3a). These effects are often referred to quantum confinement effects. As the confinement energy increases with decreasing crystal size, the valence band will move downward and the conduction band will move upward. Hence the overall net effect is an increase in the bandgap of the semiconductor. This will result in a blue-shift of the band-to-band excitation energy of the semiconductor (see Fig. 1.3b). The effect of crystal size on the bandgap energy is given by the Brus equation [75],

$$E_g(r) = E_{g,bulk} + \frac{\hbar^2\pi^2}{2r^2}\left(\frac{1}{m_e^*} + \frac{1}{m_h^*}\right) - \frac{1.786e^2}{4\pi\varepsilon_0\varepsilon_r r} + 0.284E_R \,, \qquad (1.6)$$

where E_R is the Rydberg energy for the bulk semiconductor:

$$E_R = \left(\frac{13.606m_0}{\varepsilon_r^2\left(1/m_e^* + 1/m_h^*\right)}\right) \text{eV}, \qquad (1.7)$$

and $1.786e^2/\varepsilon_r r$ is the Coulomb term and $0.284E_R$ gives the spatial correlation energy and is a minor correction.

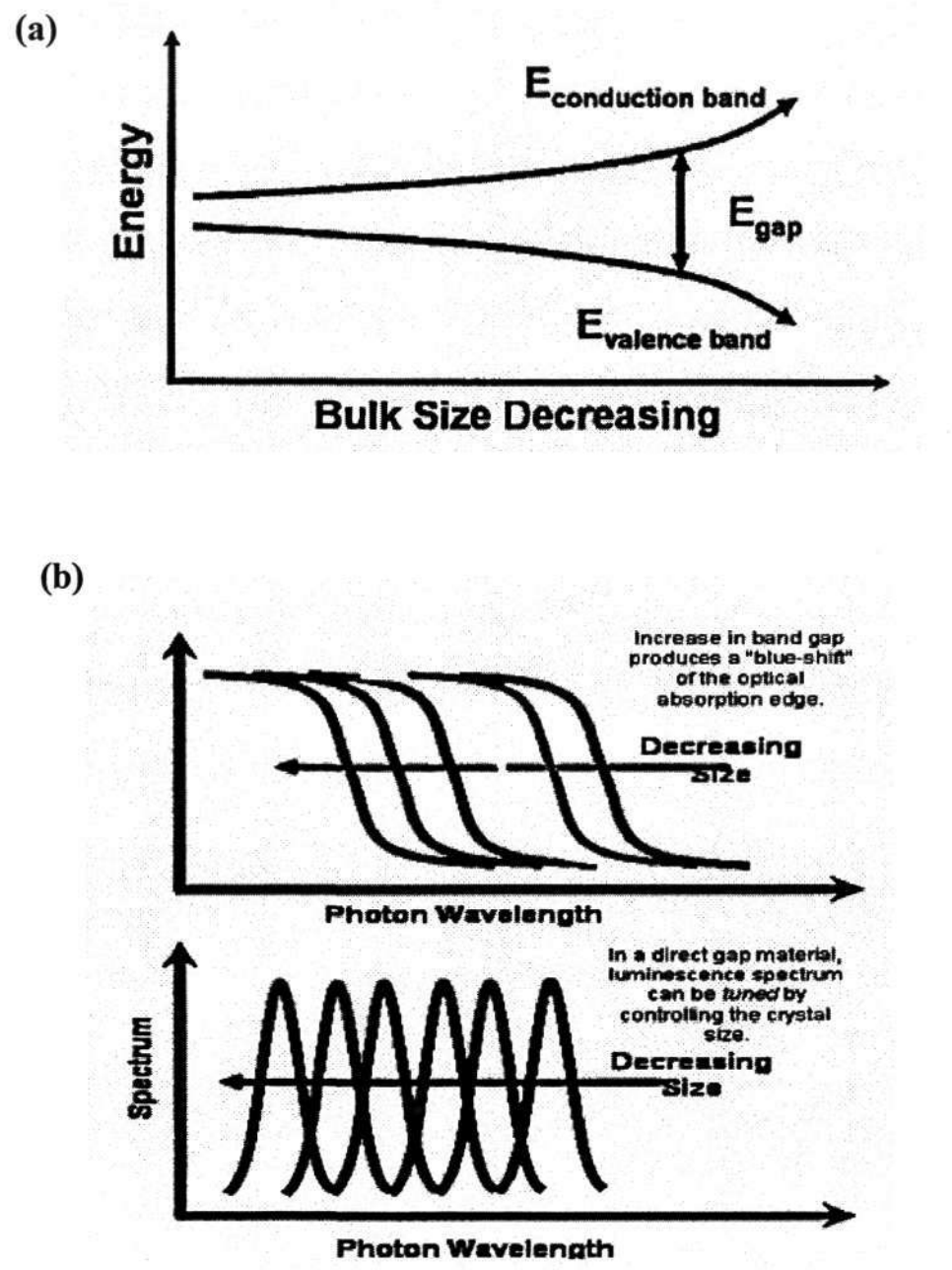

Figure 1-3 (a) Dependence of bandgap on size of semiconductor crystal and (b) Optical absorption and emission as a function of physical size [76].

As the physical dimensions diminish, the bandgap enlarges, resulting in a higher excitation energy required to promote an electron from the valence band to the conduction band and a larger energy released upon recombination of the electron-hole pair. This is depicted by the "blue shift" of the optical absorption edge and the photoluminescence spectrum as the physical size of the structure decreases as shown in Fig. 1-3. As the physical size of the nanostructures decrease, the probability of luminescence from recombination of the electron-hole pairs also increases due to the confinement effects.

1.4 Nanoparticle Synthesis

The importance of small particles in the nanometer regime was not recognized until the early 1980s when Ekimov-Efros *et al.* [77-78], Brus and coworkers [79] independently studied the size-dependent properties of semiconductor nanoparticles, and attributed it to quantum confinement effects. These effects were easily observed spectroscopically for semiconductor nanometer-scale particles. Since then, there has been intense interest in the study of nanoparticles.

The novel physical and chemical properties of nanoparticles are a consequence of their size-dependent surface area to volume ratio. In any material, the surface atoms make a distinct contribution to the free energy [80]. In a nanoparticle, the ratio of the number of surface atoms to the total number of atoms increases rapidly as the particle size decreases below 10 nm [81]. This was demonstrated by the liquid drop model adopted by Jortner *et al.* [82]. If R_c is the nanoparticle's radius and R_0 is the effective atomic radius, then the number of constituents is $n = (R_c/R_0)^3$, because the nanoparticle volume is $V = 4\pi R_c^3/3 = 4\pi R_0^3 n/3$. The surface area is $S = 4\pi R_c^2 =$

$4\pi R_0^2 n^{2/3}$ and the number of particles on the surface is $n_s = S/\pi R_0^2 = 4n^{2/3}$. Thus the fraction of surface atoms $F = n_s/n$ is

$$F = 4/n^{1/3} = 4R_0/R_c \tag{1.8}$$

One consequence of the large surface/volume ratio is quantum confinement. The charge carriers generated by light absorption are confined inside the particles in potential wells of lateral dimensions. The small particle size compared to the de Broglie wavelength of a charge carrier in the particle causes the electronic energy levels in the nanoparticles to become discrete and shifted in energy [83].

Spherical nanoparticles are "zero" dimensional nanostructure materials. They may also be referred as ultrafine particles for their small size, nanocrystals for their crystal characteristics and quantum dots for their quantum electronic energy. Nanoparticles have size-dependent electronic [84], optical [85, 86], photochemical [87], catalytic [88] and mechanical [89] properties. For example, in CdS nanoparticles, the bandgap can be tuned between 2.5 and 4 eV, according to the size of the nanoparticles [90]. Due to their unique size-dependent properties, nanoparticles are considered to be new types of materials with highly promising applications such as light emitting quantum dots [91] and gas sensing devices [92].

In general, there are two ways to synthesize nanoparticles from the "bottom up". One way is via chemical methods, whereby the nanoparticles are grown by arrested precipitation either at high temperature in hosts such as silicate glasses [11] or at room temperature in solution [9, 10]. Another class of methods is physical methods, in which the nanoparticles are synthesized via the condensation of the atomic and molecular vapor into the solid phase [8]. Both chemical and physical methods involve

processes of nucleation and growth in supersaturated solutions or vapors and result in the formation of clusters and nanoparticles. The concept of classic nucleation theory can be applied to describe the synthesis of nanoparticles in liquids and gas phases [82]. According to classical homogenous nucleation theory [93, 94], the critical radius r^* of condensation nucleus formed from the vapor phase is strongly dependent on the supersaturation, S, where

$$r^* = 2\sigma v/k_B T(\ln S), \qquad (1.9)$$

and where σ is the surface tension, v is the volume per molecule in the bulk liquid, k_B is the Boltzmann constant and T is the temperature. This equation reveals the very important rule that the larger the supersaturation S, the smaller the critical size of the condensation nucleus.

It is preferred to synthesize nanoparticles from atomic or molecular precursors, in order to gain control of the particles' size distribution. From classical nucleation theory, smaller nuclei will form at larger supersaturations. However the particles will also grow relatively fast.

1.5 Nanowires Synthesis

Ever since the discovery of carbon nanotubes by Iijima [95], there has been great interest in the synthesis and characterization of various one-dimensional (1-D) nanostructures. Nanowires, nanorods and nanobelts constitute an important class of 1-D nanostructures, which provide models to study the relationship between electrical transport, optical and other properties with dimensionality and size confinement.

Nanowires can also act as active components in devices as revealed through recent investigations [96, 97]. In the last 3-4 years, a variety of nanowires has been synthesized and characterized. One of the crucial factors in the synthesis of nanowires is the control of composition, size and crystallinity. Several synthesis strategies have been developed for the growth of 1-D nanowires and nanobelts with different levels of control over the growth parameters. The widely-employed synthesis techniques are thermal evaporation [63], chemical vapor deposition [64] and laser ablation [68]. Most of these include the use of a catalyst and appear to follow the vapor-solid-liquid growth mechanism first proposed by Wagner and Ellis in 1964 [98].

1.5.1 The Vapor-Liquid-Solid (VLS) Growth of Nanowires

The VLS growth mechanism was proposed for nanowires grown by catalyst-assisted methods. Wagner and Ellis provided a clear demonstration of large single-crystalline whisker growth (Au particle on {111} Si) due to the size confinement of the catalytic cluster solvent medium. The core of the VLS growth mechanism is the introduction of a liquid-solid interface in the vapor-phase based growth, which breaks the symmetry of the isotropic crystal, making it grow in a 1-D manner. Figure 1-4 illustrates the VLS growth process that can be divided into 4 distinct stages. Consider a eutectic reaction between a catalyst and a material B supplied in the vapor phase. In the first step, a few to tens of monolayers of the catalyst (usually a transition metal) is introduced into the growth process. The metal catalyst can be deposited onto the substrate by a number of *ex-situ* deposition techniques (e.g. e-beam evaporation, sputtering or molecular beam epitaxy). Material B is then introduced on the metal catalyst surface in vapor phase.

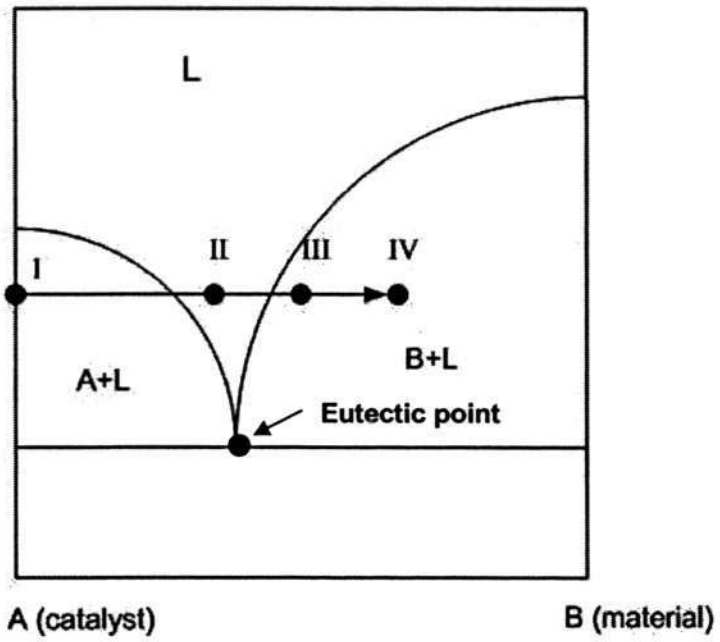

(a)

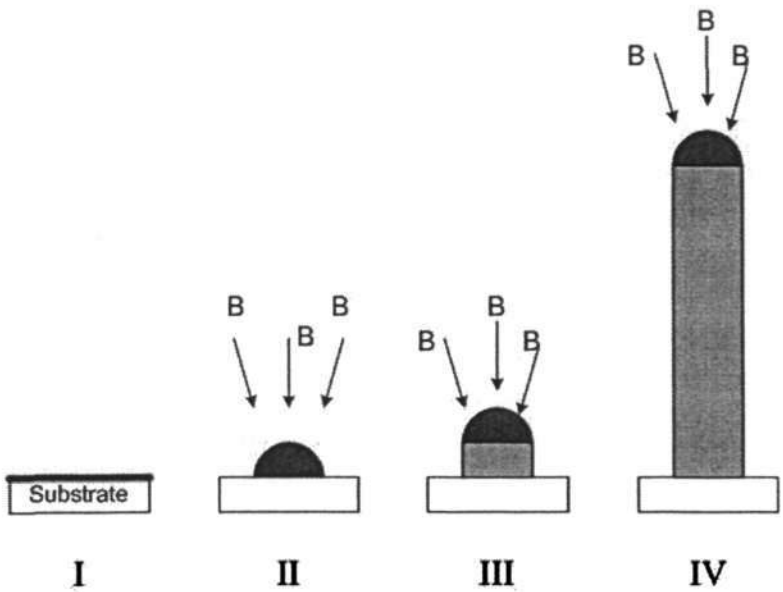

(b)

Figure 1-4 Schematic diagram of (a) catalyst-material eutectic phase diagram, and (b) a vapor-liquid-solid model.

The major requirement on the metal catalyst is that it must form a liquid solution with growth material B at the growth temperature and be able to create a supersaturation acting as a driving force for crystallization of the nanowires. When the growth temperature is above the eutectic point, material B dissolves into the metal catalyst to form a liquid alloy at point II in Fig. 1.4. The nanowires (B) starts to nucleate and grow at the liquid-solid interface after the liquid alloy becomes supersaturated with material B at point III and point IV. Extended formation of the nanowires can be maintained as long as a sufficient quantity of reactant is present and the growth temperature is kept above the eutectic temperature. In the VLS mechanism, it is found that the catalyst dictates the formation of the nanowires. If the material in the vapor source does not dissolve in the liquid catalyst, then the formation of the nanowires is prohibited.

Wu *et al.* [99] have confirmed this mechanism by *in-situ* observation of the growth of Ge nanorods in the chamber with the aid of a transmission electron microscope (TEM), equipped with a temperature-controlled stage. Ge nanorods were grown with GeI_2 as the vapor source and Au as the catalyst. Based on this mechanism, it is found that the diameter of the nanowires can be controlled by the size of the liquid particle and remains essentially unchanged during the entire growth process. In other words, smaller catalysts will result in thinner nanowires. However, the major drawback of the VLS method is the presence of the catalyst nanoparticles at the ends of the nanowires which may contaminate the semiconductor nanowires and thus altering their properties.

Nevertheless, since the diameter of the nanowires is determined by the diameter of the catalyst particles, this method provides an efficient means to obtain uniform-sized nanowires. Also, with knowledge of the phase diagrams of the metals and the material

of the desired nanowire, appropriate catalyst and growth temperature between the eutectic and the melting point of the material can be determined for successful deposition. Synthesis techniques such as laser ablation, thermal evaporation and chemical vapor deposition can be utilized to generate the reactant species in vapor form as required for nanowire growth. As mentioned earlier, metal catalysts can be sputtered or evaporated onto the substrates. An advantage of this route is that patterned deposition of catalyst particles yields patterned nanowires. Using this growth mechanism, nanowires of materials including Ge [99], ZnO [100] and GaN [6] have been successfully obtained.

1.6 Research Motivation

The investigation of nanostructured low-dimensional semiconductor oxides has been of great interest in the recent years due to their potential applications in optoelectronic and gas sensing nanodevices. In particular, monoclinic gallium oxide (β-Ga_2O_3) is a very good candidate for these purposes because of its wide bandgap of 4.8 eV that provides the possibility of light emission in the infrared, visible, and ultraviolet regions of the spectrum. Furthermore, the extremely small physical dimensions of nanostructures imply high surface to volume ratios, which are necessary for good sensing applications. In addition, Ga_2O_3 also exhibits good conduction properties related to oxygen vacancies. Synthesis processes have been employed to obtain Ga_2O_3 nanomaterials using metallic Ga, GaN, GaAs or Ga_2O_3 as starting materials. Unfortunately, most of these techniques have severe drawbacks such as contamination from the liquid, crucible and/or reactants, long processing time (2-15 hrs) and high annealing temperatures (800 to 1200°C) that lead to high thermal budgets and very broad size distributions for the Ga_2O_3 nanomaterials. It is also

difficult to synthesize metal oxide nanowires by simply evaporating Ga_2O_3 powders because of their high melting point. Ga_2O_3 bulk powders require a high processing temperature to dissociate into Ga and O species to form nanomaterials. Therefore, there is an incentive to find new methods of synthesis as well as to overcome some limitations in the current synthesis methods, so that high quality growth of Ga_2O_3 nanoparticles and nanowires can be attained with excellent control of their dimension, size, morphology, composition, crystallinity and optical properties.

1.7 Research Objectives

To overcome the limitations and challenges in the current synthesis methods, a novel growth technique has been developed to synthesize Ga_2O_3 nanomaterials via pulsed laser ablation of GaN in N_2 and O_2 ambient. From the literature, Ga_2O_3 nanowires have been synthesized by thermal annealing of milled GaN [63] and arc-discharge of GaN [101]. However these techniques suffer from several drawbacks that were discussed earlier. On the contrary, the pulsed laser ablation technique provides a very promising approach for fast and contamination-free deposition of nanomaterials of various materials under a very wide range of growth conditions. Therefore the main objectives of this work are:-

- To design and develop a novel, efficient and low-temperature growth method for Ga_2O_3 nanoparticles, nanoclusters and nanowires via photo-dissociation of GaN by pulsed laser ablation.

- To study and understand the growth mechanisms and quantum confinement effects in Ga_2O_3 nanoparticles, nanoclusters and nanowires.

- To investigate and analyze the effect of growth conditions such as deposition pressure, deposition ambient, growth temperature, laser fluence and catalyst effect on the size, dimensions, crystallinity, structural and optical properties of Ga_2O_3 nanomaterials.
- To improve the crystallinity and photoluminescence of amorphous Ga_2O_3 nanoparticles and nanoclusters via pulsed KrF excimer laser annealing.

1.8 Thesis Outline

The background, motivation and objectives of this project are presented in Chapter 1. Chapter 2 elucidates the necessary theoretical background and literature required for this work whereas Chapter 3 provides the project methodology, experimental procedures and characterization techniques employed during the course of this project. Room-temperature synthesis of Ga_2O_3 nanoparticles and nanoclusters by pulsed laser ablation of GaN is presented in Chapter 4. The optical properties of Ga_2O_3 nanoparticles and nanoclusters are studied in great detail in Chapter 5. Chapter 6 presents the effect of pulsed KrF excimer laser annealing on the crystallinity and photoluminescence of amorphous Ga_2O_3 nanoparticles and nanowires, while a detailed study on the synthesis of Ga_2O_3 nanowires with Au, Ag and Pd catalysts is found in Chapter 7. Lastly, Chapter 8 summarizes the essential points deduced from the analysis of the results. Recommendations for future work are also presented in Chapter 8.

CHAPTER 2

BACKGROUND AND LITERATURE REVIEW

2.1 Pulsed Laser Ablation (PLA)

The study of the interaction of high power lasers with solids began with the advent of the first ruby laser in 1960. Since then, the laser-material interactions have provided information that has contributed significantly to the fields of physics and chemistry. Smith and Turner first demonstrated the use of laser ablation in 1965 when they succeeded in the laser deposition of thin films. Due to the poor qualities of these films, the laser ablation technique for thin film growth did not get adequate recognition amongst researchers and scientists and was unable to compete with other established thin-film techniques. However, with the advent of nanosecond lasers in 1970 and their success in the growth of commercial high-temperature superconductor thin film devices in the late 1980s; laser ablation studies have started to gain increased importance in industry.

Laser ablation is generally used to describe explosive laser-material interaction. When a short-pulsed laser beam is focused onto a solid target, a portion of the material instantaneously explodes into vapor. Laser-material interactions involve coupling of optical energy into a solid, resulting in vaporization, ejection of atoms, ions, molecular species and fragments. The laser ablation technique offers several advantages including stoichiometric transfer of a complex, multi-element material to the substrate, reactive deposition in low-pressure ambient gas and the possibility of synthesizing materials from a small target, especially if the material is extremely expensive or isotopically pure. Today, the laser ablation technique is widely used in the areas of thin film technology [102-104], nanoparticles and nanowires growth [105,

106], surface cleaning [107], etching and patterning [108], sampling for chemical analysis and in areas of fundamental research such as surface-kinetic studies [109], and optical damage investigations [110].

2.1.1 Laser-Material Interaction

The first step towards an effective ablation is the absorption of a significant amount of laser light by the material (see Fig. 2-1). In materials such as metals, the band structure of the metals favors absorption of most low-to-moderate energy photons from the laser [111]. Once the photons are absorbed by the metal, the kinetic energy of the conduction electron increases dramatically, and the electrons are heated to high temperatures. The absorbed energy is subsequently transferred to the lattice by means of electron-phonon interactions. The time duration for this transfer is typically in the order of picoseconds [111]. The energy, transferred to the lattice in the form of heat, resulting in a heat affected zone (HAZ) also causes the material to vaporize locally, thereby generating a plasma of ions of the material being ablated away.

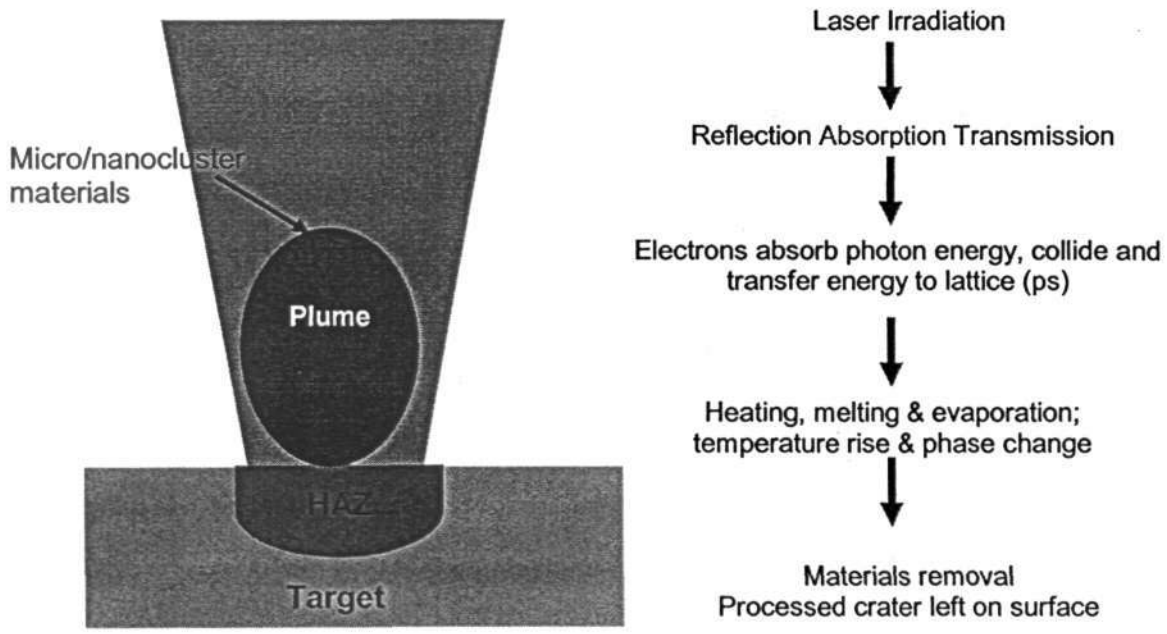

Figure 2-1 Schematic illustration of pulsed laser ablation process.

There are numerous factors that govern the effectiveness of the ablation process. The most important factor is the thermal conduction within the material. The key to effective ablation is to concentrate the energy absorbed from the laser over a small area. However, in highly conductive materials, like metals, the energy absorbed is dissipated over a large area by heat diffusion into the bulk material during the laser pulse, and the temperature does not increase high enough to vaporize the material. One way to circumvent this problem is to shorten the laser pulse duration. The thermal conduction within a material is directly related to the depth over which the absorbed energy can be transferred and is commonly referred to as the *thermal diffusion length*, which is given by the equation

$$L = \sqrt{D * t} \quad , \qquad (2.1)$$

where L is the diffusion length, D is the thermal diffusivity and t is the pulse width of the laser.

From the above equation, it can be seen that the smaller the pulse width of the laser, the smaller the thermal diffusion length in the material. This means that the absorbed energy is transferred over a small area. For short laser pulses (nanosecond to femtosecond region) the heat diffusion into the material is usually negligible. Consequently, the energy accumulates rapidly within the optical absorption volume, resulting in an effective ablation process as soon as the accumulated energy reaches a critical value of the order of the enthalpy of evaporation [112].

2.1.2 Characteristics of the Plume

A plume is basically a plasma of activated species formed from the thermal emission of the atoms, ions, and electrons from the target surface. During the duration of the pulse, the plasma of the charged species can absorb most of the laser energy by the inverse bremsstrahlung process and can screen the target from the remainder of the laser pulse, thereby making ablation very ineffective [113]. This can be avoided by working with ultrashort laser pulses so that the plasma formation does not occur during the duration of the pulse, but only after the pulse terminates. By using ultrashort laser pulses, the heat diffusion into the metal becomes insignificant during the pulses' time scale. This is because the electrons are not in thermal equilibrium with the laser pulse and do not lose energy to the lattice phonons, which causes the material to evaporate and gives rise to the formation of a plasma consisting of highly activated species. The plasma expands at very high velocities, typically at the rate of 10^6 cm/s in vacuum. This is due to large density gradients that are present at the outer edge of the plasma. The physics of plasma expansion and plasma dynamics becomes very complicated for ablation processes carried out in a background gas rather than in vacuum.

2.1.3 Plume in a Background Gas

The primary reason for introducing a background gas is to promote gas-phase reactions between the target atoms and the background gas. In the current experiment, for example, Ga_2O_3 nanoparticles, nanoclusters and nanowires were synthesized from the gas-phase reaction between highly activated Ga and GaN species in the plasma and the O_2 or N_2 molecules, which was introduced into the chamber as the background gas. In the presence of an atmosphere, the ablated species produce a

shock wave, which is formed by the piston-like action of the fast expanding ablated species pushing forward on the backing gas [114]. This type of shock wave is typically referred to as a blast wave and is produced when a large amount of energy is deposited in a small volume and when there is a backing gas present to support the wave. The blast waves move forward at extremely high velocities and decelerates rapidly to the speed of sound in the medium (Mach 1) with increasing distance from the target. Blast wave velocities as high as Mach-27 have been previously observed using shadowgraphy techniques [115]. As a result of this dramatic deceleration, a high density of the target species is maintained for long periods of time.

Due to the long residence time of the target species, a gas-phase reaction between the target atoms and the background gas is promoted. In addition to promoting the gas-phase reaction, the presence of the background gas helps in significantly cooling the clusters of the product, thereby controlling the final size of the particles. By cooling the particles, there is insufficient energy for the particles to grow. In the absence of sufficient cooling, however, the clusters of the reaction products will keep growing in size by means of Ostwald ripening. Eventually, the clusters will form particulates that are much larger than what is expected. The final size of the particles largely depends on the pressure of the background gas. If the pressure is too low, the particle size will be large due to insufficient cooling, and there is also a possibility of the reaction being incomplete. On the other hand, if the pressure is too high, the particles get cooled too fast and the crystallinity of the end product is lost. High pressure also promotes condensation of the target species before they can react with the background gas, subsequently making the reaction incomplete. Thus it is important to find an optimum pressure for the background gas which will produce high quality particles that are in the nanometer regime with desired characteristics.

2.2 Methods for the VLS Synthesis of Nanowires

In VLS synthesis, one of the major requirements is the presence of a metallic catalyst and nanowire material in the vapor phase. As such, various techniques such as laser ablation, chemical vapor deposition, physical vapor deposition, thermal evaporation, template-based synthesis, solution-based synthesis and etc. have been developed for the VLS synthesis of nanowires. In this section, only three primary techniques will be compared and discussed, namely laser ablation, chemical vapor deposition (CVD) and physical vapor deposition (PVD). Table 2-1 compares the general characteristics, advantages and disadvantages between laser ablation, chemical vapor deposition (CVD) and physical vapor deposition processes for the VLS synthesis of nanowires.

Table 2-1 Comparison of various nanowire synthesis methods.

Methods	**General Characteristics**	**Advantages**	**Disadvantages**
Laser Ablation	• Vapor source is generated by high power laser ablation. • Vapor is transported to a lower temperature zone where growth proceeds by VLS mechanism.	• High crystallinity • Good diameter control • Easy control of localization, size distribution and growth orientation. • In-*situ* doping is possible	• Complex tool requirement • Prohibitive cost of a high-power laser
Chemical Vapor Deposition (CVD)	• Vapor source is generated by evaporation or carbothermal reduction of liquid of solid source. • Vapor is transported to a catalyst-coated substrate and growth proceeds by VLS mechanism.	• High crystallinity • Good diameter control • Easy control of localization, size distribution and growth orientation. • Inexpensive toolsets	• Difficult to synthesize materials with low volatility • Simultaneous deposition of multiple materials may be difficult
Physical Vapor Deposition (PVD)	• Evaporation of source and condensation onto the substrate surface.	• Least complex toolset requirement	• Same disadvantages as CVD • Difficult to control diameter distribution.

2.3 Critical VLS Growth Parameters

In this section, a literature review on the critical process parameters which influences synthesis via VLS mechanism is presented. Based on the VLS model as discussed in Chapter 1, it is apparent that growth parameters such as type of catalyst, temperature, pressure, gas flow rate, size of catalyst particles, crystallographic orientation of the substrate surface and reaction time play critical roles in controlling the morphology of the as-grown nanowires. In general, these growth parameters are applicable and relevant to the abovementioned synthesis techniques and the effects of these parameters will be discussed in greater detail below.

2.3.1 Alloying and Solubility of Materials with Catalyst

It is important to choose an appropriate catalyst when synthesizing nanowires via the VLS mechanism. The elements needed for the growth of the nanowires must be soluble in the catalyst to form a liquid alloy. For single-element nanowires, such as Si and Ge, it is usually sufficient to identify metals that form a eutectic phase with the element. While in the case of compound materials, such as silicon carbide or Ga_2O_3, the choice of selecting a suitable catalyst is not so straightforward as two or more elements need to be simultaneously absorbed by the catalyst. Hence, when synthesizing a binary nanowire, the best approach is to identify the alloy of the metal (catalyst) and one of the elements of the nanowires with the lowest melting temperature. An equilibrium phase diagram provides invaluable information for this purpose [116]. For example, a composition containing 50 at. % of gallium is liquid at 461.3°C - the minimum temperature for growing Ga_2O_3 nanowires with Au catalyst (see Fig. 2-2). It has been demonstrated that the melting temperature of nanoparticles is lower than that of the bulk due to their large surface area to volume ratio [117-120].

As a result, the temperature of nanowire synthesis can be lowered relative to the bulk melting temperature of the alloy catalyst.

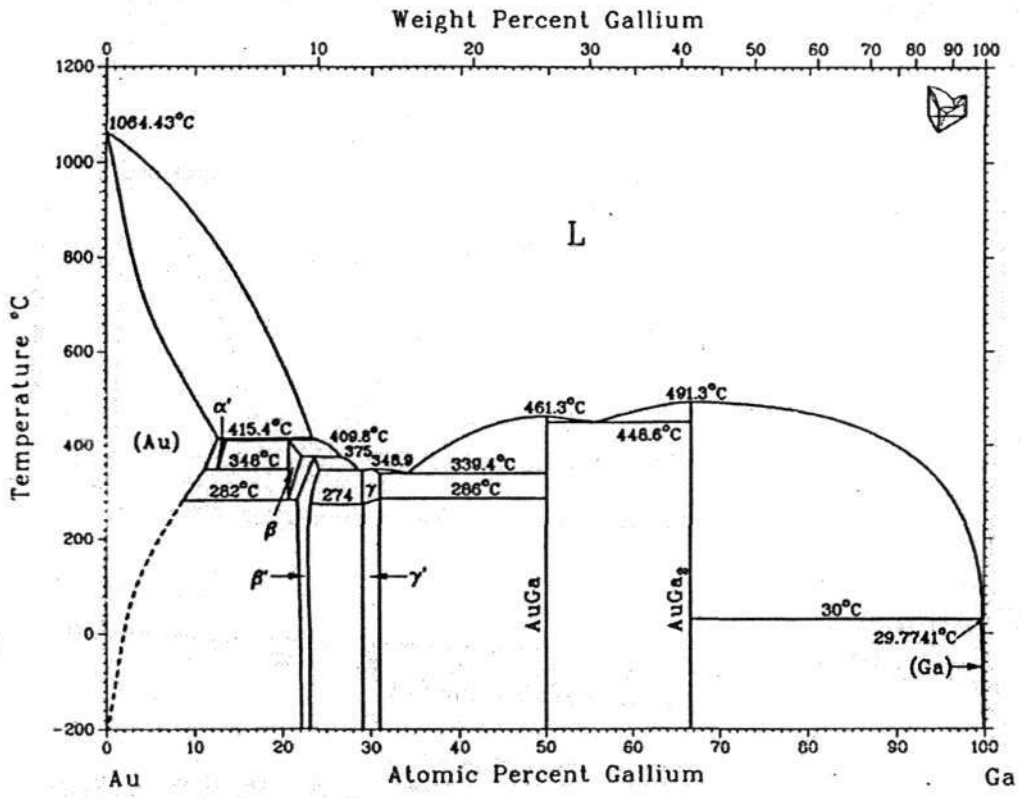

Figure 2-2 Au-Ga phase diagram [116].

Typically, pure elements have been used for initiating nanowires growth [121-123]. However, the use of eutectics as catalyst instead of pure elements is more advantageous [124, 125]. Eutectics are more oxidation resistant and due to their low melting temperatures, nanowire formation can be achieved at much lower temperatures. Eutectic catalysts have been successfully used to grow GaN [126], ZnO [127] and SiC [128] nanowires. It was also found that the choice of catalyst has significant effects on the morphology of the nanowires. Jackson and Wagner [129] found that the morphologies of the micron-sized whiskers were catalyst dependent.

Whiskers with hexagonal cross-section were obtained when a Au catalyst was used but when Ni was used, whiskers with both hexagonal and circular cross-sections were observed. The catalyst dependent cross-sections were explained in terms of minimization of the surface free energy of the whisker and the growth mechanism at the catalyst-whisker interface, e.g. growth rates.

2.3.2 Catalyst Thickness and Size of Monodispersed Nanoclusters

Many publications suggest that the diameter of a nanowire is controlled by the size of the alloy droplet, which is dictated by surface energetics and thermodynamics. Film thickness of the catalytic material directly correlates to the diameter of the liquid alloy droplets. As the temperature increases, the thin film of metal catalyst breaks apart to form nanoclusters on the surface of the substrate. The degree of the coalescence is a function of the film thickness, surface tension of the liquid metal catalyst, wetting properties, temperature, heating rate and the ambient conditions. For more rigid control, monodispersed metal nanoclusters are recommended since the average diameter of the nanoclusters is readily controlled and the diameter distribution is also, ideally, narrower. In a study performed by Gudiksen [130], indium phosphide nanowires were grown on silicon wafers with gold nanoclusters by laser ablation. The substrate was placed inside a quartz tube, downstream of a solid InP source. The furnace temperature was maintained at 650 – 700 °C, while the temperature of the substrate was kept at 500 – 600 °C.

2.3.3 Temperature

In principle, the synthesis of nanowires of complex compositions is feasible, if suitable catalyst and appropriate growth temperatures are determined. A good catalyst

material allows the formation of a liquid alloy with desirable material for nanowire growth at a reasonably practical temperature. The temperature is typically determined with a phase diagram of the catalyst and the nanowire material. A temperature range where the eutectic liquid-alloy formation, between the catalyst and the nanowire material, is located, is recommended. The growth temperature should be selected between the eutectic point and the melting point of the alloy. The effect of temperature on growth and morphology of nanowires has been reported in the literature. In a study performed by Chen *et al.* [131], GaN nanowires were grown using molten Ga at temperature of 800 – 1050 °C in an ammonia ambient at atmospheric pressure on Si (100) and quartz substrates, as depicted in Fig. 2-3. The authors observed larger diameters at faster heating rates (> 100 °C/min) and narrower diameter distribution at slower heating rates (25 °C/min). The optimum growth temperature was at 910 °C. Nanowires with poor crystallinity and amorphous solid were formed at temperatures below 850 °C. At temperature higher than 1050 °C, nanowire growth was minimal.

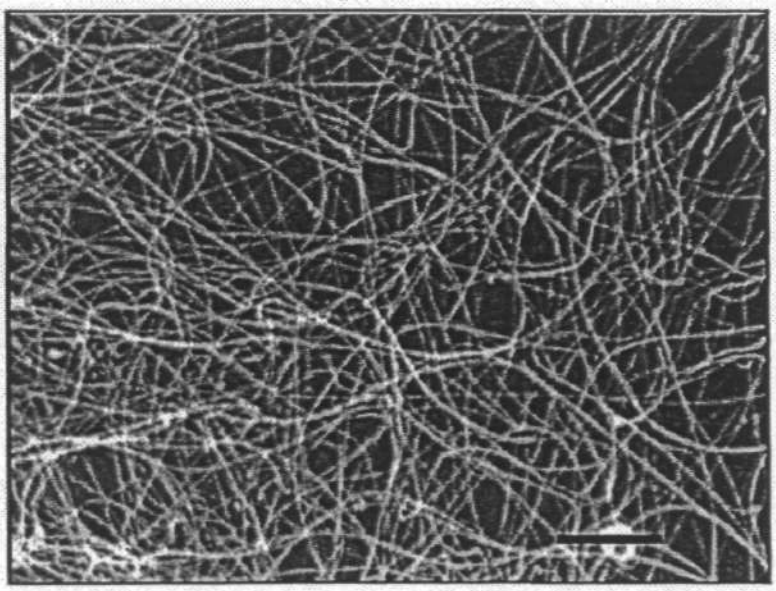

Figure 2-3 SEM image of GaN nanowires on a substrate [131].

Evidently, both growth temperature and heating rate significantly affect the growth of nanowires. The VLS model indicates existence of a process temperature window for the formation of nanowires. At temperatures below the eutectic temperature between the nanowire material and catalyst, generation of the source material or alloy formation may be prohibited. On the other hand, if the temperature of synthesis is too high, excessive supply of thermal energy increases the kinetic energy of the vapor-phase and liquid-phase source material. Excessive thermal energy may result in reversible nucleate formation and evaporation of the source molecules from liquid alloy droplet, hence prohibiting the growth of nanowires. Furthermore, "premature nucleation" and amorphous film growth may result if the nucleation stage occurs before the coalescence of the gold film to form gold nanoclusters completes, which usually occurs at lower temperature and faster heating rates.

2.3.4 Source-to Substrate Separation

In most cases, the vapor phase species will be transported to the substrate by the carrier gas to form nanowires. However, due to the loss of reactant materials via deposition on the wall of the reactor, mass transport limitation prevents most of the vapor reactants from reaching the substrate, resulting in low growth efficiency. As a consequence, many researchers have performed studies on the effect of the separation between the source and substrate in a tube reaction chamber. Chen *et al.* [132] reported that the diameter distribution of nanowires has a strong dependence on the separation distance between the source and the substrate. For the separation distance of 1 cm, diameters of nanowires are in the range of 50-150 nm. When the separation distance is increased to 10 cm, the diameter distribution is reduced to 20-50 nm. This

observation may be explained by the mass-transport phenomena whereby at longer separation distance, lesser amount of vapor phase species can reach the substrate.

2.3.5 Substrate Orientation

In general, nanowires have preferred growth directions. For the growth of ZnO nanowires on Si (111) substrates, Huang *et al.* [133] reported the preferred growth direction of ZnO nanowires is along the [001] direction, with lattice spacing of 2.56 ± 0.05 Å between the (002) crystal planes and the ZnO nanowires do not grow perpendicularly to the surface of the substrates (Fig. 2-4). Wu *et al.* [134] propose a method to grow vertically aligned nanowires by catalyst-free pulsed laser deposition methods. According to them, to grow vertically aligned nanowires, the substrate should have the surface plane orientation perpendicular to the preferred growth direction of the desired nanowires i.e. Si (111) substrate for Si nanowires and sapphire (110) substrate or Si (100) for ZnO nanowires. In the case of ZnO, the lattice mismatch between the ZnO a axis and the sapphire c axis is less than 0.08 % at room temperature. Figure 2-5 shows the vertical growth of ZnO nanowires on the Si (100) substrate.

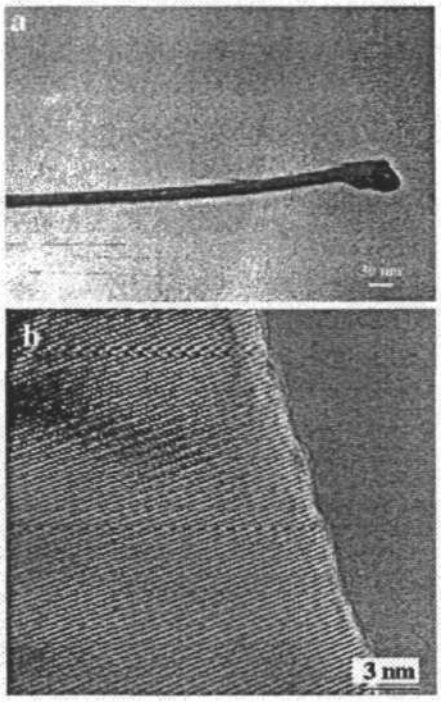

Figure 2-4(a) TEM image of a thin ZnO nanowire with a Zn/Au alloy tip and (b) High resolution TEM image of a single-crystalline ZnO nanowire showing the lattice fringes [133].

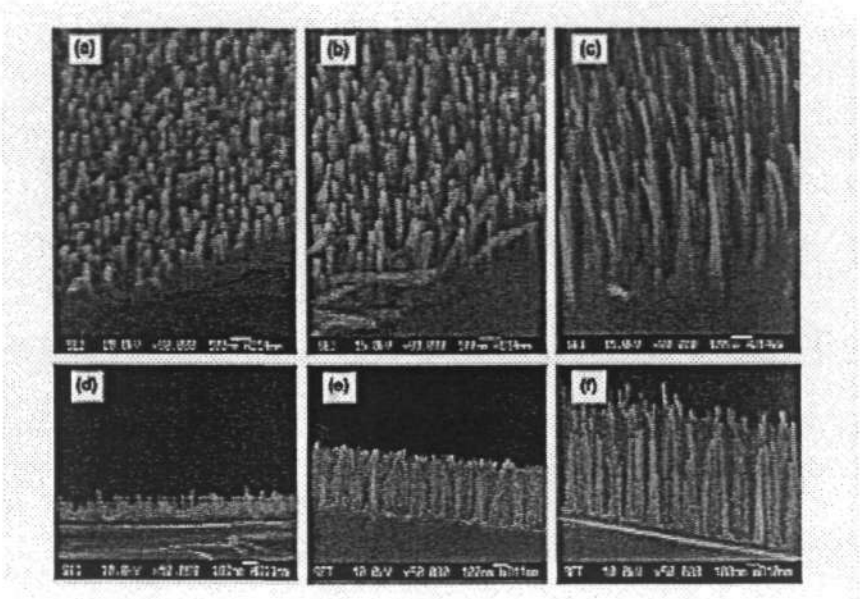

Figure 2-5 SEM images of ZnO films grown on Si(1 0 0) at T_{sub} = 600 °C and $p(O_2)$ ~10 mTorr for t = 15, 30 and 45 min, respectively, each viewed at a tilt angle of ~40° to the horizontal (a–c) and in cross-section (d–f) [134].

2.3.6 Deposition time

According to the VLS model, a longer reaction time will result in longer wires. Gudiksen [32] also studied the effect of growth time on length of InP nanowires. In his study, the vapor source was generated by laser ablation of the solid InP source. InP nanowires were synthesized at various growth times using gold nanoclusters of 20 nm average diameter. Figure 2-6 shows SEM images of the nanowires grown for different durations and Fig. 2-6(d) shows the relationship between the nanowires length versus the laser ablation (growth) time. As growth time increases, the length and the number of nanowires increase. The authors also observed that the aerial distribution of the nanowires is denser at longer growth times. Therefore with PLA methods, one can simply control the length of the nanowires by controlling the length of the deposition time.

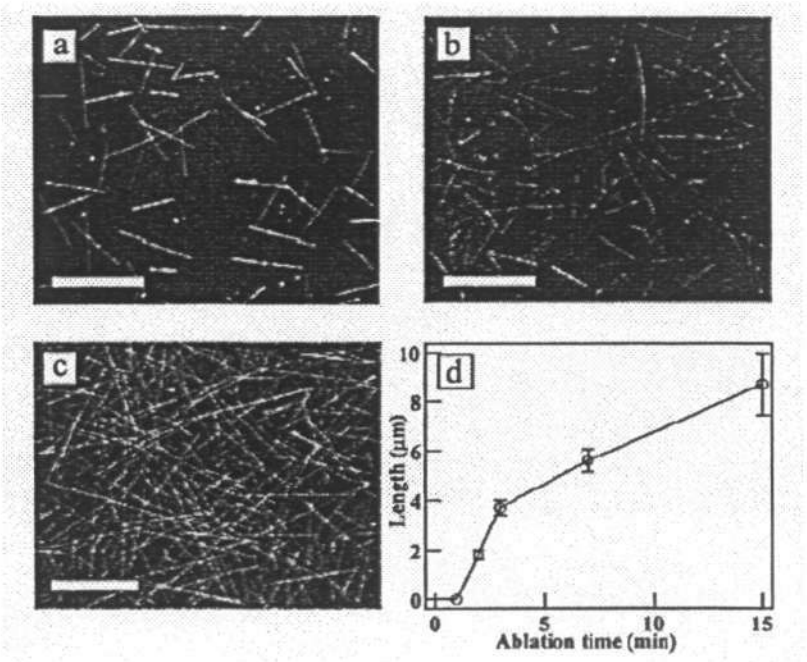

Figure 2-6 FE-SEM images of nanowires produced after growth times of (a) 3 min, (b) 7 min, and (c) 15 min. All scale bars correspond to 5 μm. (d) Plot showing the relation between growth time and nanowires length [130].

CHAPTER 3

Ga_2O_3 Nanoparticles, Nanoclusters and Nanowires: Synthesis and Characterization

This chapter presents an overview of the synthesis procedures for the growth of Ga_2O_3 nanoparticles, nanoclusters and nanowires by pulsed laser ablation (PLA), laser annealing of Ga_2O_3 nanoparticles and nanoclusters as well as the characterization techniques employed in this research.

3.1 Synthesis of Ga_2O_3 Nanoparticles, Nanoclusters and Nanowires

3.1.1 Deposition Chamber

Ga_2O_3 nanoparticles and nanowires were synthesized in a high vacuum stainless steel deposition chamber. The deposition chamber was first pumped with a turbomolecular pump to achieve a base pressure of 3×10^{-5} Torr. Pure N_2 (99.9995%) or O_2 (99.99%), depending on whether it was for inert or reactive deposition, was then introduced slowly into the deposition chamber. The desired deposition pressure was achieved by controlling the flow rate of the gas that was introduced into the chamber. Typically, the chamber pressure was maintained between 1 to 100 Torr during the growth of the nanoparticles, nanoclusters and nanowires. The chamber has a quartz window through which the laser beam was able to pass and be incident on a rotating target with a loss of less than 20%. The angle between the incident laser beam and normal to the target surface was 45°. The deposition time ranged from 5 to 20 mins. A schematic and photograph of the deposition chamber is shown in Fig. 3-1 and Fig. 3-2 respectively.

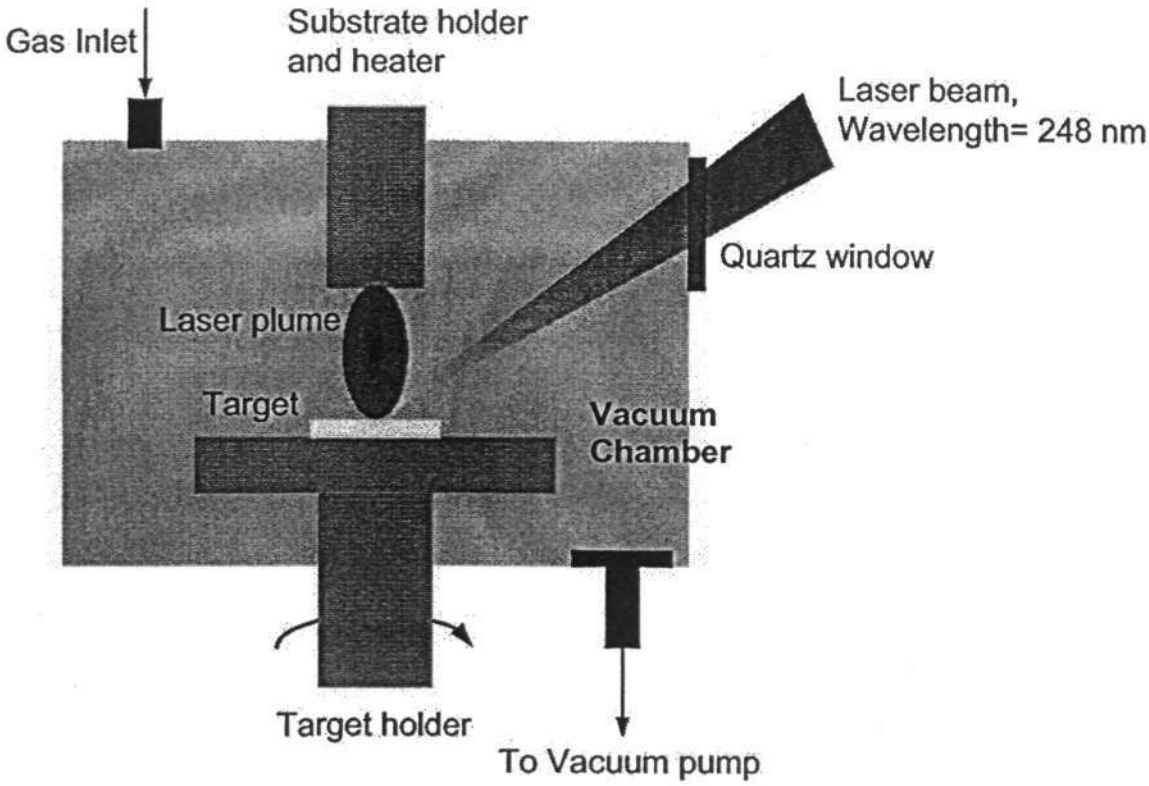

Figure 3-1 Schematic of pulsed laser ablation system.

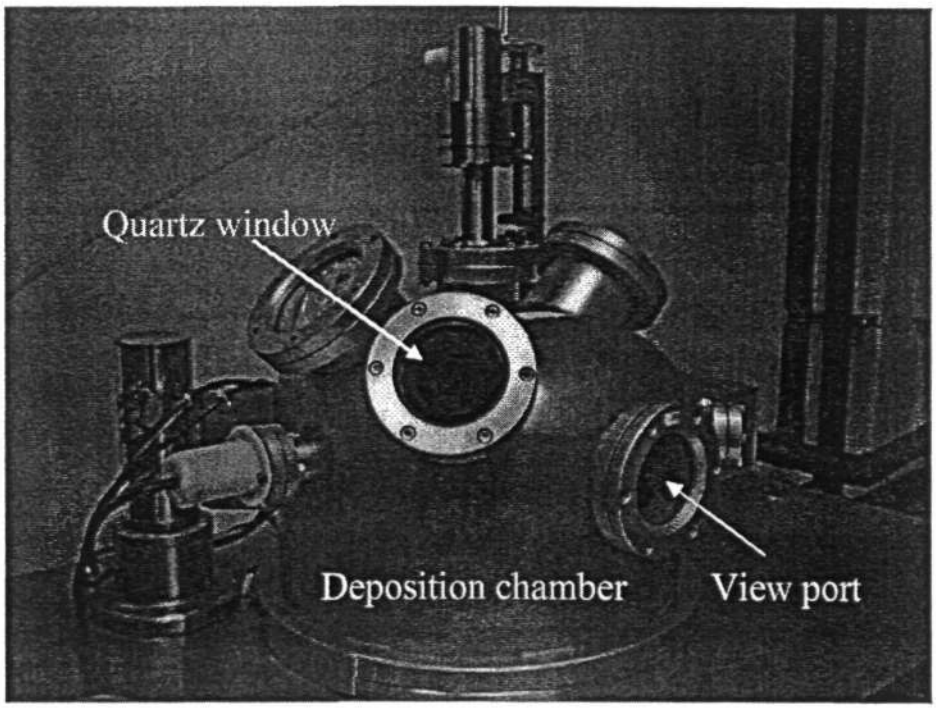

Figure 3-2 Photograph of the pulsed laser deposition chamber.

3.1.2 Target Handling

The target was fabricated by mechanically pressing the GaN powder (Sigma Aldrich 99.99% purity) at a force of 10 tons at room temperature for 2 hours into a solid disc with 5 cm diameter. The target was placed 2 to 4 cm away from the substrate inside the high vacuum deposition chamber. The dimension of the focused laser spot size irradiated on the target was approximately 0.05 cm^2.

3.1.3 Laser

A KrF excimer laser (LAMBDA PHYSIK, Compex 102) operating at a wavelength of 248 nm and pulse duration of 23 ns was used to irradiate the GaN target at laser energies between 100-200 mJ/ pulse (see Fig. 3-3). The laser fluence is calculated by measuring the energy of the laser beam just before the entrance to the deposition chamber with an energy meter, subtracting the losses associated with transmission through the quartz window and dividing this by the area of the spot on the target. Laser fluences reported in this thesis are expected to be accurate to within a possible systematic error of 20%.

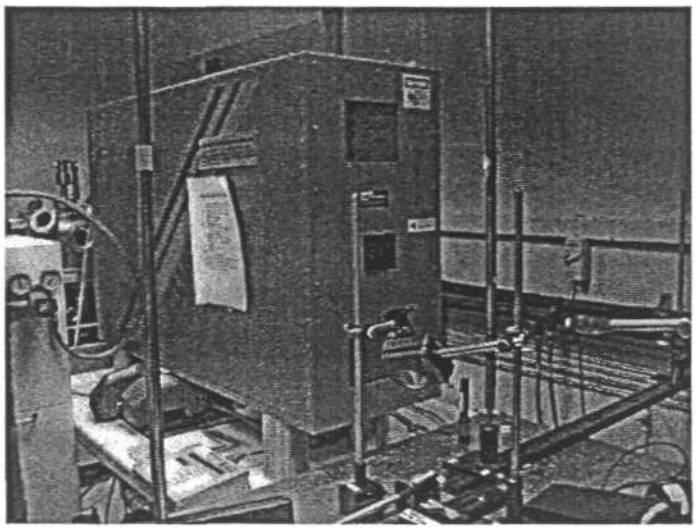

Figure 3-3 Photograph of KrF excimer laser.

3.1.4 Substrate Handling

Silicon and fused silica substrates were used to deposit Ga_2O_3 nanoparticles and nanowires. Prior to deposition, the substrates were cleaned and degreased using acetone, ethanol and de-ionized water.

The substrate heater (see Fig. 3-4) is a 2" diameter disk with a filament wounded behind the disk plate. The filament is resistively heated by applying a constant voltage, which can be adjusted to achieve the desired temperature. Temperature is measured on the surface of the heater with a thermocouple, embedded in a solidified ceramic paste. The samples were attached onto the substrate heater with Ag paste. For Ga_2O_3 nanoparticles and nanoclusters, PLA was conducted at room temperature on blank silicon or quartz substrates for 5 to 20 mins.

The synthesis of Ga_2O_3 nanowires was more involved. First the substrate has to be coated with a suitable metallic film that acts as a catalyst. This is achieved using an e-beam evaporator (BOC Edwards, Auto 306). The substrate heater was heated to 400-800°C at a ramp rate of 20°C/min with flowing N_2 or O_2. The laser ablation of the target lasted between 5 to 20 mins at that temperature and nanowires were grown on the substrate.

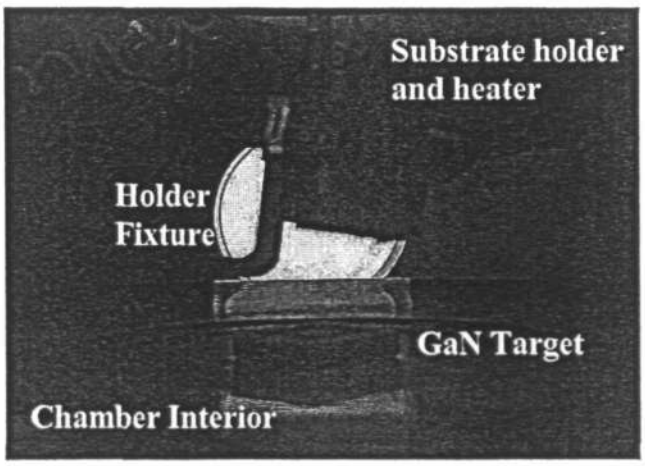

Figure 3-4 Photograph of deposition chamber's interior.

3.2 Laser Annealing of Ga_2O_3 Nanoparticles and Nanoclusters

The laser-synthesized Ga_2O_3 nanoparticles were laser annealed in air and at room temperature. A pulsed KrF excimer laser (Lambda Physik, Compex 102, $\lambda = 248$ nm) was employed to perform laser annealing of the nanoparticles. In this experiment, laser pulses and laser fluence were varied to study the effects of laser annealing on the morphology, crystal structure and photoluminescence of the amorphous Ga_2O_3 nanoparticles and nanoclusters. A schematic of the experimental setup is illustrated in Fig. 3-5.

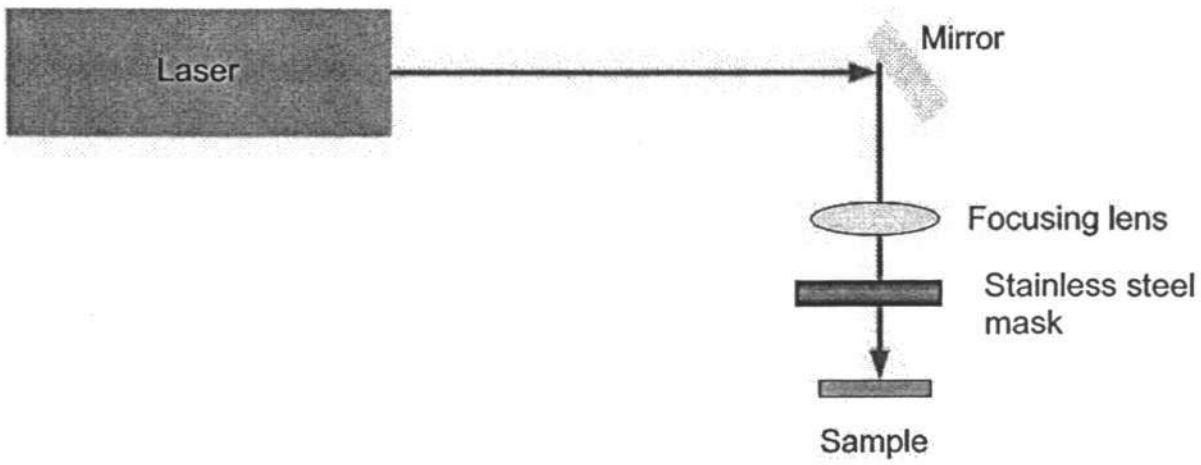

Figure 3-5 Schematic of laser annealing setup.

3.3 Ga_2O_3 Nanoparticle, Nanocluster and Nanowire Characterization

After synthesis, the Ga_2O_3 nanoparticles, nanoclusters and nanowires were characterized using Field Emission Scanning Electron Microscopy (FESEM), Energy Dispersive X-Ray Spectroscopy (EDX), Transmission Electron Microscopy (TEM) including High Resolution TEM (HRTEM) and Selected Area Electron Diffraction (SAED), X-Ray Diffraction (XRD), Raman Spectroscopy, X-Ray Photoelectron Spectroscopy (XPS) Photoluminescence (PL) Spectroscopy, and UV-vis Absorption Spectroscopy. The following sections briefly describe these various characterization techniques.

3.3.1 Scanning Electron Microscopy

The as-synthesized Ga_2O_3 nanoparticles, nanoclusters and nanowires were viewed under a field emission scanning electron microscope (FESEM, JOEL JSM 6340F). As Ga_2O_3 nanomaterials are not conductive, the samples were coated with an extremely thin layer of Au of a few angstroms in a sputter coater before observation under the FESEM. The operating principle in a scanning electron microscope (SEM) is focusing an electron beam as a spot on the sample to be investigated, and scanning this spot across the sample. Each point struck by the spot produces a response (secondary electrons), which is collected and displayed to give an image. The as-synthesized Ga_2O_3 nanomaterials were imaged in an FESEM to determine their length, diameters and size distributions. The FESEM is also equipped with an Energy Dispersive X-ray (EDX) spectrometer that was used to determine the elemental composition of the nanomaterials. However, there is a spatial limitation in the area from which the detection can be made. In a typical SEM coupled with EDX, the smallest specimen area from which the X rays can be sampled is 3 μm x 3 μm. In

addition, there is a limitation in determining the precise concentration of elements lighter than oxygen. Thus due to the lower detection limits and orders of magnitude difference in the EDX spot size, higher resolution imaging and compositional analyses of Ga_2O_3 nanoparticles and nanowires were carried out in a TEM.

3.3.2 Transmission Electron Microscopy

The composition, phase and crystal structure of the Ga_2O_3 nanomaterials were studied under a transmission electron microscope (TEM, JEM 2010). Samples for TEM analysis were prepared by physically scraping the nanomaterials from the substrates, dispersing them in ethanol or isopropyl alcohol (IPA) in an ultrasonic bath, and subsequently dropping the suspension on a holey carbon TEM grid.

TEM is a powerful technique for crystal structure characterization with real space imaging resolution of 1 Å. The TEM operates on the same fundamental principles as an optical microscope but uses electrons instead of light. TEM uses electrons as the light source and the small wavelength of the electrons causes the atoms in a crystal to act as diffracting centers. Thus, the electron beam provides information about the lattice spacing in a crystal. The underlying principle of TEM is built upon this idea and uses a beam of highly focused electrons to be directed toward a thinned sample to gather information about the sample. A schematic of a TEM is shown in Fig. 3-6. The electron beam is focused to a small, thin and coherent beam by the use of two condenser lenses and a condenser aperture before passing through the sample. The condenser aperture helps in knocking out any of the high angle electrons. The highly energetic incident beam then interacts with the atoms in the sample to produce both diffracted and transmitted electrons. The sample needs to be thinned enough to allow

the electrons to be transmitted through the sample much like the light being transmitted through the materials in a conventional optical microscope.

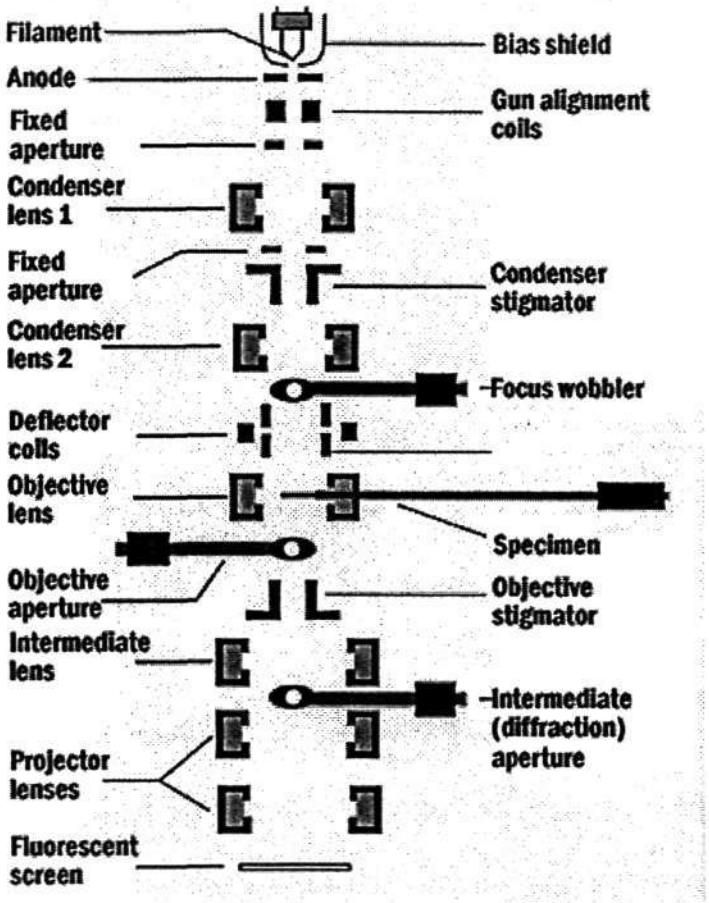

Figure 3-6 Schematics of a TEM system.

The transmitted portion of the electrons is focused to an image by the objective lens. The objective aperture is placed after the objective lens to knock out any high angle diffracted electrons. This helps in enhancing the contrast of the image. The electrons are then passed through a series of two intermediate lenses and a projector lens to form the magnified image of the sample on a phosphor screen. There is also a selected area aperture present right after the objective aperture, which can be taken out or put in the path of the transmitted beam enabling the user to get diffraction information

from the sample. The highly energetic incident electrons interacting with the atoms in the sample and producing both diffracted and transmitted electrons can provide valuable information about the material phase, size, shape and compositional information of the particles. X-ray diffraction is a complementary technique to TEM. It provides the user with diffraction information of the sample, from which the phase of the material can be discerned. The working of XRD is similar to TEM but differs in the mechanism in which the X-rays interact with the material.

3.3.3 X-ray diffraction (XRD)

In this work, a general purpose X-ray diffractometer (Shimadzu, LabX XRD-6000) with a vertical goniometer, was used to identify and study the crystalline phases in Ga_2O_3 nanomaterials. The installed vertical goniometer allows measurement of powder and thin film samples.

XRD is a powerful tool for studying the arrangement of atoms in a crystal. X-rays are electromagnetic radiation whose wavelength are of the order of 1 Å. Max Von Laue was the first person to hit upon the idea that a crystalline solid consisting of a regular array of atoms can form a natural diffraction grating for the X-rays whose wavelengths are about equal to atomic diameters. The atomic planes of a crystal cause an incident beam of X-rays to interfere with one another as they leave the crystal and form a characteristic interference pattern. This phenomenon is called X-ray diffraction. Diffraction occurs at different angles for different planes. The diffraction condition is satisfied by Bragg's law, which is given by

$$\lambda = 2\, d \sin\theta\,, \qquad (3.1)$$

where λ is the wavelength of the X-ray, d is the interplanar spacing and θ is Bragg's angle (angle of incidence equal to angle of diffraction).

The diffraction pattern which is formed by diffracted or reflected beams can be used to study the interplanar spacings of various crystal planes. The intensities of distinct peaks from a material vary for different interplanar spacing and each diffraction angle has corresponding Miller indices (hkl). X-ray diffraction is a complementary technique to TEM.

3.3.4 Raman Spectroscopy

Raman spectroscopy of Ga_2O_3 nanoparticles was also analyzed using a dual source imaging micro-Raman spectrometer (Renishaw System 200). In the case of Ga_2O_3 nanowires, Raman signals could not be obtained due to the small quantities of the sample. Raman spectroscopy provides useful information on the vibrational, rotational, electronic and other frequency modes in a material. It involves illuminating a sample with monochromatic light and using a spectrometer to examine light scattered by the sample. At the molecular level, photons can cause either elastic or inelastic scattering in materials. The elastic process is termed as Rayleigh scattering, whereas the inelastic process is known as Raman scattering. The electric field component of the scattering photon perturbs the electron cloud of the molecule and may be regarded as exciting the system to a 'virtual' state. Raman scattering occurs when the system exchanges energy with the photon and the system subsequently decays to vibrational energy levels above or below that of the initial state. The frequency shift corresponding to the energy difference between the incident and scattered photon is termed as the Raman shift. The shift in energy gives information

about the phonon modes in the system. A plot of the detected number of photons versus Raman shift from the incident laser energy constitutes a Raman spectrum. Different materials have different vibrational modes, and therefore result in characteristic Raman spectra. A microscope is used to focus the laser beam. Light from the sample passes back through the microscope optics into the spectrometer. Raman shifted radiation is detected with a charged-coupled device (CCD) detector and a computer is used for data acquisition.

Interesting phenomena take place in materials at the nanometer scale. For example, quantum confinement causes silicon to change from an indirect energy bandgap material to a direct energy bandgap material. These quantum confinement effects can be easily detected with Raman spectroscopy [135]. In addition, materials may exhibit different phases at the nanometer scale, and this can also be characterized using Raman spectroscopy.

3.3.5 X-Ray Photoelectron Spectroscopy

The chemical compositions of laser-synthesized Ga_2O_3 nanoparticles and nanoclusters were investigated using a scanning ESCA (Electron Spectroscopy for Chemical Analysis) microprobe (PHI Quantum 2000). When a material is exposed to electromagnetic radiation of sufficiently high energy, the emission of electrons is observed. This phenomenon is known as the photoelectric effect. A high energy photon, with $h\nu$ significantly in excess of the threshold energy $h\nu_o$, may be capable of separating one photon/one electron photoionization events by ionizing different species of electrons having various ionization energies $I_k < h\nu$. One photon may eject a very loosely bound electron, imparting high kinetic energy to it, while another photon of same energy might ionize a more tightly bound species of electron and

produce a photoelectron of lower kinetic energy. Since the energy levels occupied by electrons are quantized, the photoelectrons have a kinetic energy distribution n(E), consisting of a series of discrete bands, that essentially reflect 'shell' form of the electronic structure of the sample. The experimental determination n(E) by a kinetic energy analysis of the photoelectrons constitutes photoelectron spectroscopy. Ejection of photoelectrons is a very direct way of obtaining information, characteristics of atoms. If high enough excitation energy is provided, core level spectra can be obtained for all elements in the periodic table except H and He and the determined binding energies of these core levels are sufficiently unique for their unambiguous identification. XPS will give valuable information about the surface functionalities, compositions and chemical states of the material.

3.3.6 UV-Vis Absorption Spectroscopy

For this research, the UV-vis spectra of Ga_2O_3 nanoparticles and nanoclusters were obtained with UV-Vis-NIR scanning spectrophotometer (Shimadzu, UV-3101PC). The light source is a deuterium discharge lamp for UV measurements and a tungsten-halogen lamp for visible and NIR (near-infared) measurements. It has a double monochromator equipped with two sets of switchable blazed holographic gratings to deliver high energy throughout the entire wavelength (190-3200 nm).

UV-vis absorption spectroscopy is the measurement of the attenuation of a beam of light after it passes through a sample or after reflection from a sample surface. Many materials absorb ultraviolet or visible light. The absorbance of a material increases as the attenuation of the beam increases. Absorbance is directly proportional to the path length b and the concentration c of the absorbing species.

Beer's Law states that

$$A = \varepsilon bc\,, \tag{3.2}$$

where ε is a constant of proportionality and A is the absorptivity.

The absorption of UV or visible radiation corresponds to the excitation of outer electrons to higher energy levels. When an atom or molecule absorbs energy, electrons are promoted from their ground state to an excited state. In a molecule, the atoms can rotate and vibrate with respect to each other. These vibrations and rotations also have discrete energy levels, which can be considered as being packed on top of each electronic level (see Fig. 3-7).

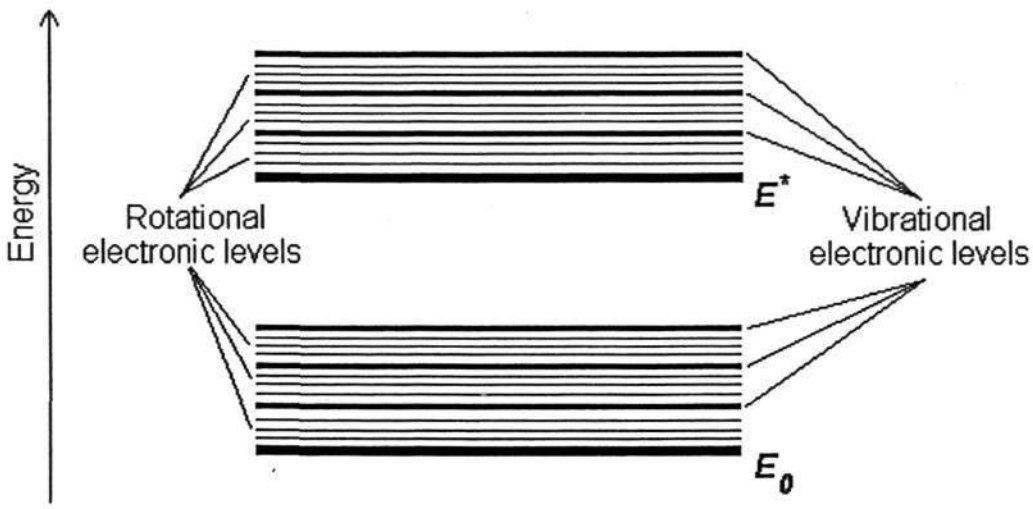

Figure 3-7 Rotational and vibrational electronic levels of atoms

A typical absorption spectrum will show a number of absorption bands corresponding to the structural groups within the material and absorption measurements can be at a

single wavelength or over an extended spectral range. UV-vis spectroscopy is usually applied to molecules and inorganic complexes in solution. Additionally, the UV-vis spectra can also be used for characterization of the optical or electronic properties of materials.

3.3.7 Photoluminescence Spectroscopy

Photoluminescence (PL) spectra were obtained with a fluorescence spectroflurophotometer (Shimadzu RF-5301PC) at room temperature. Optical excitation was provided by a 150W Xenon arc lamp dispersed by a monochromator. The luminescence spectra were recorded by a secondary monochromator. The excitation light wavelength ranged from 266 nm to 325 nm. The emission light wavelength was detected in the range from 300 to 500 nm. Excitation and emission slits were 3.5 nm and 5 nm respectively. No optical filters were used for collecting the room temperature PL spectra. Low temperature PL spectra were obtained with another system that consists of a continuous flow cryostat system (JANIS ST-100) and a He-Cd laser (Kimmon, IK3023R-BR, λ = 325 nm). The luminescence spectra were also recorded by a monchromator. Photoluminescence spectroscopy is a contact-free, non-destructive method of probing the electronic structure of materials. When light of sufficient energy is incident on a material, photons are absorbed and electronic excitations are created. The excess energy that is transferred into the material atoms causes the electrons to get pumped from the valence band to the conduction band. This process is called photo-excitation. Since the atoms get disturbed away from their equilibrium states, the absorbed energy could be dissipated through the radiative recombination of the excess electrons and holes, which emits light. The intensity and spectral content of the luminescence provides information on

the relative rates of the radiative and non-radiative recombination and the electronic energy levels of the samples.

3.4 Data Analysis Technique

3.4.1 Analysis method to determine diameter and length of nanoparticles and nanowires

The length of the nanowires was measured using an image analysis software (UTHSCSA ImageTool, version 3.0) where the scale bars on the SEM micrographs were calibrated to determine the actual length of the nanowires. For each condition, 50 nanowires were measured using the software, taking into consideration 10% in error measurement.

3.4.2 Analysis method to determine diameter and length distribution data of nanoparticles and nanowires

Determining the 'right' sample size is a very important issue because a sample size that is too large may require too much time, resources and money, while a sample size that is too small may lead to inaccurate results. In each sample, a total of 200 nanoparticles or nanowires had been counted to get the distribution data. For instance, 40 nanoparticles or nanowires were counted at five different locations on the sample, namely Left, Right, Center, Top and Bottom; to ensure that the distribution data is adequate and accurate.

CHAPTER 4

Room-temperature Synthesis of Ga_2O_3 Nanoparticles and Nanoclusters by Pulsed Laser Ablation

4.1 Introduction

Nanoparticles and nanoclusters containing a few to thousands of atoms, play an important role in modern physics and technology. They have been extensively investigated due to their unique and superior electrical, magnetic, optical and chemical properties which are different from quantum objects (atoms and molecules) and macroscopic bulk materials [136-138]. In fact, the benefit arising from the size-dependent properties of these tiny particles has been one of the important driving forces in nanotechnology. Hence, the synthesis of nanometer size clusters and particles of electronic and optical materials becomes an important aspect of the applied physics of materials for new devices.

Several methods have been developed to fabricate nanoclusters and nanoparticles, e.g. mechanical (ball milling) [139], template based [140], sol-gel [141] and gas phase processes (gas condensation, chemical vapor deposition) [142] where the nanoparticles are usually condensed from an oversaturated vapor. However, some disadvantages of these methods include long processing time, inefficient collection of nanoparticles and nanoclusters and contamination from the liquid, crucible and/or reactants. On the contrary, the pulsed laser ablation technique is a very promising approach for fast and contamination-free deposition of nanoparticles of various materials under a very wide range of growth conditions, thereby opening new prospects for the synthesis of novel nanostructured materials [143-145]. Unlike pulsed laser deposition of thin films, laser ablation and condensation of nanoclusters and

nanoparticles is carried out at relatively high pressures (> 1 Torr). The ablated material leaves the surface of the target explosively, and is highly energetic but quickly loses most of its energy through collisions with the background gas molecules. As the ablated materials thermalize, they condense into clusters. By choosing the appropriate growth conditions such as laser fluence, growth pressure and temperature, the size of the condensing nanoclusters and nanoparticles can be controlled accordingly. More importantly, nanoparticles with diameters considered unfavorable thermodynamically can be easily obtained. For example, the growth of Si nanoparticles with a narrow size distribution by the pulsed laser ablation technique has been studied for the development of new optoelectronic devices [146]. In addition, this technique has been successfully employed in the synthesis of both metallic [147] and semiconducting [148] nanoparticles and nanoclusters.

For the first time, this work investigates the room-temperature pulsed laser ablation of a GaN target in N_2 and O_2 ambients for the bulk synthesis of Ga_2O_3 nanoclusters and nanoparticles without the use of catalysts or template confinement. The experimental results highlight the relationship between the processing parameters and characteristic features of the Ga_2O_3 nanoparticles and nanoclusters generated by pulsed laser ablation technique. The effects of the deposition parameters such as growth pressure, deposition gas and laser fluence on the size, shape, degree of aggregation and crystallinity of Ga_2O_3 nanoparticles and nanoclusters are discussed in detail in section 4.3. Optical properties of the Ga_2O_3 nanoparticles and nanoclusters will be further discussed in Chapter 5.

4.2 Experimental

A pressed GaN powder target (Sigma Aldrich, 99.99% purity), N_2 (99.9995% purity) and O_2 (99.99% purity) was used for the synthesis of the Ga_2O_3 nanoparticles and nanoclusters. A pulsed KrF excimer laser (Compex 102, LAMBDA PHYSIK) operating at a wavelength of 248 nm, pulse duration of 23 ns, and pulsed energies ranging from 100 to 200 mJ per pulse was used to ablate the GaN target in a high-vacuum chamber (see Fig. 3-1). The laser beam was focused on the GaN target at an incident angle of 45°. The target was rotated about its axis to ensure uniform ablation of the target. The target-to-substrate distance was varied between 2 to 4 cm to operate in different pressure regimes. P-type (100) silicon and quartz substrates were cleaned with acetone and IPA and attached onto the substrate heater with Ag paste in the high-vacuum chamber. The chamber was pumped down to a base pressure of 3×10^{-5} Torr and N_2 or O_2 was slowly introduced into the chamber to maintain a pressure of 1 to 100 Torr during laser ablation. The nanoparticles and nanoclusters collected on the substrates were characterized using an X-ray diffractometer (XRD, Shimadzu LabX XRD-6000) with Cu-Kα radiation, transmission electron microscopy (TEM, JEM 2010) and field emission scanning electron microscopy (FESEM, JOEL JSM 6340F). In addition, Raman (Renishaw System 200) and X-ray Photoelectron (PHI Quantum 2000) spectroscopy were performed to study the vibrational modes and chemical compositions of the as-synthesized Ga_2O_3 nanomaterials, respectively.

4.3 Control of size, morphology and crystalline phase of Ga_2O_3 nanomaterials

4.3.1 Effect of Growth Pressure and Deposition Gas

In this study, the effect of growth pressure on the surface morphology of the Ga_2O_3 nanoparticles and nanoclusters generated via pulsed laser ablation of GaN was investigated while other parameters such as laser fluence, repetition rate and deposition time were kept constant. The influence of N_2 and O_2 on the surface morphology and crystallinity of Ga_2O_3 nanoparticles is also examined. Figure 4-1 depicts the FESEM images of the room-temperature growth of Ga_2O_3 nanoparticles and nanoclusters at various deposition pressures in N_2. The FESEM images reveal aggregation of nanoclusters and nanoparticles. Large and irregular shaped clusters were formed at 1 and 5 Torr (see Fig. 4-1a and b). At pressures above 10 Torr, porous, chain-like but connected nanostructures with smaller nanoparticles were formed randomly and abundantly on the substrate. Figure 4-1(c) and 4-1(d) show the porous, chain-like nanostructures grown at 10 and 100 Torr, respectively. As shown in the higher magnification FESEM images in Fig 4-2(a), the chain-like aggregates consist of individual spherical and ellipsoidal nanoparticles aggregated one-dimensionally. EDX spectra of the Ga_2O_3 chain-like nanoparticles deposited at 10 Torr in N_2 ambient is presented in Fig. 4-3. It clearly indicates the chemical compositions of the nanoparticles consist of gallium and oxygen atoms. That little or no nitrogen atom is present in the sample confirms the formation of Ga_2O_3 nanomaterials during laser synthesis in an N_2 ambient. The silicon peak in the EDX spectra originates from the silicon substrate and the gold peak originates from the sample preparation step where a thin layer of gold was sputtered onto the sample surface. The purpose of coating a thin layer of gold onto the sample surface before

FESEM analysis is to make the sample conductive and hence a better FESEM image quality can be achieved. The chemical composition of the Ga_2O_3 nanoparticles synthesized at 10 Torr in N_2 ambient was further investigated by X-ray Photoelectron Spectroscopy (XPS). Figure 4-4(a) displays the photoelectron peaks for gallium and oxygen. From the spectrum, the ratio of Ga/O is estimated to be approximately 1: 1.5. In Fig. 4-4(b), the high resolution Ga 3d core level spectrum is shown. The binding energy of the Ga 3d core level is ~ 20.3 eV indicating negligible shift in the binding energy for the nanoparticles deposited in the various conditions. The binding energy positions of the Ga *3d*, Ga $3p_3$ and O *1s* core levels are consistent with the reported data of Ga_2O_3 [149]. Thus, the XPS results support the conclusion that the sample is composed of only stoichiometric Ga_2O_3 when deposited in N_2 ambient.

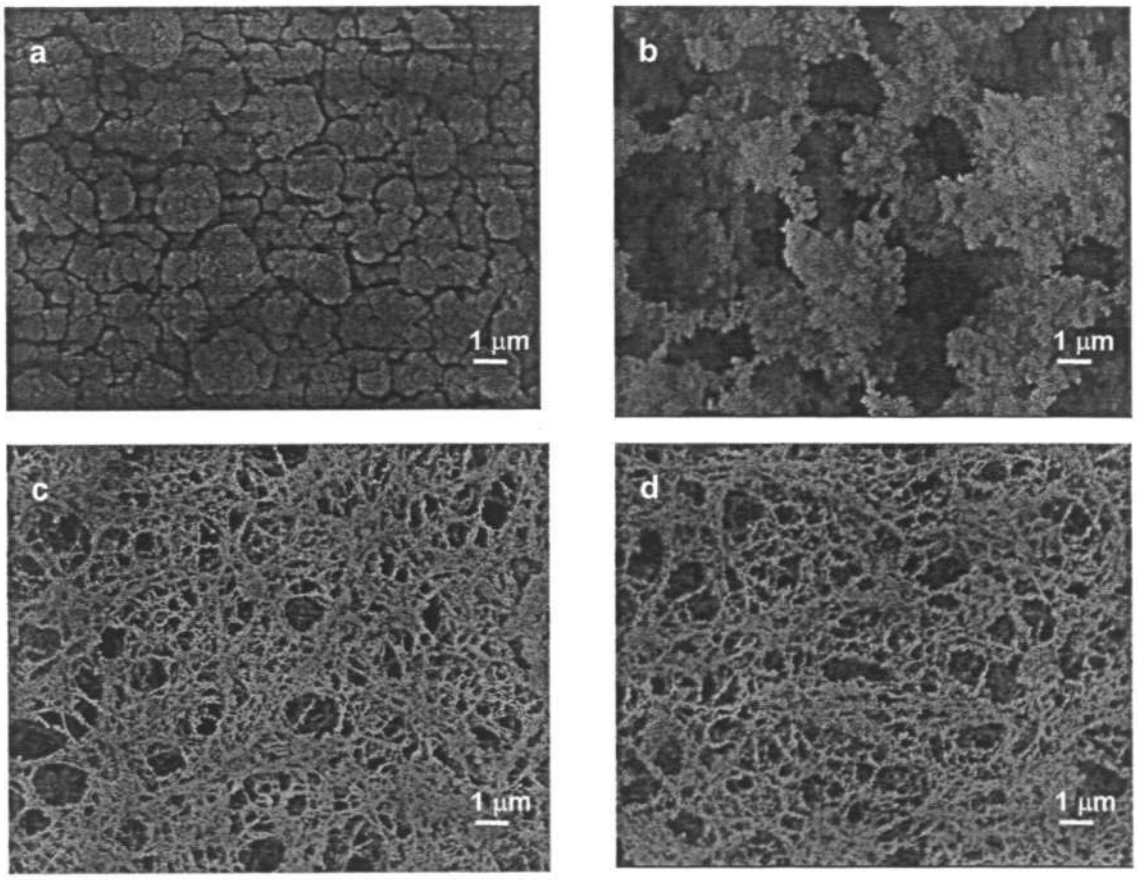

Figure 4-1 FESEM images of Ga_2O_3 nanoparticles deposited at (a) 1 Torr, (b) 5 Torr, (c) 10 Torr, (d) 100 Torr on silicon substrates in N_2 ambient. Laser fluence of 1.3 J/cm^2, repetition rate of 10 Hz and deposition time of 10 minutes were adopted. Scale bar is 1 μm.

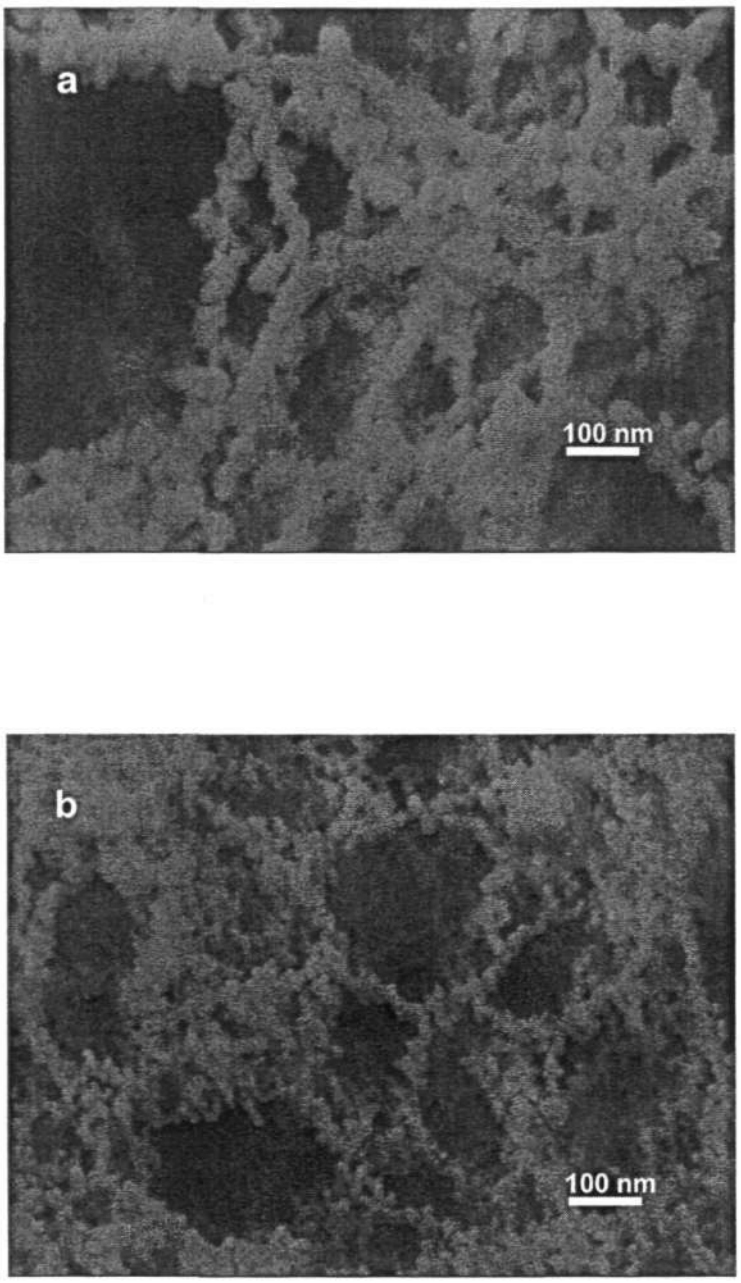

Figure 4-2 High magnification FESEM images of Ga_2O_3 nanoparticles deposited at (a) 10 Torr, (b) 100 Torr on silicon substrates in N_2 ambient. Laser fluence = 1.3 J/cm^2, repetition rate = 10 Hz and deposition time = 10 minutes were adopted. Scale bar is 100 nm.

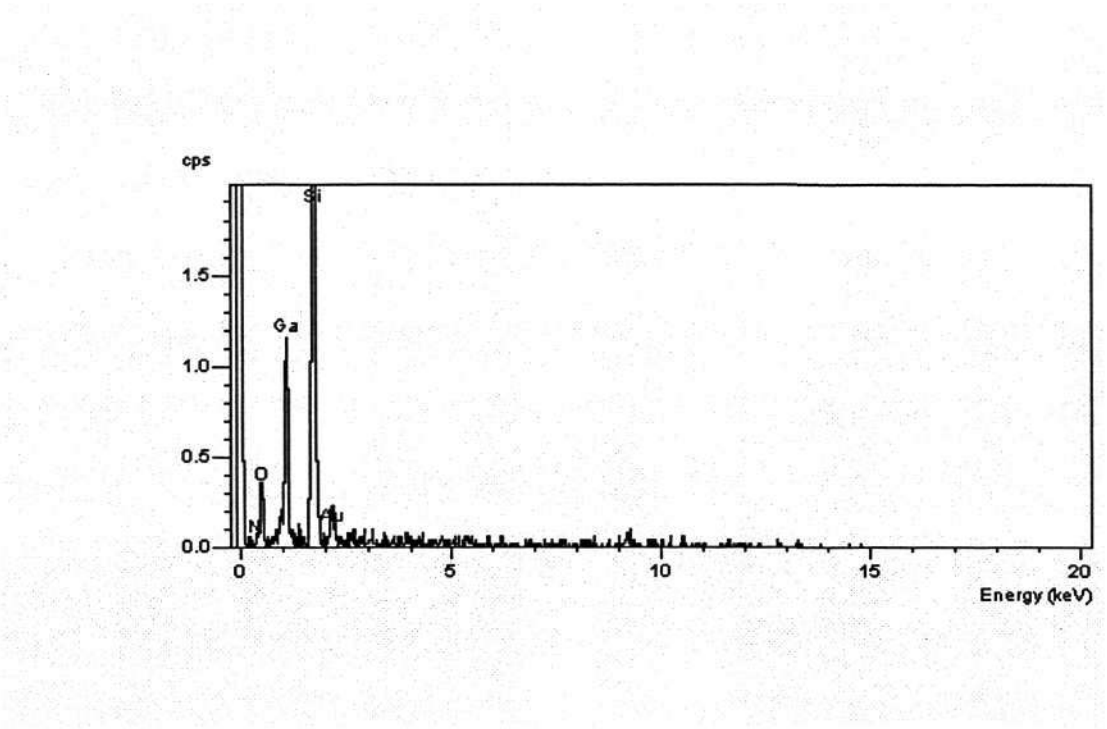

Figure 4-3 EDX spectra of the as-deposited Ga_2O_3 nanoparticles at 10 Torr in N_2 ambient at room temperature.

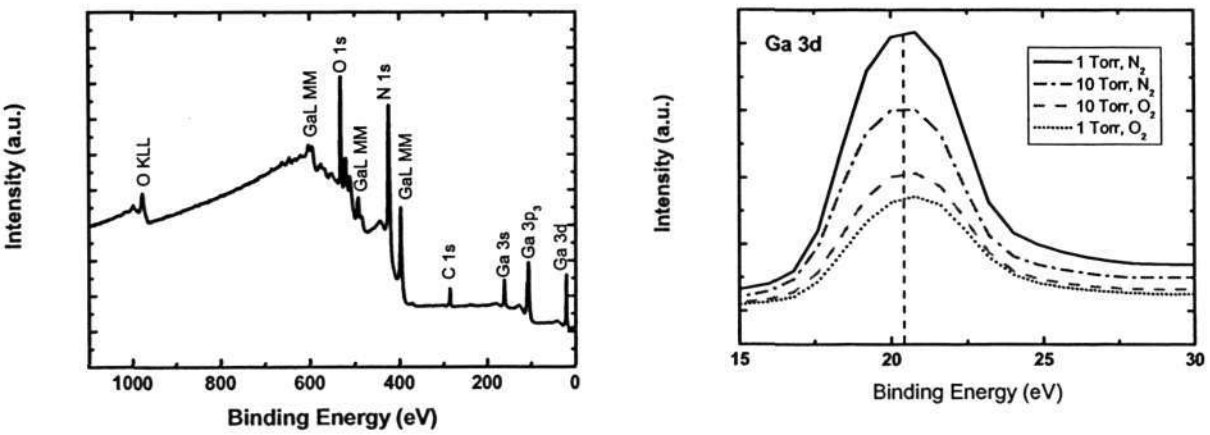

(a) (b)

Figure 4-4(a) X-ray photoelectron survey spectra of Ga_2O_3 nanoparticles deposited at 10 Torr in N_2 ambient. (b) Ga 3d core level spectrum.

Figure 4-5 shows the surface morphology of the Ga_2O_3 nanomaterials deposited in O_2 ambient at 1 Torr and 10 Torr which is similar to that synthesized in N_2 ambient. Large nanoclusters are likewise observed for samples synthesized in O_2 ambient at 1 Torr. On the other hand, porous and interconnected chain-like nanoparticles are observed when synthesized at 10 Torr in O_2 ambient. In other words, the results suggest that deposition gas does not influence the surface morphology of the deposited nanoclusters and nanoparticles. However, growth pressure plays a more significant role in controlling the size and degree of aggregation of the nanoclusters

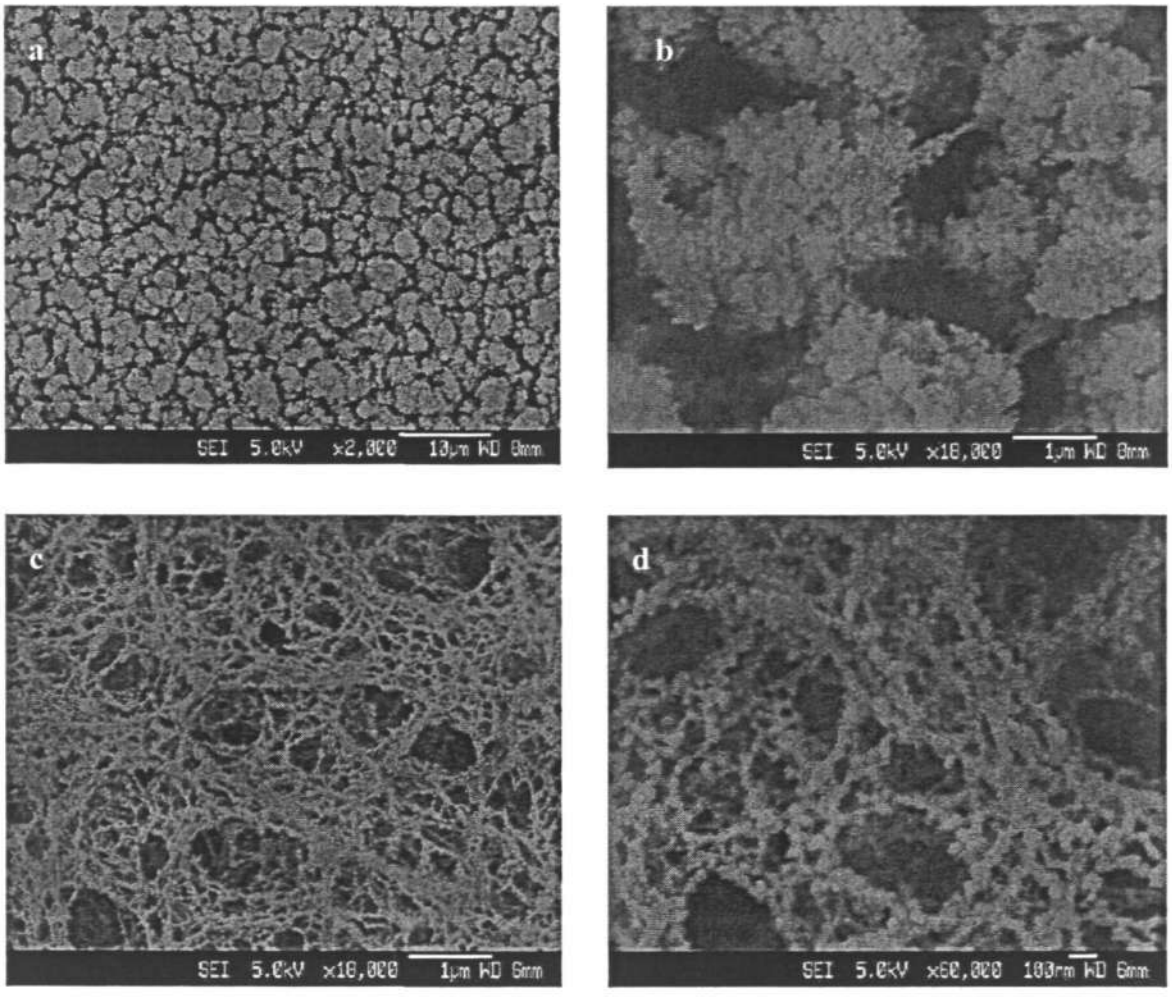

Figure 4-5 FESEM images of Ga_2O_3 nanoparticles deposited at (a) 1 Torr, (b) 1 Torr (higher magnification), (c) 10 Torr, (d) 10 Torr (higher magnification) on silicon substrates in O_2 ambient. Laser fluence of 1.3 J/cm^2, repetition rate of 10 Hz and deposition time of 10 minutes were adopted.

EDX spectra of Ga_2O_3 nanoparticles deposited at 10 Torr in O_2 ambient is presented in Fig. 4-6. Similarly, it indicates that the chemical compositions of the nanoparticles consist of gallium and oxygen atoms, with no apparent nitrogen peak in the sample. Based on the EDX results, the formation of Ga_2O_3 by pulsed laser ablation of GaN in O_2 ambient was demonstrated. As mentioned earlier, the gold peak originates from the sputtered Au film on the sample surface while the silicon peak comes from the silicon substrate.

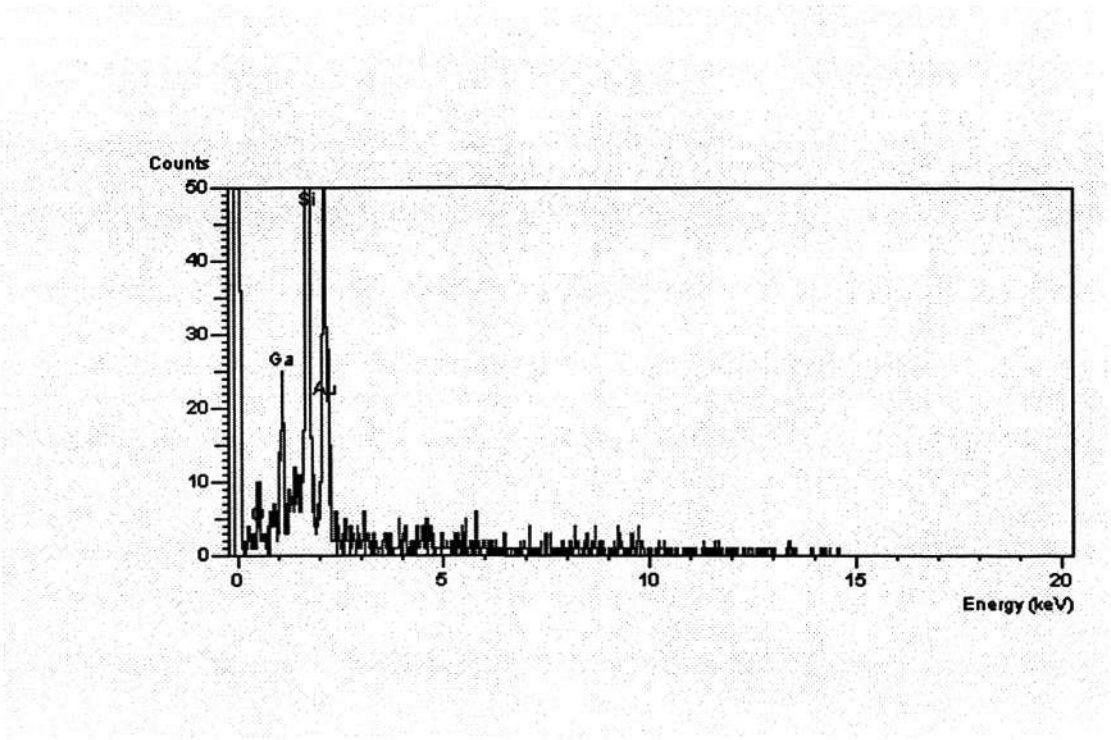

Figure 4-6 EDX spectra of the as-deposited Ga_2O_3 nanoparticles at 10 Torr in O_2 ambient at room temperature.

4.3.2 Growth Mechanism of Ga_2O_3 Nanoparticles and Nanoclusters from Pulsed Laser Ablation of GaN

In general, the formation of nanoparticles and nanoclusters from PLA in an ambient gas is related to the gas-condensation process and it can be explained by the following:

1. Laser irradiation of a solid material results in heating, melting and evaporation of the solid material. If the laser fluence exceeds the ablation threshold of the solid material, superheated vapor (plasma or plume) is formed.
2. The plume consists of atoms, molecules, ionized and neutral species of the solid material. The ablated species collide with the gas atoms at the front of the expanding plume. As a result, species in the plume thermalize normally in 10 – 100 μs after the laser pulse [150]. The rate of thermalization is related to the efficiency of the energy transfer during gas-target atom collisions, which depends on the atomic mass.
3. The cooling plume becomes supersaturated and results in the formation of nanoparticles via homogeneous nucleation. The nanoparticles are subsequently transported to the substrate via a diffusion process. The size of the primary particles can be explained quantitatively by the collision-coalescence theory [151] for particle formation from a gas phase with a certain background pressure. The collision of primary particles at high temperature early in the cooling process results in coalescence. As the gas cools, coalescence ceases and colliding particles tend to form aggregates, which continue to grow by a cluster-cluster aggregation process.

Based on the above discussion, the formation of Ga_2O_3 nanomaterials by pulsed laser ablation of GaN can be explained qualitatively. KrF excimer laser in the UV range, whose photon energy exceeds the bandgap of GaN, generated plasmas with high electronic excitations. Plasma diagnostics has shown that GaN completely decomposed into individual atoms and excited ionic species of Ga, and N [152] upon laser irradiation with KrF excimer laser (λ=248nm). KrF excimer laser dissociates oxygen molecules present in the chamber into atomic O whereas GaN dissociates via the following possible reactions:

$$4GaN\ (s) \rightarrow 4Ga\ (g) + 2N_2\ (g) \qquad (1)$$

$$2Ga\ (g) + 3O\ (g) \rightarrow Ga_2O_3\ (s) \qquad (2)$$

Here, the decomposition of GaN into Ga and N_2 proceeded via a photochemical laser ablation mechanism. The ablated Ga and N_2 species then collided with the deposition gas (N_2 or O_2) and confined them to a certain regime, to form nanoparticles and nanoclusters. It is postulated that the Ga_2O_3 nanoparticles and nanoclusters gas formed in the gas phase within the confinement region away from the substrate and subsequently transported to the substrate via diffusion process. The size and degree of aggregation of the Ga_2O_3 nanoparticles and nanoclusters are controlled by the growth pressure as the extent of plume expansion varies in different pressure regions [153]. As shown in the previous results obtained by EDX and XPS, the as-synthesized products consist of stoichiometric Ga_2O_3 when deposited in both N_2 and O_2 ambient. The reason for the formation of Ga_2O_3 in N_2 ambient is because Ga ions in the plume prefer to react with the surrounding atomic O species or oxygen molecules instead of

N_2 or atomic N species, owing to the higher reactivity of oxygen. The presence of oxygen in the chamber may come from impurities in the N_2 (99.9995%) gas or it may originate from a small amount water vapor or oxygen content present in the chamber or on the chamber wall which could not be efficiently removed when the chamber was evacuated to a base pressure of 3×10^{-5} Torr.

Figure 4-7 shows the X-ray diffraction patterns of Ga_2O_3 samples deposited at 1 and 10 Torr in N_2 and O_2 at a laser fluence of 1.3 J/cm^2. Clearly, the nanoclusters and nanoparticles synthesized at 1 and 10 Torr in N_2 ambient, show little or no crystallinity. During laser ablation, nanoparticles and nanoclusters formed by condensation of vapor undergo cooling and crystallization [154]. At the moment of quenching, the temperature of the nanomaterials is above the melting temperature [15] and the cooling rate of the liquid nanomaterials determines their final structure. If the cooling rate is faster than the crystallization rate, the nanomaterials become amorphous; otherwise they become crystalline. In our case, it is believed the ablated species undergo greater heat transfer and faster cooling when they collide with N_2 molecules than O_2 molecules at 10 Torr because of the higher thermal conductivity of N_2 (26 mWm^{-1}K^{-1}) than O_2 (23.8 mWm^{-1}K^{-1}). From the results, it is deduced that the cooling rate of the ablated species may be faster than the rate of crystallization of Ga_2O_3 when synthesized in N_2 ambient. As a result, samples synthesized in O_2 show higher crystallinity.

The peaks can be indexed to monoclinic Ga_2O_3 (JCPDS Card no. 41-1103) with lattice constants a = 12.227 Å, b = 3.0389 Å, c = 5.8079 Å and β = 103.820°. These values are in good agreement with published values [155]. However, the relative intensity is different, for which the strongest peaks of bulk Ga_2O_3 powder are (004), $(10\bar{4})$ (200), (111) and $(12\bar{2})$ whereas for β-Ga_2O_3 nanoparticles and nanoclusters,

the strongest peaks are only $(11\bar{1})$ and (401). Furthermore, it is apparent from the XRD results that β-Ga_2O_3 nanoparticles, with better crystallinity was achieved when deposited at higher growth pressure. In general, it is known that the background gas pressure changes the density of the excited species in the laser plume [156]. At a higher background pressure, the extent of plume expansion is smaller due to higher resistance of the background gas. Nakata *et al.* has demonstrated that the density of Si increases with increasing He background gas pressures [153]. Furthermore, the temperature of the laser plume rises as their density increases, as assessed by theoretical calculations based on the time-dependent collisional-radiative model for describing the population densities of excited states [157]. Therefore, an increase in the excited species in the laser plume at higher background gas pressure corresponds to the higher temperature synthesis of Ga_2O_3 nanoparticles and nanoclusters, thereby enhancing the formation of the monoclinic phase of the Ga_2O_3, due to more rapid cooling from higher temperatures. From these findings, it is noteworthy that the deposition gas and growth pressure have significant effect on the crystallinity of the synthesized material.

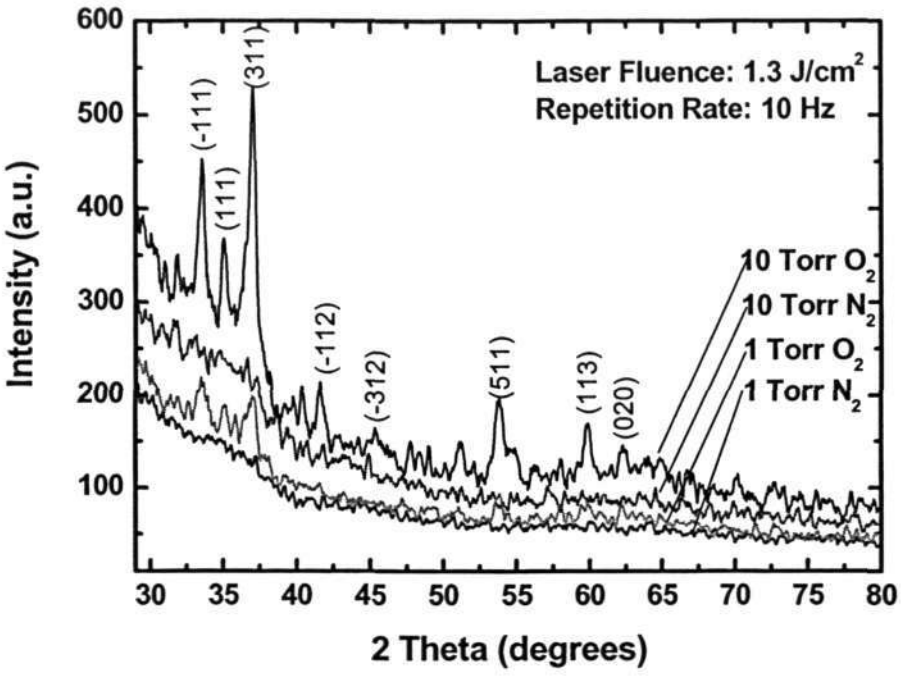

Figure 4-7 XRD patterns recorded on the as-deposited Ga_2O_3 nanoparticles at 1 and 10 Torr in N_2 and O_2 at room temperature.

The effect of growth pressure and deposition gas on the bonding and crystal structure of Ga_2O_3 nanoparticles and nanoclusters was furthered investigated by Raman spectroscopy. Raman spectra were obtained by illuminating the samples with the 514 nm Ar^+ laser. Figure 4-8 shows the room-temperature Raman spectra of the as-received Ga_2O_3 bulk powder compared with Ga_2O_3 nanoparticles and nanoclusters synthesized at 1 and 10 Torr in N_2. To improve the signal to noise ratio, each spectra was obtained from the average over 3 scans. Raman spectra of several locations on the sample surface were also measured and compared to ensure that it is representative of the sample and each measurement was reproduced 2-3 times.

Since β-Ga_2O_3's unit cell contains two formula units-GaO_6 (edge sharing) octahedral and GaO_4 (corner sharing) tetrahedral, 15 Raman active modes are expected in the vibrational spectrum [156]. Eight Raman scattering peaks for the as-

received Ga_2O_3 bulk powder at 200, 321, 346, 416, 474, 630, 653 and 767 cm^{-1} has a monoclinic structure and agree well with that in previous reports [158, 159]. All the Raman peaks correspond to the dual vibration mode (Raman active) because β-Ga_2O_3 belongs to the centrosymmetric C2/m space group [160]. The Raman-active modes of β-Ga_2O_3 can be classified into 3 groups: high-frequency stretching and bending of GaO_4 tetrahedral (~770 – 500 cm^{-1}), mid-frequency deformation of Ga_2O_6 octahedral (~ 480 - 310 cm^{-1}) and low-frequency libration and translation (below 200 cm^{-1}) of tetrahedral-octehedral chains [158].

The Raman peaks for Ga_2O_3 nanoclusters synthesized at 1 Torr in N_2 are located at 275, 490 and 689 cm^{-1}. New Raman peaks located at 261, 332, 412, 458, 637, 684, 742 cm^{-1} are observed for samples synthesized at 10 Torr in N_2 ambient. Low-frequency modes are absent in samples synthesized at 1 Torr in N_2 ambient. For the mid-frequency deformation modes, it is observed that the strong Raman peak at 416 cm^{-1} in bulk Ga_2O_3 powder red-shifted to 412 cm^{-1} for samples synthesized at 10 Torr in N_2 ambient (see Fig. 4-8a). As we know, the redshift of Raman peak in the nanomaterial is usually caused by three factors: a phonon confinement effect caused by the nanosize of the material, defects and strains. The redshift in the phonon frequencies has been attributed to the presence of impurities and defects such as point defects, twins and stacking faults [161]. In our work, Ga_2O_3 nanoparticles and nanoclusters are likely to be oxygen deficient when synthesized in an N_2 ambient, hence the observed redshift may be related to the creation of oxygen vacancies during the deposition process. Dai *et al.* have similarly reported that oxygen vacancies and stacking faults cause an abnormality in the Ga-O bond vibration and led to red-shift in the Raman frequencies [162]. The Raman peaks at 10 Torr become narrower and

more distinct as compared to the indistinguishable Raman peaks at 1 Torr, indicating a strong relationship between crystallinity and Raman spectra.

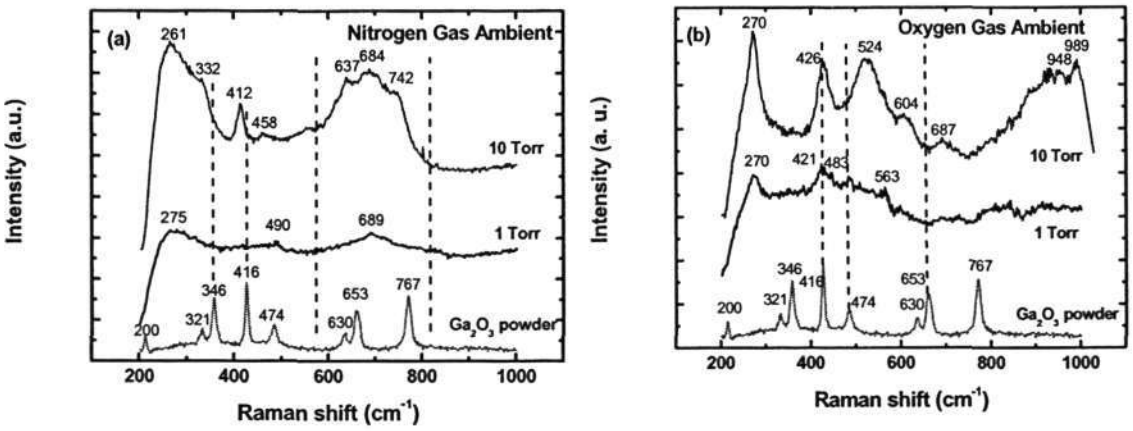

Figure 4-8 Raman spectra of Ga_2O_3 nanoparticles deposited at 1 and 10 Torr in (a) N_2 and (b) O_2 ambient.

Figure 4-8(b) shows the Raman peaks located at 270, 421, 483, 563 cm^{-1} and 270, 426, 524, 604, 687, 948 and 989 cm^{-1} for the nanoparticles and nanoclusters deposited in O_2 at 1 and 10 Torr respectively. For the mid-frequency deformation modes, it is observed that the strong Raman peak at 416 cm^{-1} in bulk Ga_2O_3 powder blueshifted to 421 cm^{-1} and 426 cm^{-1} for samples synthesized at 1 and 10 Torr in O_2 ambient (see Fig. 4-10b) respectively. The blueshift in phonon frequencies of low dimensional materials are often attributed to the quantum size-confinement effect. Since the average diameter of the Ga_2O_3 nanoparticles synthesized at 10 Torr is around 6.5 nm, it is likely that the quantum confinement effect causes the phonon shift up to 10 cm^{-1}. Additionally, new peaks at 524 cm^{-1}, 948 cm^{-1} and 989 cm^{-1} are observed in the Raman spectra for samples synthesized at 10 Torr in O_2 which may be related to additional vibrational modes due to the formation of defects. The Raman peaks for

samples deposited at 10 Torr became narrower and more distinct as compared to samples deposited at 1 Torr in O_2 ambient. Evidently, the Raman results show that the nanoparticles have better crystallinity when deposited in O_2 at 10 Torr as compared to 1 Torr, which is consistent with the XRD results discussed earlier.

Also shown in Fig. 4-8, there is evident broadening of all Raman peaks for both samples synthesized in N_2 and O_2 at 1 and 10 Torr with respect to bulk Ga_2O_3 powder. Broadening and asymmetry of the Raman peaks can be explained by phonon confinement effects. Du *et al.* have reported that the Raman lines of ZnO nanoparticles are slightly broad and asymmetrical with respect to ZnO crystals [163]. Such phonon-confinement effects have also been observed in other nanostructure materials such as Si and GaAs [164, 165].

Low magnification TEM images of the Ga_2O_3 nanoparticles with chain-like nanostructures synthesized at 10 Torr in N_2 and O_2 ambient and at a laser fluence of 1.3 J/cm^2 are presented in Fig. 4-9(a) and (b) respectively. It is obvious from the TEM images that the growth of the chain-like nanostructures proceeds non-uniformly with lengths up to several micrometers. The TEM images are also in good agreement with the FESEM images where the chain-like nanostructures are formed by the coalescence of individual nanoparticles, which are not perfectly spherical. The average diameters of the Ga_2O_3 nanoparticles deposited in N_2 and O_2 are 8.5 ± 1.75 nm and 6.5 ± 1.34 nm respectively. The selected area electron diffraction (SAED) images (inset) in Fig. 4-9 show that the Ga_2O_3 nanoparticles deposited in O_2 has better crystallinity while the nanoparticles deposited in N_2 ambient produce amorphous rings with little or no crystallinity. The SAED results in Fig 4-9(a) and (b) are in excellent agreement with the XRD data discussed earlier.

Figure 4-10(a) presents the low magnification TEM image of Ga_2O_3 nanoparticles deposited at 100 Torr in an N_2 ambient and at a laser fluence of 4.25 J/cm^2. The HRTEM image and SAD inset in Fig. 4-10(b) presents the crystalline nature of the nanoparticles, surrounded by amorphous layers. The HRTEM image also illustrates that individual spherical nanoparticles coalesced to form the chain-like nanostructures with (001) atomic planes. Moreover, the ED recorded perpendicular to the long axis of the nanostructure can be indexed to [110] zone axis. The diffraction pattern analysis and lattice spacing of 0.55 nm also reveal that the nanoparticles consist of monoclinic Ga_2O_3. The effect of laser fluence on the surface morphology and crystallinity of the as-synthesized Ga_2O_3 samples will be discussed further in a later section.

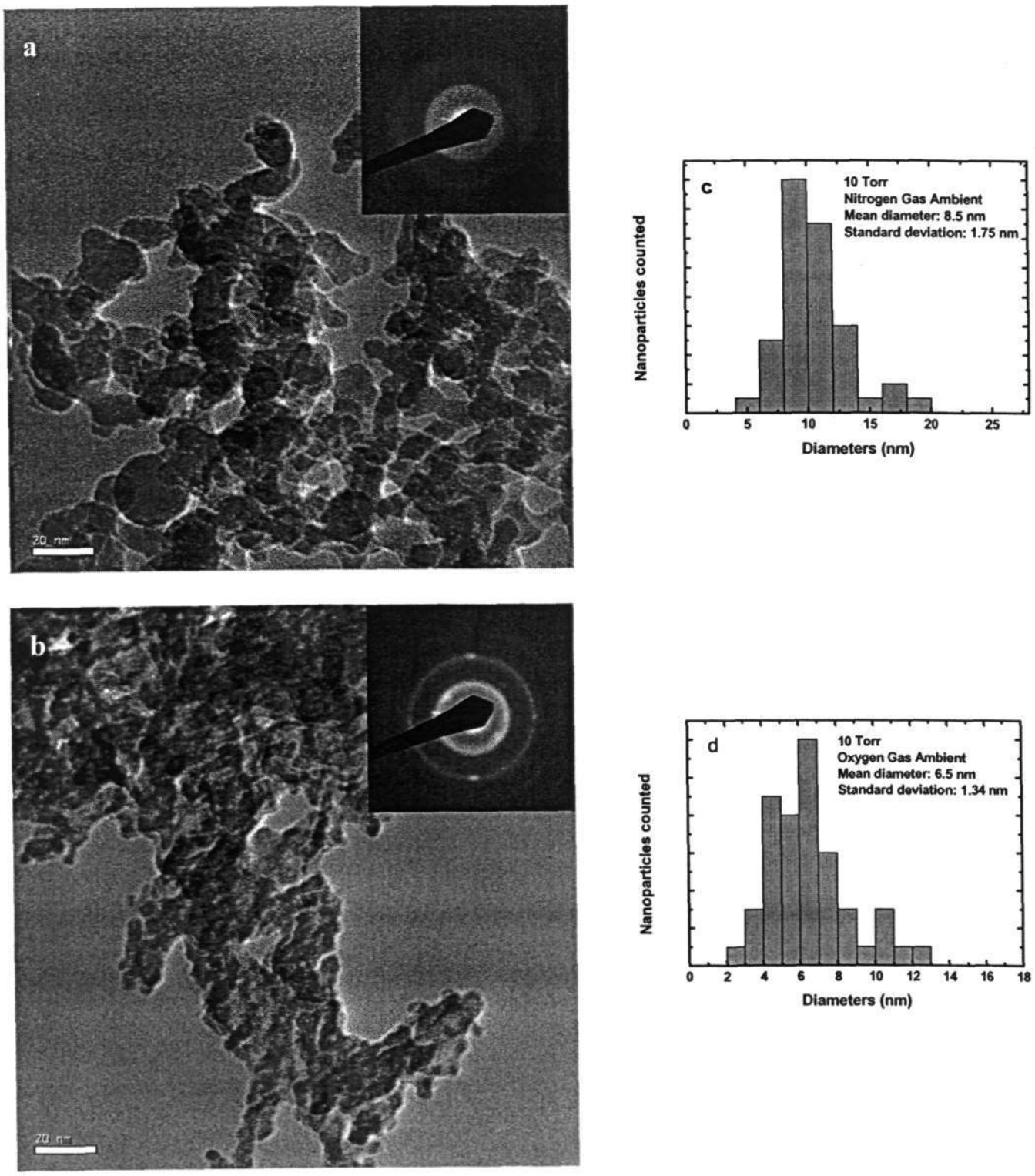

Figure 4-9 TEM images of Ga_2O_3 nanoparticles growth at 10 Torr (a) N_2 and (b) O_2 ambient, at a repetition rate of 10 Hz, deposition time of 10 minutes and laser fluence of 1.3 J/cm^2.

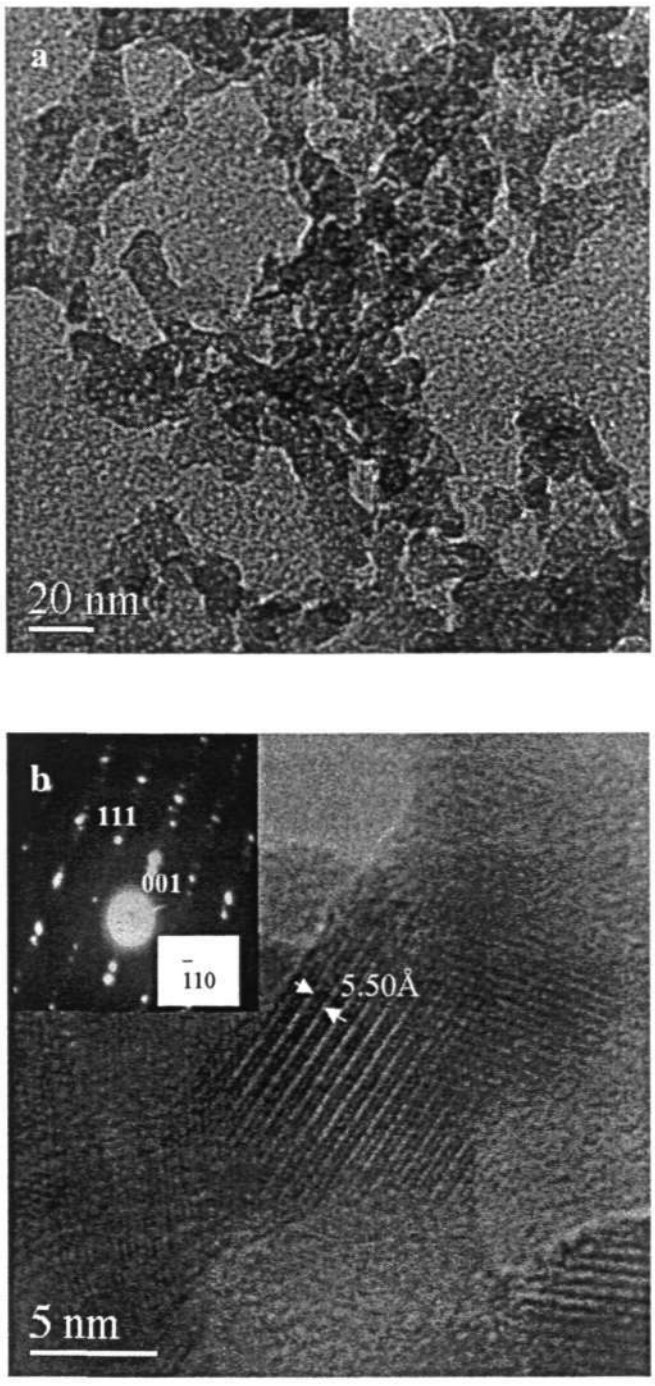

Figure 4-10 (a) TEM images of Ga_2O_3 nanoparticles deposited at 100 Torr in N_2 ambient, at a repetition rate of 10 Hz, deposition time of 10 minutes and laser fluence of 4.25 J/cm^2. (b) Corresponding HRTEM image and selected area electron diffraction pattern (inset) of the Ga_2O_3 nanoparticles deposited at 100 Torr in N_2.

Here, a comparison of the average diameter of chain-like nanoparticles synthesized at 10, 50 and 100 Torr in N_2 and O_2 ambient is illustrated Table 4-1. The as-synthesized samples prepared at 1 and 5 Torr are not included in this study because they consist of large and irregularly shaped clusters in the micrometer range. From the table, it is clearly seen that the average size of the nanoparticles synthesized at 10 Torr in N_2 and O_2 ambient is about 8 ± 1.75 nm and 6.5 ± 1.34 nm, respectively, and the diameter of the nanoparticles increases with increasing growth pressure. These observations suggest that growth pressure plays a dominant role in controlling the size of the nanoparticles.

Table 4-1 Average diameters of Ga_2O_3 nanoparticles synthesized at 10, 50 and 100 Torr in N_2 and O_2 ambient.

	Growth Pressure		
	10 Torr	50 Torr	100 Torr
Nitrogen	8 ± 1.75 nm	15 ± 8.85 nm	35 ± 12.5 nm
Oxygen	6.5 ± 1.34 nm	12 ± 7.53 nm	30 ± 10.64 nm

Evidently, the size of the Ga_2O_3 nanoparticles decreases linearly with decreasing growth pressure. At the same time, the size distribution increases with increasing growth pressure. Our results are in agreement with Yoshida *et al.*'s report where larger Si nanoparticles were obtained at increasing growth pressures, which is due to increased collisions between the ablated species and the ambient gas [166]. Similarly, Sasaki *et al.* reported the preparation of calcium iron complex oxide nanoparticles by PLA using an ArF excimer laser and found that the particle size increased with increasing total pressure of Ar/O_2 gas [167]. Based on the previously discussed results, it is therefore apparent that by varying growth pressure, the surface morphology of the synthesized products such as shape, size and degree of aggregation

of the individual nanoparticles can be effectively controlled at room temperature, without *in-situ* or post annealing treatment performed on the samples. It has also been reported that the formation of the nanoclusters and nanoparticles is strongly influenced by the multiple collisions of the ablated species with the ambient gas where most of the initial kinetic and internal energy of the ablation plume is quenched [168]. Multiple collisions dissipate the kinetic energy of the ablated species which promotes nucleation and growth. Since the probability and frequency of collision between the ejected species and the ambient gas molecules are dictated by the pressure in the chamber, the latter is expected to have a strong influence on the final morphology of the nanoclusters and nanoparticles.

In addition, these Ga_2O_3 nanoparticles agglomerate to form porous chain-like nanostructures at high background gas pressure (≥ 10 Torr), as shown in Fig 4-1(c-d), 4-2 and 4-5. In the nanosecond regime and for low pressures (< 10 mbar or 7.5 Torr), the size and composition of the aggregates strongly depends on the nature and pressure of the background atmosphere. Ga_2O_3 chains instead of 3D clumps (1 Torr) were observed in Fig. 4-5 when synthesized at the growth pressure of 10 Torr and 100 Torr, these experimental results indicate a correlation between the surface nanostructuring and the background gas pressure. An increase in growth pressure (≥10 torr) leads to a decrease in plume expansion volume, causing the probability of collision to increase in the confinement region. Therefore the initial Ga_2O_3 nanoparticles formed in the plume via homogeneous nucleation possess lower kinetic energy upon reaching the substrate when synthesized at higher growth pressure. As such, these nanoparticles have lower surface mobility to reorganize themselves on the substrate to form clump-like of island-like structures. Hence, aggregations of nanoparticles with chain-like structure with big voids between them are found at

higher growth pressures. On the contrary, the formation of island-like structures or 3D clumps are observed (Fig 4-5 a and b) when synthesized at low growth pressure (1 Torr). This is attributed to the fact that when deposited at lower growth pressures, more and more ejected species from the target avoid condensation in the plume. Due to lower probability in collision with the background gas molecules, these ejected species would possess higher kinetic energy when they reach the substrate whereby heterogeneous nucleation begins. To lower their internal energy, the condensed nanoparticles would then diffuse to low energy sites on the substrates to form 3D clumps. All in all, the morphological changes of the Ga_2O_3 nanostructures can be related to the flux of nanoparticles arriving on the substrate and the surface mobility of the nanoparticles.

4.3.3 Effect of Laser Fluence

Figure 4-11 illustrates FESEM images of the as-deposited Ga_2O_3 nanoparticles and nanoclusters at different laser fluences. It is clearly depicted that the size of the nanoclusters increases with higher laser fluence. Nanoclusters with higher particle density are observed when higher laser fluence is employed to ablate the GaN target. When higher laser fluence is employed, more energy is transferred to the target from the laser beam. Consequently, the target is heated to a higher temperature and results in a bigger plasma expansion. Hence, this will result in more material and more atoms being ejected from the target, forming larger nanoclusters that were subsequently deposited on the substrate. Figure 4-12 shows the XRD patterns of the nanoparticles deposited at laser fluence of 1.3 J/cm^2 and 2 J/cm^2. The XRD patterns show that nanoparticles deposited at higher laser fluence exhibit better crystallinity. Shim *et al.* also confirmed that increasing the laser fluence enhances the crystallinity and

stoichiometry of GaN films deposited by pulsed laser ablation at room temperature [169]. When laser fluence is increased, the ejected species generated by laser ablation possessed higher kinetic energy, thereby promoting an increase in surface mobility of the atoms diffusing over the surface. This could enhance crystallization of Ga_2O_3 nanoclusters.

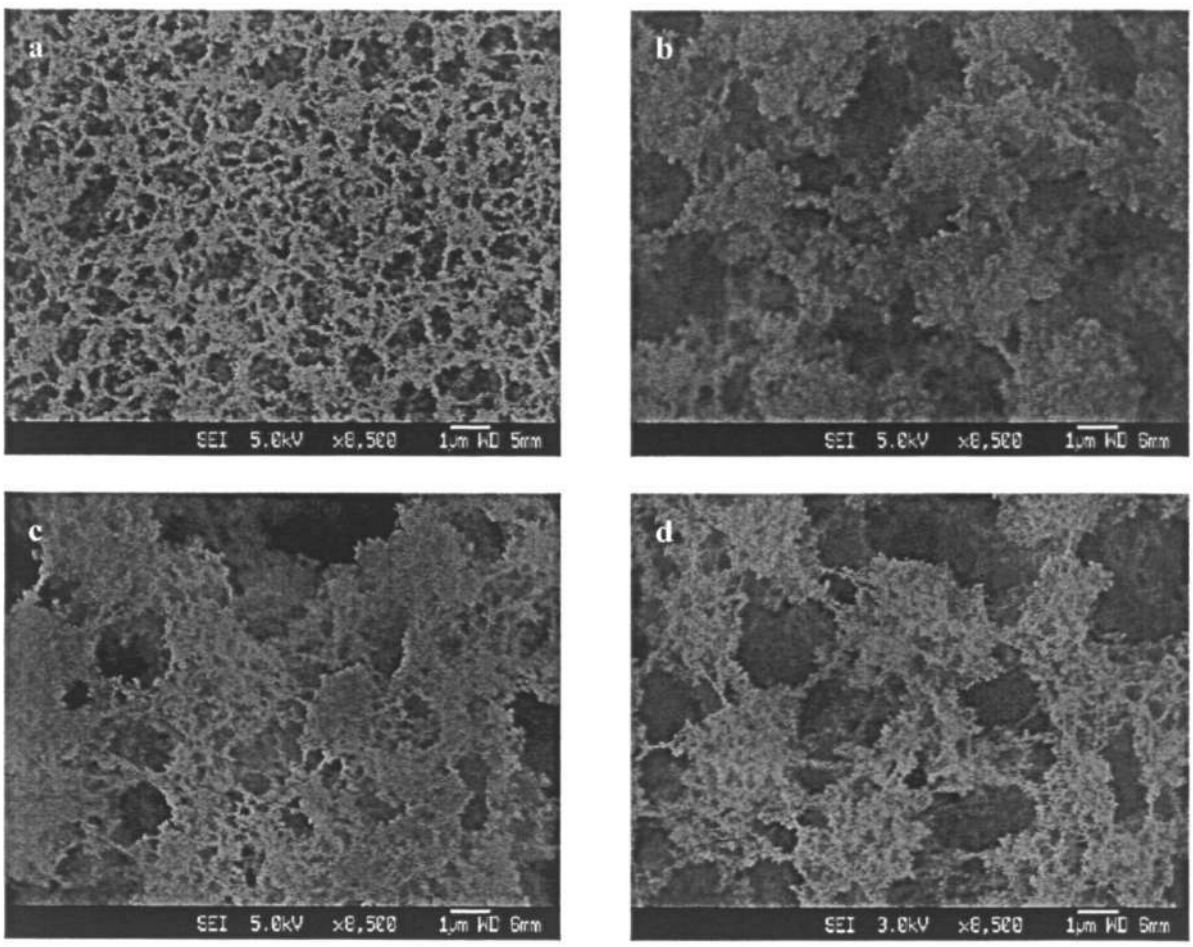

Figure 4-11 FESEM images of Ga_2O_3 nanoparticles deposited at various laser fluences (a) 2 J/cm^2 (b) 3.8 J/cm^2 (c) 4.7 J/cm^2 (d) 5.5 J/cm^2 at 5 Torr chamber pressure, repetition rate = 10 Hz, deposition time = 10 minutes.

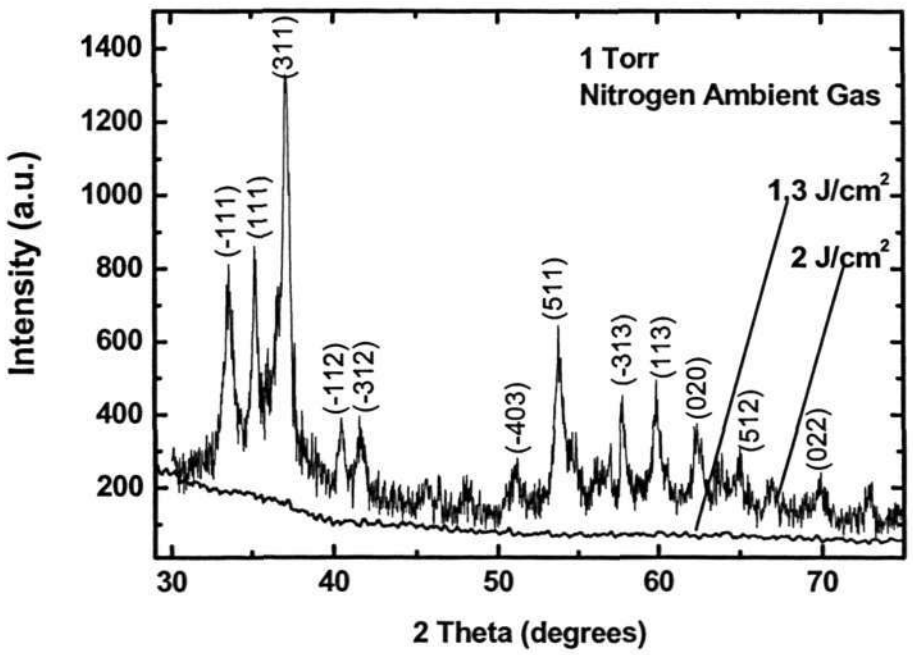

Figure 4-12 XRD patterns recorded on the as-deposited Ga_2O_3 nanoparticles at laser fluence of 1.3 J/cm^2 and 2 J/cm^2 at 1 Torr in N_2 ambient at room temperature.

4.4 Summary

In summary, a quick and novel synthesis method has been successfully used to synthesize monoclinic Ga_2O_3 nanoparticles and nanoclusters by pulsed laser ablation of a GaN target in N_2 or O_2 ambients, at room temperature. EDX and XPS confirm that the as-synthesized products are composed of only stoichiometric Ga_2O_3. The FESEM results clearly demonstrate that the diameter of the nanoparticles and degree of aggregation increase when deposited at higher growth pressures. TEM results revealed that the aggregation of the nanoparticles proceeded one dimensionally to

form chain-like nanostructures when synthesized at 10 to 100 Torr. TEM results also indicate that the spherical and ellipsoidal nanoparticles typically have diameters of 8.5 ± 1.75 nm and 6.5 ± 1.34 nm when synthesized at 10 Torr in N_2 and O_2 ambients, respectively. Also shown in XRD results, Ga_2O_3 nanoparticles with higher crystallinity were achieved when deposited at higher growth pressure. It is believed that an increase in the excited species in the laser plume at higher background gas pressure enhances the formation of the monoclinic phase of the Ga_2O_3. Ga_2O_3 nanoparticles deposited at higher laser fluence generated bigger nanoclusters and nanoparticles with higher crystallinity. In addition, the strong Raman peak at 416 cm^{-1} in bulk Ga_2O_3 powder redshifted for samples synthesized in an N_2 ambient. The observed redshift may be related to the creation of oxygen vacancies during the deposition process. On the other hand, the same mid-frequency Raman peak at 416 cm-^{1} in bulk Ga_2O_3 powder blueshifted to 421 cm^{-1} and 426 cm^{-1} for samples synthesized at 1 and 10 Torr in O_2 ambient respectively. The blueshift in phonon frequencies of low dimensional materials are often attributed to the quantum size-confinement effect. Based on these findings, it can be concluded that the size, shape, surface morphologies, degree of aggregation and crystallinity of the Ga_2O_3 nanoparticles and nanoclusters can be controlled accordingly by varying the growth conditions such as growth pressure, laser fluence and deposition gas.

CHAPTER 5

Optical Properties of Ga_2O_3 Nanoparticles

5.1 Introduction

Over the years, there has been a considerable interest in the novel optical properties of semiconductor nanoparticles and nanowires [170-174]. These nanostructures are interesting from a physical and chemical point of view mainly because several of their properties are very different from those of bulk materials [175]. In particular, they exhibit quantum confinement effects: the electron energy levels become discrete; the bandgap widens when their size is below a certain length scale characterized by the Bohr exciton radius. For example, Si in bulk is an indirect energy bandgap material. When its size is reduced below 5 nm, the non-radiative recombination rate reduces due to quantum confinement, enabling Si to emit visible luminescence at room temperature [176]. Similarly, cadmium sulfide has served as a prototype material in which both the absorption and emission shift to shorter wavelength for smaller crystal sizes [177]. This wide shift in fundamental properties is not achieved via variation of the chemical composition of the material; rather, it is decided through a reduction of the crystal size. Therefore by varying the crystal radius, the emission and excitation wavelengths of a nanocrystal can be tuned via quantum confinement effects. As the size of the nanocrystal is decreased, quantum confinement of the charge carriers also causes a blueshift of the absorption onset of up to 1 eV and the development of discrete features in the optical spectra.

Optical spectroscopy is a powerful tool in collecting information about the electronic structure and the fundamental properties of low dimensional materials. Optical measurements are very useful in the determination of the structure, defects

and impurities in these nanostructures. This chapter explores the use of photoluminescence and absorption spectroscopy to study the optical properties of the Ga_2O_3 nanoparticles and nanoclusters and investigate the quantum confinement effects which are known to influence the excitonic states of nanocrystalline semiconductors [178, 179].

5.2 Experimental

The synthesis method used to prepare Ga_2O_3 nanoparticles is similar to that described in Chapter 3. All steps of the synthesis were performed in N_2 or O_2 ambient at room temperature. The collected nanoparticles on Si substrates were characterized using room-temperature photoluminescence (PL), low-temperature PL and absorption spectroscopy. Room temperature PL spectra were obtained with a spectroflurophotometer (Shimadzu RF-5301PC) where the optical excitation was provided by a 150W Xenon arc lamp dispersed by a monochromator. The luminescence spectra were recorded by a secondary monochromator. The excitation light wavelength ranged from 266 to 325 nm. The emission light wavelength was detected in the range from 300 to 500 nm. No optical filters were used for collecting the room-temperature PL spectra. On the other hand, low-temperature PL spectra were obtained using a liquid helium flow-cryostat equipped system (JANIS ST-100) with a sample heater to stabilize the temperature between 10 K and room temperature. The optical excitation for low-temperature PL analysis was provided by a He-Cd laser (Kimmon, IK3023R-BR) at the wavelength of 325 nm. Lastly, the UV-vis spectra of Ga_2O_3 nanoparticles were obtained with UV-Vis-NIR scanning spectrophotometer (Shimadzu, UV-3101PC).

5.3 Results and Discussion

5.3. 1 Room-temperature Photoluminescence (PL) of Ga_2O_3 Nanoparticles

Figure 5-1 shows the PL spectra of bulk Ga_2O_3 nanoparticles synthesized at 10 Torr in N_2 and O_2 ambient Room temperature PL spectra were obtained with a spectroflurophotometer (Shimadzu RF-5301PC) where the optical excitation was provided by a 150W Xenon arc lamp The measurements were taken at room temperature with optical excitation at 266 nm. In general, the samples deposited at 10 Torr in N_2 and O_2 show broad emission bands ranging from 2.5 eV to 3.37 eV, with maximums at 3.17 eV and 3.19 eV respectively. A small blue emission peak located around 2.65 eV is also observed. Narrow and distinct UV peaks located around 3.41 - 3.44 eV are also observed. From the PL spectra, it is evident that Ga_2O_3 nanoparticles deposited in N_2 and O_2 exhibit both UV and blue emissions. For the PL mechanism of Ga_2O_3, several reports have suggested that the defect band emission of Ga_2O_3 crystals may be attributed to Ga vacancies (V_{Ga}), O vacancies (V_o) and Ga-O vacancy pair (V_o, V_{Ga}). Harwig and Kellendouk proposed that the blue luminescence of Ga_2O_3 originates from the recombination of an electron on a donor formed by V_o and a hole on an acceptor formed by V_{Ga} [180, 181]. Vasil'tasiv *et al.* suggested that the acceptor was formed by a (V_o, V_{Ga}) [182]. The V_o vacancies generally act as deep defect donors in the semiconductor, which would cause the formation of new donor levels in the bandgap. During photoexcitation, the electron in the donor V_o can be captured by the excited hole on an acceptor and a blue photon is emitted via radiative recombination process. On the other hand, the UV luminescence from Ga_2O_3 is independent of sample history, growth conditions and the impurity contents of the sample and has been attributed to an intrinsic transition, caused by self-trapped excitons [182].

It is observed that the UV emissions are relatively stronger than the blue emissions in all samples. It is therefore proposed that more electrons on the donors might be thermally detrapped to the conduction band, and more holes on acceptors might be thermally detrapped to form hole acceptors, recombining to emit a UV photon. In other words, more holes and electrons contribute to emitting a UV photon than a blue photon in the as-synthesized samples.

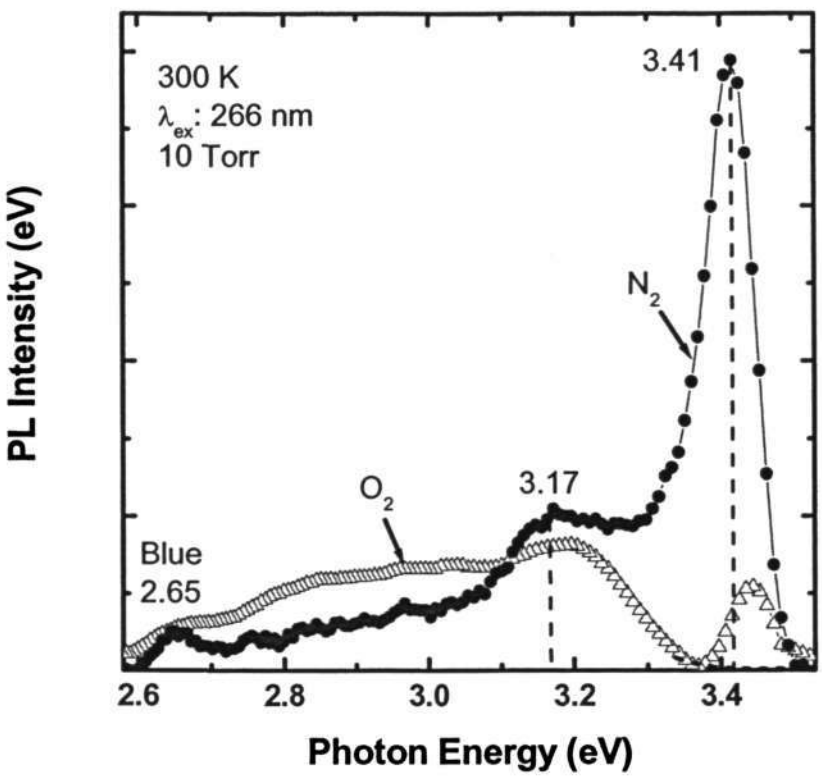

Figure 5-1 Room-temperature photoluminescence spectra of Ga_2O_3 nanoparticles and nanoclusters deposited at 10 Torr in N_2 and O_2 ambient.

The average diameters of Ga_2O_3 and nanoparticles deposited at 10 Torr in N_2 and O_2 are 8.5 ± 1.75 nm and 6.5 ± 1.34 nm, respectively. Clearly, the Ga_2O_3 nanoparticles deposited at 10 Torr in O_2 had smaller average diameters. The intensities of UV emission peaks located at 3.17 eV and 3.41 eV are found to be higher for samples synthesized in an N_2 ambient. This may be related to the fact that the surface-to-volume ratio becomes larger with decreasing size of the nanoparticles and smaller nanoparticles have larger non-radiative relaxation rates over the surface states. As a result, this non-radiative relaxation process occurring in the surface states will remarkably reduce the PL intensity with a smaller diameter of the nanoparticles. From the above discussions, it is considered that the stronger UV emissions of Ga_2O_3 nanoparticles deposited at 10 Torr in O_2 ambient could be due to a larger particle size that reduces non-radiative relaxation rates to enhance the UV emissions.

In general, nanoparticles with diameters smaller or equal to the Bohr exciton radius would exhibit a quantum confinement effect and a blueshift of the emission wavelength. Noticeably, the UV emission peaks located around 3.41 – 3.44 eV exhibit blueshifts of 5 meV (N_2) and 35 meV (O_2) with respect to Ga_2O_3 thin films (3.405 eV). Since the diameter of the as-synthesized Ga_2O_3 nanoparticles deposited in both N_2 and O_2 ambient are close to the Bohr exciton radius of Ga_2O_3 (2.6 nm - 5 nm), the blueshifts of the UV emission peaks are attributed to quantum confinement effects. In addition, a greater blueshift observed for O_2-syntheszied Ga_2O_3 nanoparticles is related to the smaller particle size that led to greater confinement effect. Binet *et al.* performed PL characterization on bulk Ga_2O_3 single crystal and found a peak at 2.85 eV [183]. The blue emission centered at 2.65 eV observed for Ga_2O_3 nanoparticles deposited in N_2 ambient indicates a blueshift of about 40 meV with the 2.61 eV reported by Zhang *et al.* for Ga_2O_3 powder [184]. Again, the blueshift of Ga_2O_3

nanoparticles can be ascribed to quantum confinement effect. Hence the luminescence mechanism may be attributed to quantum size effects and the presence of defects and surface states. In addition, the PL intensity is found to be strongly dependent on the growth conditions.

Yoffe *et al.* [185] have related the shift in energy to the average size of the particles for 3 different size regimes:

1) Weak confinement effects:

In this regime, the average size of the particle, R, is greater than the exciton radius, a_B, and the dominant term is the Coulomb term in the energy equation:

$$\hat{H}\psi(r_e, r_h) = \left[-\frac{\hbar^2}{2m_e}\nabla_e^2 - \frac{\hbar^2}{2m_h}\nabla_h^2 + V_e(r_e) + V_h(r_h) \right] \psi(r_e, r_h) \tag{5.1}$$

Due to size quantization of the excitons, the shift in energy ΔE is proportional to $1/R^2$ and is given by the equation:

$$\Delta E = \frac{\hbar^2 \pi^2}{2MR^2} \tag{5.2}$$

where

M = $m_e^* + m_h^*$ = mass of exciton

R = Average radius of the particle

2) Medium confinement effects:

For medium confinement effects, $R << a_e$ but $>> a_h$, where a_e and a_h are electron and hole Bohr radii respectively. In this size regime, the electron motion is quantized and the hole interacts with it through the Coulomb potential so the mass term in the above equation is substituted with the effective mass of the electron (m_e^*) and the shift in energy is given by

$$\Delta E = \frac{\hbar^2 \pi^2}{2 m_e^* R^2}. \tag{5.3}$$

3) Strong confinement effects:

In this case, the size of the particles is much smaller than both the Bohr electron radii and Bohr hole radii, and the electrons and holes can be considered as confined independent particles. Separate size quantization for the electrons and holes occur. Therefore, the shift in energy is still proportional to $1/R^2$, but the mass term is replaced by the reduced exciton mass and is given by

$$\frac{1}{\mu} = \frac{1}{m_e^*} + \frac{1}{m_h^*}. \tag{5.4}$$

The shift in energy is

$$\Delta E = \frac{\hbar^2 \pi^2}{2 \mu R^2}. \tag{5.5}$$

From the TEM studies, the average diameters of Ga_2O_3 nanoparticles synthesized at 10 Torr in N_2 and O_2 ambient are 8.5 nm and 6.5 nm respectively. The Bohr exciton diameter of Ga_2O_3 is not available in the literature. However, if the Bohr exciton diameter for Ga_2O_3 is close to that of indium tin oxide (ITO) which is in the range between 2.6 nm and 5 nm [186, 187] because the electronic structure is considered similar in both compounds [188]. We can expect the synthesized Ga_2O_3 nanoparticles to exhibit only weak confinement effects. Using equation 5.2, the size of the particles with an energy shift of 40 meV can be calculated.

$$\Delta E = \frac{\hbar^2 \pi^2}{2MR^2},$$

where

ΔE = shift in energy = 40 meV,

M = $m_e^* + m_h^*$ = $1.24m_0 + 0.44\ m_0$, and

R = radius of the particle.

Using the appropriate values in the equation, the average diameter of the particles was determined to be 6 nm. The calculated value is in good agreement with the TEM results for the average diameter of Ga_2O_3 nanoparticles synthesized at 10 Torr in O_2 (6.5 nm), thus indicating that the blue shift exhibits weak confinement.

5.3.2 Temperature Dependent Photoluminescence of Ga_2O_3 Nanoparticles

Figure 5-2 depicts the PL spectra for Ga_2O_3 nanoparticles measured at various temperatures (10 K - 200 K). The low-temperature PL spectra were obtained using a liquid helium flow-cryostat equipped system (JANIS ST-100) with a sample heater to stabilize the temperature between 10 K and room temperature and the optical excitation for low-temperature PL analysis was provided by a He-Cd laser (Kimmon, IK3023R-BR) at the wavelength of 325 nm. The reason for using another PL characterization system for this analysis is because the spectroflurophotometer (Shimadzu RF-5301PC) is not equipped with a low-temperature chamber for low-temp PL analysis. The Ga_2O_3 nanoparticles were deposited at 10 Torr in N_2 ambient. Narrow peaks at 2.79 eV (blue) with FWHM of approximately 34.2 meV, and broad emission bands in the region of 2.9 - 3.3 eV, which were centered at 3.13 eV (UV), were observed at temperatures from 10 to 200 K. When the temperature is gradually increased, the intensities of the UV emissions at 3.13 eV decrease and evident broadening of the peaks' linewidths are observed. Notably, the shift of the UV emission (3.13 eV) to lower energies with increasing temperature is also observed. The temperature dependence of the peak energy of I_D is shown in Fig. 5-3(a). The total shift between 10 K and 200 K is about 30 meV. The solid line in Fig 5-3(a) is fitted with the least-square method to Varshni's empirical formula [189] that describes the temperature dependence of the bandgap of a semiconductor and is given by:

$$E_g(T) = E_0 - \frac{\kappa T^2}{(\theta + T)} \quad (5.6)$$

In this equation, $E_g(T)$ is the energy at temperature T, E_0 is the energy at 0 K, and κ and θ are called Varshni's thermal coefficients. The least-square fit gives the value of $E(0)$ = 3.132 eV, κ = 0.96 meV/K and θ = 578 K for Ga_2O_3 nanoparticles. The obtained value for κ is in good agreement with the temperature dependence of the absorption edge of Ga_2O_3, which is approximately 1 meV [190]. The θ value of 578 K is in good agreement with the reported θ value of 570 K [191]. The linewidth broadening of the UV emission at 3.13 eV is depicted in Fig. 5-5(b). Due to electron-phonon coupling, the linewidth of the emission bands changes with temperature [192]. Similar linewidth broadening of the blue emission at 2.79 eV is also observed in Fig 5-4(b).

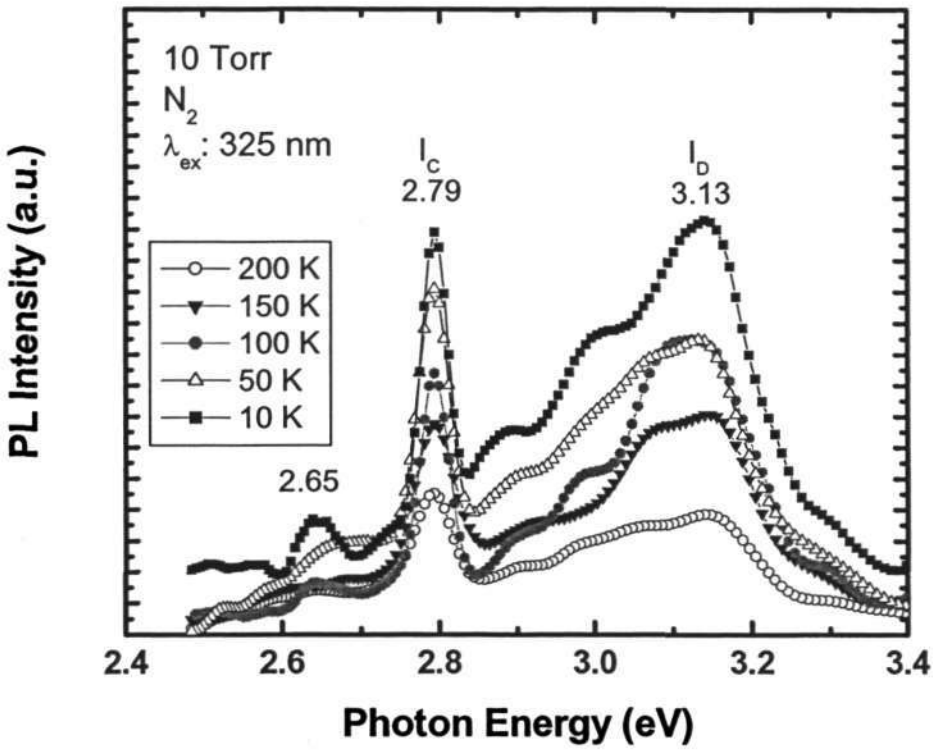

Figure 5-2 Photoluminescence spectra of Ga_2O_3 nanoparticles deposited at 10 Torr in N_2 ambient measured from 10 K to 200 K.

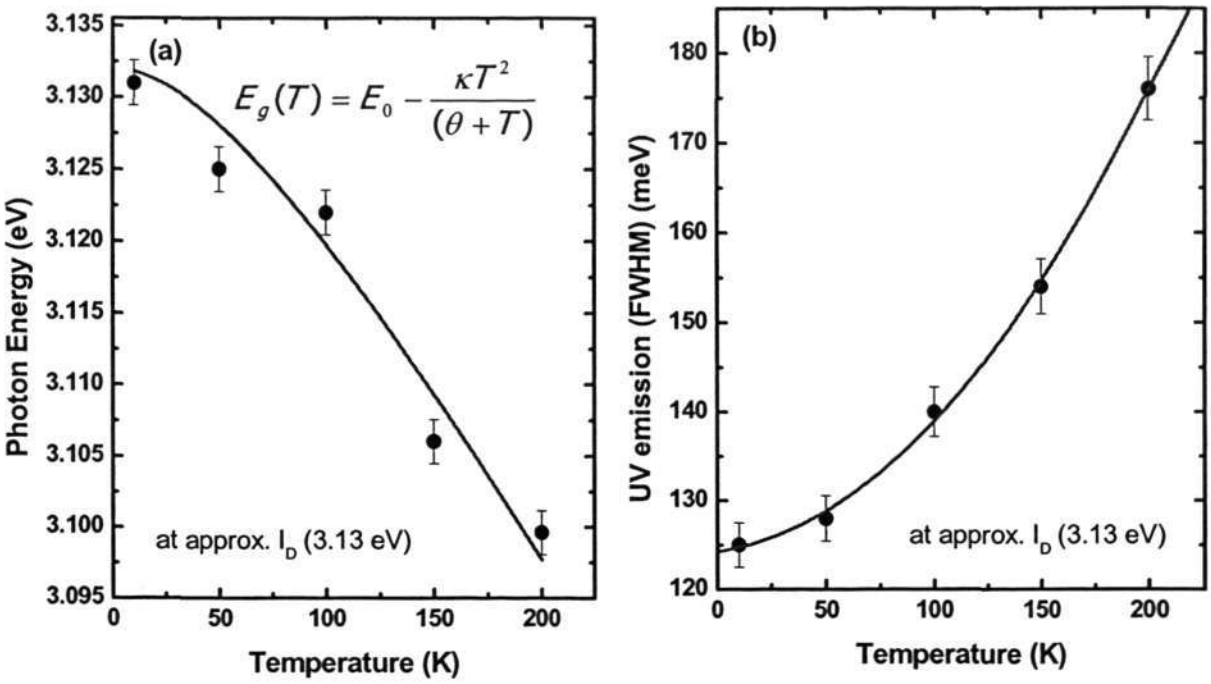

Figure 5-3(a) Temperature dependence of photon energy at I_D (3.13 eV) for Ga_2O_3 nanoparticles. Solid lines are least-square fitted to Varshni's empirical formula. (b) Full-width at half maximum of I_D as a function of temperature.

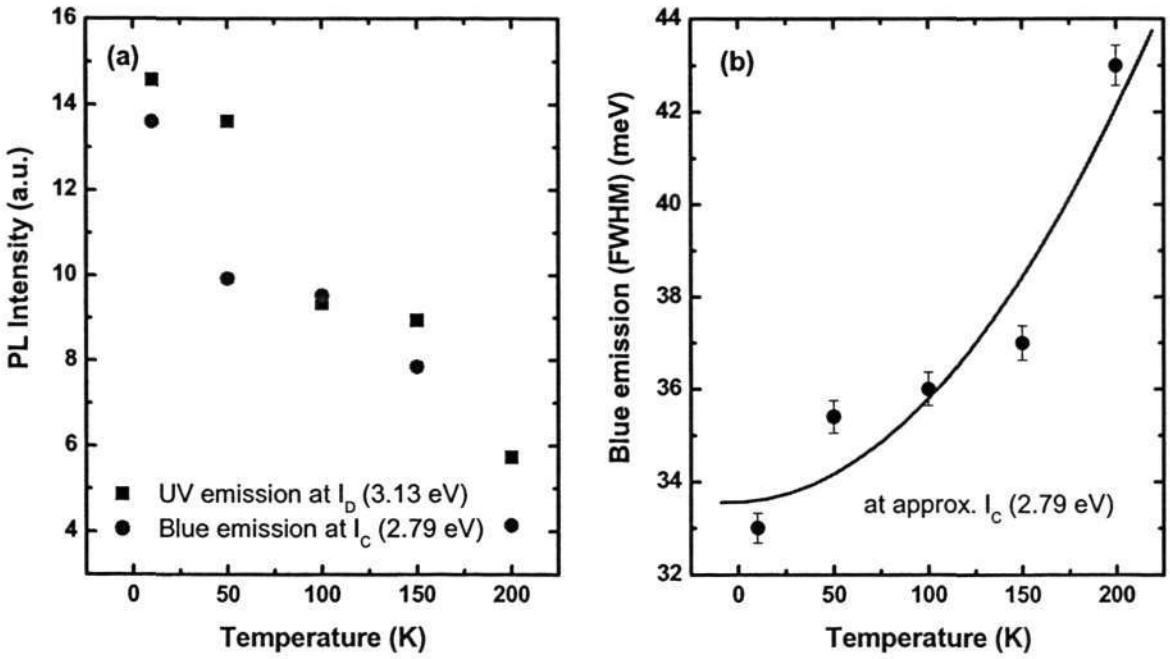

Figure 5-4(a) Temperature dependence of PL intensity at I_C and I_D for Ga_2O_3 nanoparticles. (b) Full-width at half maximum of I_c as a function of temperature.

Figure 5-4(a) presents the temperature dependence of the PL intensity of the UV and blue emissions. The intensities of the UV and blue emissions are found to decrease with increasing temperature. This is because as the temperature is increased, excitons dissociate and carriers vacate shallow traps thereby reducing the intensity of these features in the PL spectrum [193]. Thus low energy traps appear in low temperature PL because the thermal population of high- density band levels is very small. Figure 5-5 shows the temperature dependence of the integrated PL emission intensity at I_c of Ga_2O_3 nanoparticles.

To further study the thermal activation energy of I_c transitions, the integrated PL emission intensity has been fitted with the well-known expression [193]:

$$I(T) = \frac{I(0)}{1 + C_1 \exp\left(\frac{-E_1}{kT}\right) + C_2\left(\frac{-E_2}{kT}\right)}, \tag{5.7}$$

where C_1, C_2 and $I(0)$ are constants, k is Boltzmann's constant and E_1 and E_2 are the activation energies involved in the carrier recombination.

The fitting results are depicted in Fig. 5-5 and the parameters used for fitting are E_1 = 0.01 eV and E_2 = 0.51 for I_c. The reported activation energy of shallow donors due to oxygen vacancies is between 0.05 eV - 0.052 eV in Ga_2O_3 [183, 190]. Here, it is proposed that the activation energy E_2 are related to the activation energy of shallow donors due to oxygen vacancies in Ga_2O_3 while E_1 is due to other shallow donors. Orita *et al.* also reported that the thermal energy of the donor-bound electron for β-Ga_2O_3 thin films is approximately 0.01 eV, from the dependence of electrical conductivity on temperature [194].

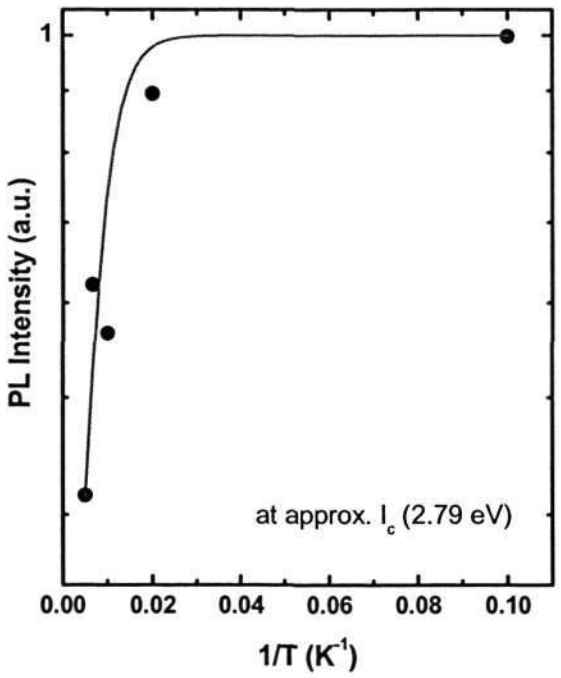

Figure 5-5 Temperature dependence of integrated PL emission intensity at I_C (2.79 eV) from Ga_2O_3 nanoparticles. Solid line is the least-squares fitting. The parameters used for fitting are $E_1 = 0.01$ eV and $E_2 = 0.051$ eV for I_c.

Therefore, it is evident that the E_1 and E_2 values obtained from the fitting are in good agreement with the reported values and it can be concluded that E_1 corresponds to the activation energy of the shallow donor due to oxygen vacancies below the conduction band. Furthermore, the results highlight that the electrons trapped on the donor are involved in both blue and UV luminescence recombination.

5.3.4 UV-Vis Absorption of Ga_2O_3 Nanoparticles

Figure 5-6 shows the optical absorption spectra for Ga_2O_3 nanoparticles deposited at 10 Torr in both N_2 and O_2 ambients. Although an isolated absorption peak is not observed in Fig. 5-6, the N_2- and O_2-synthesized Ga_2O_3 nanoparticles exhibit absorption edges around 238.5 nm and 232 nm, respectively. Xu *et al.* has similarly reported a strong absorption feature (~ 258 nm) for Ga_2O_3 nanowires in the UV region without the appearance of an isolated absorption peak [195]. The bandgap of bulk Ga_2O_3 occurs at 258 nm [196]. Hence, significant blueshifts of the absorption edge are observed for the Ga_2O_3 deposited in both N_2 and O_2 ambient is clearly observed. A shift of the absorption edge towards a higher energy is generally expected from nanocrystalline materials due to quantum size effects. The large blueshift in the absorption shoulder is attributed to the strong confinement effects in small particles. Clearly, there is more significant blueshift of the absorption shoulder for nanoparticles synthesized in O_2 ambient. This may be related to the smaller size-distribution of Ga_2O_3 nanoparticles synthesized in O_2 ambient. This result is also consistent with the PL results reported in the earlier section.

When a semiconductor material absorbs a photon with high enough energy, an electron is excited from the valence band to the conduction band. The onset of this absorption occurs at the bandgap energy, E_g, which for bulk Ga_2O_3 is 4.8 eV at room temperature (300 K). For Ga_2O_3 nanoparticles, the electron levels become discrete due to quantum confinement effects and the bandgap, E_g increases with decreasing particle size. The bandgap energy can be calculated from the absorption coefficients in the onset region using the relation [197]:

$$(\alpha h\nu)^n = B(h\nu - E_g), \tag{5.9}$$

where α is the absorption coefficient, hν the energy of the incident photon, B the absorption edge width parameter, E_g the optical bandgap and n the exponent. It has been well established that the exponent determines the type of electronic transitions causing the optical absorption and can take values $1/2$, $3/2$, 2 and 3 for direct-allowed, direct-forbidden, indirect-allowed, and indirect-forbidden transitions, respectively. It has been shown that Ga_2O_3 single crystals have a direct energy band structure with anisotropic optical properties [198]. For Ga_2O_3 nanoparticles, E_g can be obtained by extrapolating the plot of $(\alpha h\nu)^2$ vs. hν to $\alpha = 0$. The estimations of the optical bandgap were found to be 5.5 and 5.7 eV (insets of Fig. 5-6a and b) for nanoparticles deposited at 10 Torr in N_2 and O_2 ambient, respectively. Similarly, the bandgap widening (blueshift in the absorption edge) of the Ga_2O_3 nanoparticles can be explained by quantum confinement size effects. Recently, Allan *et al.* also reported a blue shift in the absorption edge for amorphous silicon nanoclusters, where the bandgap shifts to higher energy with reduction in size [199].

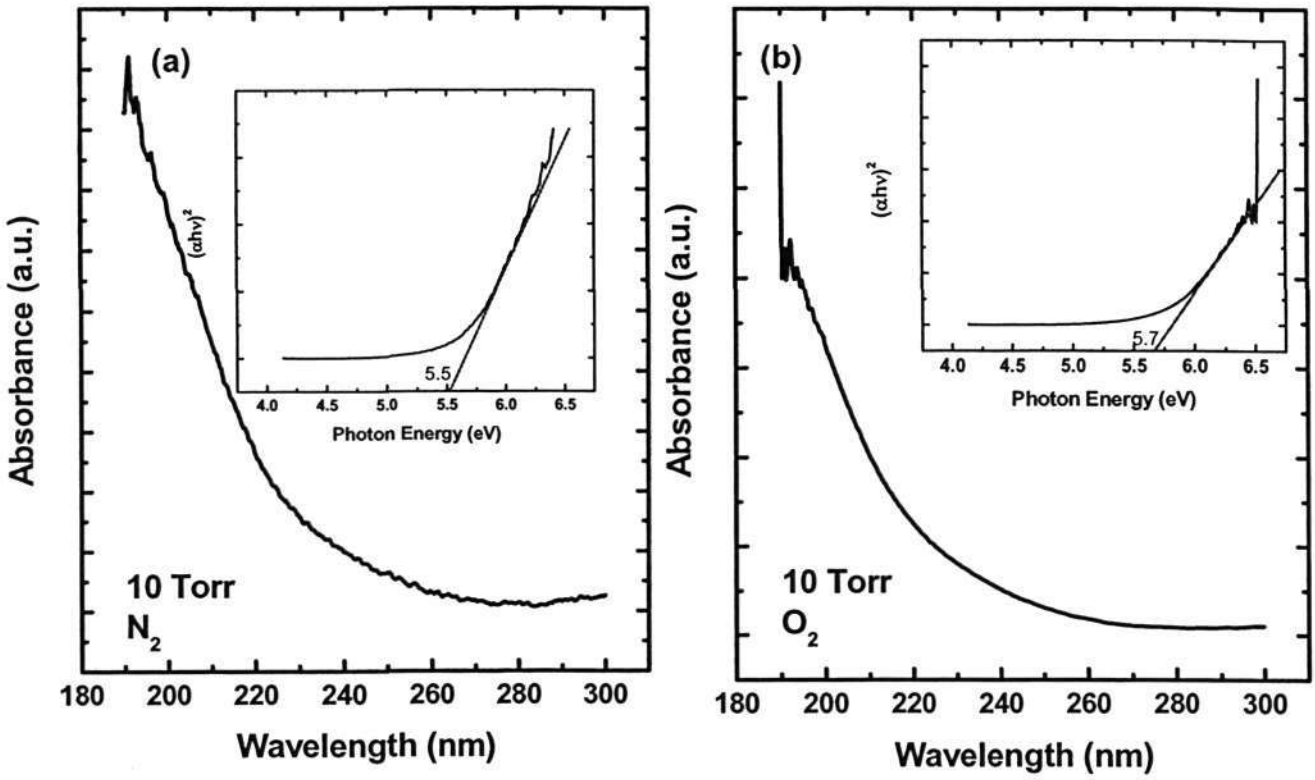

Figure 5-6 Optical absorption spectra for Ga_2O_3 nanoclusters and nanoparticles deposited at 10 Torr in N_2 and O_2 ambient

5.4. Summary

The optical properties of Ga_2O_3 nanoparticles synthesized via pulsed laser ablation of GaN at room temperature were investigated. Ga_2O_3 nanoparticles deposited at 10 Torr in both N_2 and O_2 ambient exhibit both UV and blue emissions. Ga_2O_3 nanoparticles exhibited a blueshift of the blue emission located at 2.65 eV, as compared to the feature PL emission of bulk Ga_2O_3 powders. The PL blueshift is attributed to quantum confinement effects. Furthermore, upon some mathematical calculation, the PL blueshift of Ga_2O_3 nanoparticles is also found to possess weak confinement. In addition, the temperature dependence of the peak position and linewidth for both blue and UV emission bands of Ga_2O_3 nanoclusters and nanoparticles have been studied. The temperature-induced linewidth broadening and

shift to longer wavelength were observed for the blue and UV emission bands. Due to electron-phonon coupling, the linewidth of the emission bands increases with higher temperature. Both UV and blue emission intensities also decrease with increasing temperature and that is related to the elimination of shallow traps. Lastly, the effect of deposition gas on the absorption of Ga_2O_3 nanoparticles was also investigated. Significant blueshift of the absorption edge was clearly observed for Ga_2O_3 nanoparticles formed in both N_2 and O_2 ambient. It is proposed that the blueshift in the absorption edge is also related to strong quantum confinement effects.

CHAPTER 6

Effect of KrF Excimer Laser Annealing on the Crystallinity and Photoluminescence of Ga_2O_3 Nanoparticles and Nanoclusters

6.1 Introduction

Laser annealing of semiconductor materials was first demonstrated by Japanese scientists in 1979 [200]. Due to the many advantages of laser annealing, there has been extensive study and development in the laser annealing of various semiconductor materials such as Si [201] and ZnO [202] in the past decades. The dominant characteristic of laser annealing features large energy absorption in a short time interval. Typically, the surface of the absorbing material is heated up in milliseconds, nanoseconds or even in picoseconds, depending on the types of laser employed. In pulsed UV laser annealing, only the thin surface layer of about a few hundred to several thousand angstroms can be heated to a very high temperature, without concomitant annealing of the underlying substrate. This allows rapid recrystallization of the melted layer to occur, thereby offering a higher temporal and spatial control over the annealing process as compared to conventional furnace annealing. The advantages of pulsed laser annealing over standard furnace annealing include short processing cycles that can be achieved with an UV excimer laser [203], selected area processing of an implanted sample [204], rapid crystallization without any change in the intrinsic structure [205], and avoidance of surface contamination which are important aspects of laser applications to materials processing. Laser-annealed materials also show good crystallinity which is related to laser-induced melting and regrowth of the material. In particular, laser induced Si melting, crystallization and amorphization has been widely employed to achieve high mobility

thin film transistors for liquid crystal displays [206]. The ultrafast melting and resolidification sequence by pulsed laser annealing has been extensively studied with various time-resolved optical [207], electrical [208] and X-ray [209] techniques. In addition, an improvement in the structural and optical properties of polycrystalline GaN on silica substrates by excimer laser annealing has been recently demonstrated by Kim *et al.* [210]. Conventional thermal annealing requires the samples to be heated to high temperature for sufficiently long time for thermal diffusion of the defects to occur. However, the heating of the entire sample has undesirable effects for device production. The use of a pulsed laser is more advantageous for annealing because laser annealing is local and very rapid. In this study, pulsed laser ablation was used to fabricate Ga_2O_3 nanoparticles in N_2 ambient. Pulsed KrF excimer laser annealing was applied to the as-deposited Ga_2O_3 nanoparticle film. The purpose of this work is to improve the crystallinity and photoluminescence of the amorphous Ga_2O_3 nanoparticles and nanoclusters.

6.2 Experimental

Ga_2O_3 nanoparticles were deposited by pulsed laser ablation of GaN in purified N_2 (99.995%) gas. A pulsed KrF excimer laser (Lambda Physik, Compex 102, λ = 248 nm, τ = 30 ns) was used to ablate the GaN target as shown previously in Fig. 3-1. The target was rotated constantly to ensure uniform ablation of the target surface. After the base vacuum of the deposition chamber was pumped down to 5.0 X 10^{-3} Pa, N_2 was slowly introduced into the vacuum chamber and maintained at a constant pressure of 10 Torr during deposition. The deposition was carried out for 20 min at the laser fluence of 1.3 J/cm^2 at room temperature and the Ga_2O_3 nanoparticles deposited on cleaned Si and quartz substrates were laser annealed by KrF excimer (Lambda Physik,

Compex 102) laser at room temperature in air. The laser fluence used for annealing is much smaller than that required for deposition. KrF excimer laser annealing was performed at various laser fluences (30 to 150 mJ/cm^2) and with laser pulses with a repetition rate of 1 Hz. In order to obtain a homogeneous laser fluence over a relatively wide area, the laser beam was condensed by a lens (f = 50 mm) on a square (0.5 x 0.5 cm) stainless steel mask. The effective area for annealing is 0.25 cm^2. The mask was placed above the sample surface, with a gap of 1 cm between them. Surface morphology, crystallinity and photoluminescence (PL) of the laser annealed Ga_2O_3 samples were characterized by several methods. The surface morphology of the laser annealed samples was observed using a field emission scanning electron microscope (FESEM, Joel JSM 6340F). XRD analysis was performed by using CuKα radiation (λ = 1.5404 Å) and a X-ray diffractometer (Shimadzu 6000). Room-temperature PL spectra were recorded using a fluorescence spectroflurophotometer (Shimadzu RF 5301PC).

6.3 Results and Discussion

6.3.1 Surface Morphology and Crystallinity of Ga_2O_3 Nanomaterials after Laser Annealing

Ga_2O_3 nanoparticles were deposited on cleaned Si and quartz substrates at room temperature under optimized conditions (laser fluence = 1.3 J/cm^2 and deposition pressure = 10 Torr) in an N_2 ambient for 15 minutes. The as-deposited nanoparticles were laser annealed by using a pulsed KrF excimer laser beam at different laser fluences. The surface morphology of the Ga_2O_3 nanoparticles annealed at different laser fluences was investigated using a FESEM. Figure 6-1(a) shows a typical FESEM image of the as-prepared nanoparticles on the surface of the Si substrate. It

reveals a porous, chain-like structure made up of nanoparticle aggregates. Figure 6-1(b) to (g) presents the FESEM images of the Ga_2O_3 samples after pulsed KrF excimer laser annealing at the laser fluence of 30 mJ/cm^2, 50 mJ/cm^2, 80 mJ/cm^2, 100 mJ/cm^2,120mJ/cm^2 and 150 mJ/cm^2, respectively.

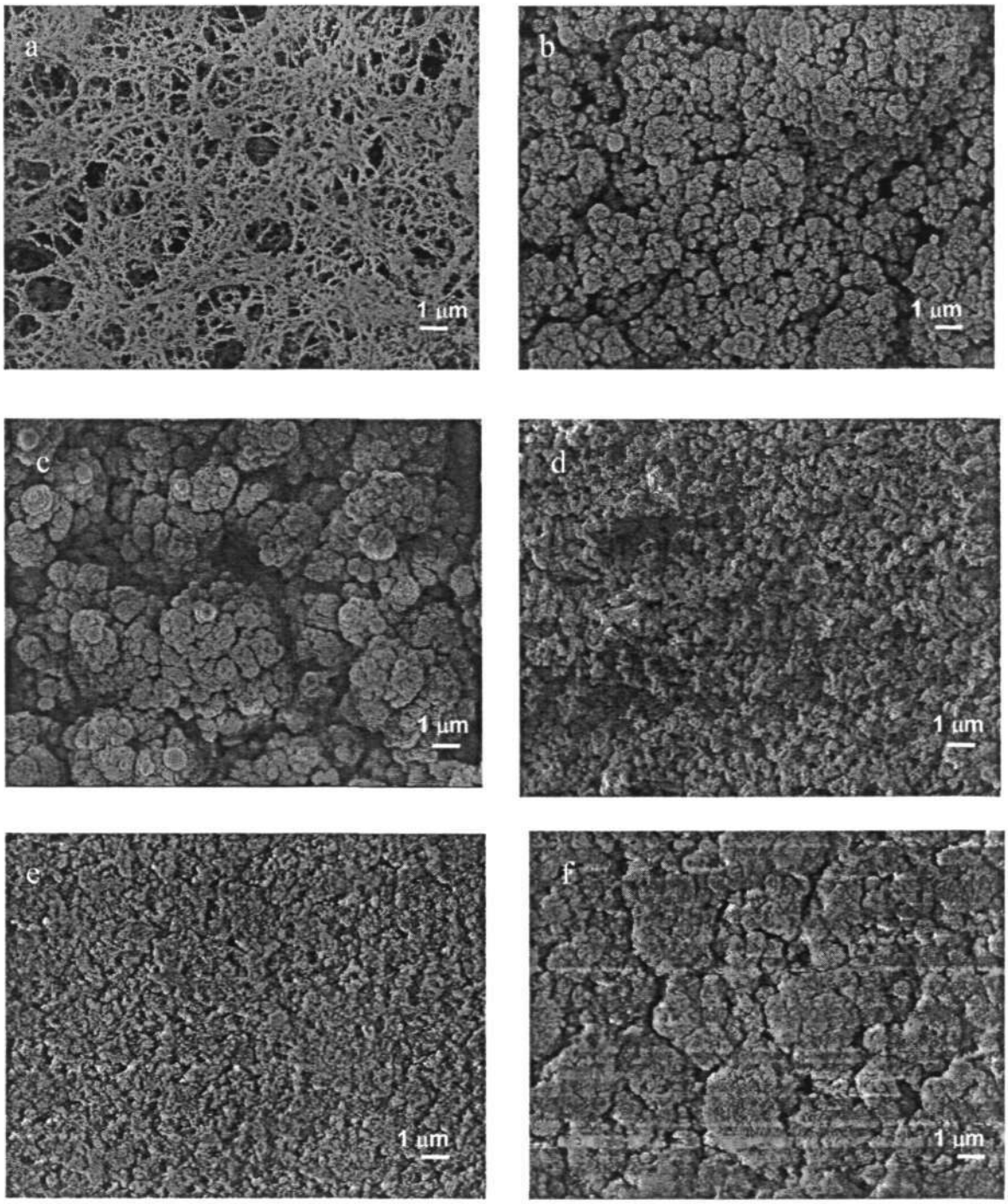

Fig. 6-1 FESEM images of KrF excimer laser annealed Ga_2O_3 nanoparticles at (a) as-deposited, (b) 30 mJ/cm^2, (c) 50 mJ/cm^2, (d) 80 mJ/cm^2, (e) 100 mJ/cm^2 and (f) 120 mJ/cm^2. The scale bar is 1 μm.

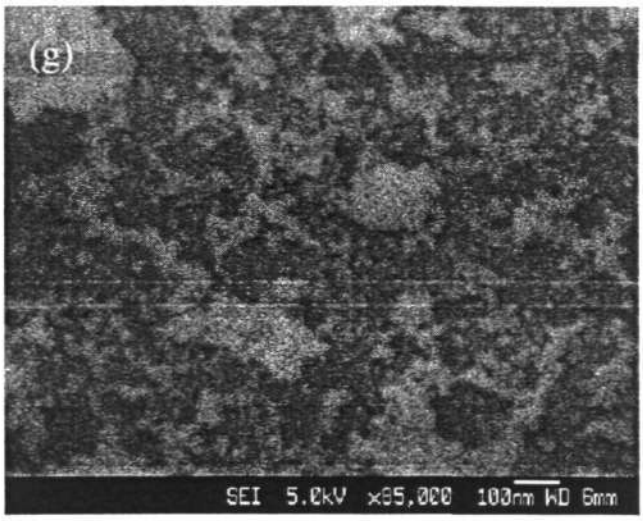

Fig. 6-1(g) FESEM images of KrF excimer laser annealed Ga_2O_3 nanoparticles at 150 mJ/cm^2.

Clearly, the chain-like nanoparticle aggregates transformed to nanoball-like morphology with diameters of 200 nm and 500 nm when laser annealed at the laser fluence of 30 mJ/cm^2 and 50 mJ/cm^2, respectively. Further morphology transformations were observed with even higher laser fluences. The nanoball-like structure started to coalesce, forming larger grains due to interparticle diffusion when annealed at a laser fluence ≥ 80 mJ/cm^2. Furthermore, the grain distribution became denser and formed a film-like structure when laser annealed at 120 mJ/cm^2. At a laser fluence between 80 – 120 mJ/cm^2, regrowth of small Ga_2O_3 grains seems to occur under the melting condition caused by KrF laser irradiation. Similar melting behaviour has also been observed in pulsed laser deposited ZnO films upon laser annealing at 193 nm [202]. However, after annealing with a laser fluence of 150 mJ/cm^2, laser ablation of the Ga_2O_3 nanoparticles was observed with significant removal of the as-deposited material from the substrate surface (see Fig. 6-1g). Hence, it is proposed that the remaining nanoclusters on the substrate might be damaged from the impinging laser pulse.

As discussed earlier, it is evident that a pulsed KrF excimer laser (laser fluence ≥ 80 mJ/cm^2) causes surface melting of the laser annealed samples whereby the surface of the absorbing material is heated to its melting temperature in nanoseconds or even picoseconds in pulsed laser annealing. The temperature rise induced by the absorbed laser radiation on a material surface or within its bulk can be calculated. Since the laser intensity profile is almost homogeneous, the one-dimensional heat diffusion equation is employed to find the sample temperature due to laser irradiation and is given by [210]:

$$\frac{\partial T}{\partial t} = \frac{\alpha}{\rho C_p} I(z,t) + \frac{1}{\rho C_p} \frac{\partial}{\partial z}\left(\kappa \frac{\partial T}{\partial z}\right), \tag{6.1}$$

where T is the temperature, $I(z,t)$ is the intensity of the laser light at depth z and time t for a homogeneous material and ρ, C_p, κ, R and α are the density, specific heat, thermal conductivity, reflectivity and absorption coefficient of the material respectively.

The light absorption length is

$$l = \alpha^{-1} \tag{6.2}$$

and the heat diffusion length is

$$l_\tau \approx 2\sqrt{D\tau} \ , \tag{6.3}$$

where D is the thermal diffusivity of the material and τ is the laser pulse duration. When the light absorption length is much smaller as compared with the heat diffusion length, equation 6.1 can be solved as [211]:

$$T(z,t) = \frac{2I_0}{\kappa}\sqrt{Dt}\left(\frac{z}{2\sqrt{Dt}}\right)(1-R). \qquad (6.4)$$

For Ga_2O_3, data on the temperature dependence of the parameters involved is limited, so it is very difficult to perform any accurate calculation on the temperature profile, heating and cooling rates in Ga_2O_3 for a certain laser intensity or fluence. However, from equation 6.4, it can be concluded that there exists a linear relationship between laser intensity and surface temperature.

In order to investigate the effect of laser annealing on the crystallinity of Ga_2O_3 nanoparticles, XRD analysis on the as-deposited and laser annealed samples were performed. Figure 6-2 represents the wide-angle XRD spectra of the laser annealed Ga_2O_3 samples. As shown previously in Fig. 4-7, the as-deposited nanoparticles synthesized at a laser fluence of 1.3 J/cm^2 in N_2 at 10 Torr are primarily amorphous, due to the absence of a distinguishable Ga_2O_3 diffraction peak. Only after laser annealing performed at 120 mJ/cm^2 (Fig. 6-3), are distinct diffraction peaks observed and found to coincide with (311), $(\bar{1}12)$ and (512) peaks of β-Ga_2O_3 (JCPDS card no. 41-1103). In other words, Ga_2O_3 nanoparticles remained amorphous when annealed at between 30 – 100 mJ/cm^2 where no apparent diffraction peaks were detected below 120 mJ/cm^2. The wavelength of the KrF excimer laser is in the UV region, thus its laser energy is absorbed effectively by the surface of the Ga_2O_3 samples. Therefore, as the laser fluence increases, the absorption depth also increases and the thickness of

modified surface layer increases. Thus, more crystallinity was observed. From these results, it can be deduced that crystallinity of the Ga_2O_3 nanoparticles can be improved by carrying out laser annealing at a laser fluence of 120 mJ/cm^2. However, when the laser fluence was further increased to 150 mJ/cm^2, the previously observed diffraction peaks at (311), $(\bar{1}12)$ and (512) are no longer apparent and the intensity of XRD spectrum has decreased significantly, thereby indicating a loss in crystallinity. This observation has confirmed our earlier deduction that the as-deposited Ga_2O_3 nanoparticles were damaged after a laser fluence of 150 mJ/cm^2 was employed for laser annealing of the samples. Now, it is apparent that laser annealing at high fluence values, in the range of 150 mJ/cm^2 led to a laser ablation effect as well as material damage, while in the range of 30 to 100 mJ/cm^2, the photon flux was not sufficient for to achieve good crystallinity of the Ga_2O_3.

The average grain size L of the laser annealed Ga_2O_3 samples can be estimated by Scherrer's equation [212],

$$L = \frac{0.9\lambda}{D\cos\theta} \tag{6.5}$$

where λ is the wavelength of the X-ray, D is the FWHM of the (311) diffraction peak and θ is the Bragg angle. From equation 6.5, the grain size was found to be 25 nm for samples laser annealed at 120 mJ/cm^2. Prior to laser annealing, the size of the nanoparticles deposited in N_2 at 10 Torr was 8 ± 1.75 nm (see Table 4-1). Clearly, the grain size increased with increasing laser fluence employed for laser annealing. This result further suggests the coalescence of Ga_2O_3 grains toward lateral directions to form a film-like morphology.

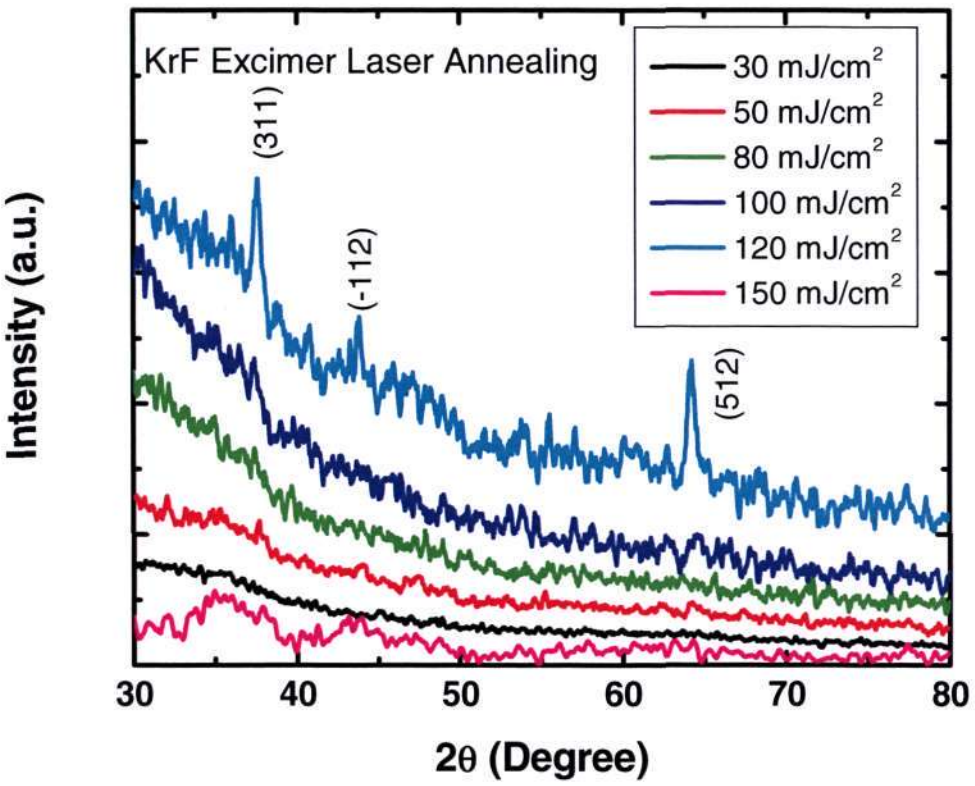

Figure 6-2 XRD spectra recorded from the Ga_2O_3 nanoparticles after KrF excimer laser (laser fluence = 30 mJ/cm^2 to 150 mJ/cm^2) annealing.

6.3.2 Photoluminescence of Ga_2O_3 Nanomaterials after Laser Annealing

Figure 6-3 depicts the room-temperature PL spectra of the KrF excimer laser-annealed Ga_2O_3 samples at various laser fluences. As discussed previously, the blue emission around 2.66 eV is related to the recombination of an electron on a donor formed by oxygen vacancies and a hole on an acceptor formed by gallium vacancies or gallium-oxygen vacancy pairs [213, 214], while the UV emission at 3.41 eV is due to the recombination of holes and electrons via a self-trapped exciton [215]. Notably, the PL intensity of the blue and UV emissions increases linearly with increasing laser fluences in the KrF excimer laser-annealed samples. This may be explained by the fact that the surface-to-volume ratio becomes larger with decreasing size of the microcrystals and smaller grains have larger non-radiative relaxation rates over the surface states. As a result, this non-radiative relaxation process occurring in the surface states will remarkably reduce the PL intensity with a smaller crystal dimension. From the above discussions, it is considered that the stronger blue and UV emission in the PL spectra for samples annealed at higher laser fluence could be due to a larger grain size that reduces non-radiative relaxation rates to enhance the PL emissions. It is also known that the efficiency of light absorption by nanoparticles or nanoclusters increases with particle size [216]. Thus, the larger clusters absorb more photons and more electron-hole pairs are created to increase the PL intensity.

Evidently, the UV emission is relatively stronger than the blue emission in the KrF excimer laser-annealed samples. When Ga_2O_3 samples were laser annealed at high laser fluence, the surface temperature also increased linearly (see equation 6.4), thus it is surmised that more electrons on the donors might be thermally detrapped to the conduction band, and more holes on acceptors might be thermally detrapped to form hole acceptors, recombining to emit a UV photon. Therefore, it is deduced that more

holes and electrons contribute to emitting a UV photon than a blue photon after KrF excimer laser annealing.

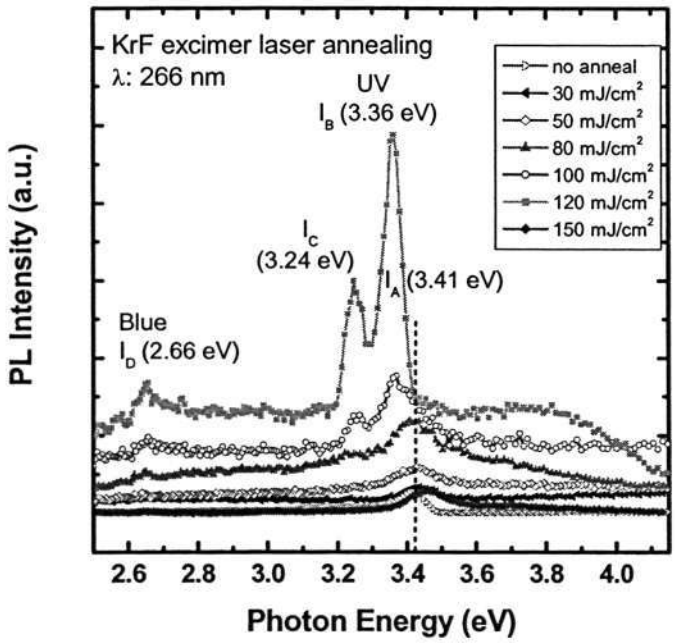

Figure 6-3 PL spectra recorded from the Ga_2O_3 nanoparticles after KrF excimer laser (laser fluence = 30 mJ/cm^2 to 150 mJ/cm^2) annealing.

Similarly, it can be inferred from both the XRD and PL spectrum that an improvement in crystallinity of the laser annealed samples correspondingly increases the PL intensity of blue and UV emissions. This correlation is clearly observed for Ga_2O_3 samples annealed at 120 mJ/cm^2. However, it is found that the PL intensity decreased significantly for samples laser annealed at 150 mJ/cm^2. The decrease in PL intensity may be related to the material damage and loss in crystallinity of the samples when laser annealed at high laser fluence. Hence, it can be deduced that PL emission of the Ga_2O_3 samples is dependent on the amount of crystalline phase present in the material.

In Fig. 6-3, the dominant UV emission of the as-deposited Ga_2O_3 nanoparticles is located around 3.41 eV (I_A) and the reported UV emission for Ga_2O_3 thin film is 3.405 eV [217]. Hence, a blueshift of approximately 5 meV was observed for the as-deposited Ga_2O_3 nanoparticles as compared to Ga_2O_3 thin films. The blueshift of the as-deposited Ga_2O_3 nanoparticles is attributed to quantum-size effects. Table 6-1 highlights the peak position and peak shift of the UV emission for Ga_2O_3 samples annealed at various laser fluences. As the material is damaged at 150 mJ/cm^2, these samples were not included in the later studies.

Table 6-1 PL peak position and peak shift as a function of laser fluence for laser annealing.

Laser fluence (mJ/cm^2)	Thin Film	As-deposited	30	50	80	100	120
PL peak position (eV)	3.405	3.410	3.436	3.431	3.419	3.361	3.359
PL peak shift (meV)		5	31	26	14	44	46
		← Blueshift →				← Redshift →	

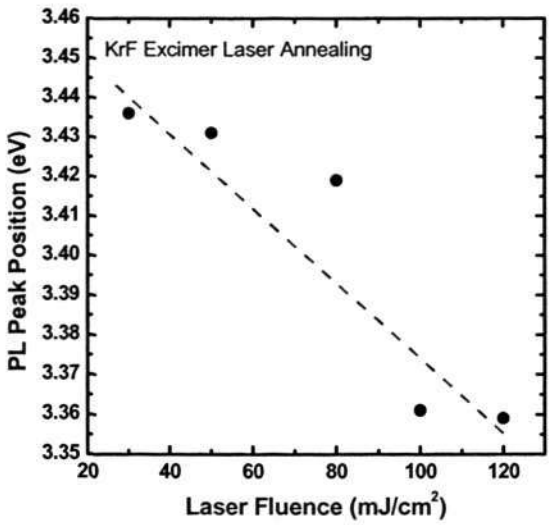

Figure 6-4 PL energy as a function of the laser fluence for KrF excimer laser annealing.

When laser annealed at 30 mJ/cm^2, 50 mJ/cm^2 and 80 mJ/cm^2, the Ga_2O_3 samples exhibit a blueshift of 31 meV, 26 meV and 14 meV respectively, as compared to bulk Ga_2O_3 thin films. However, the extent of blueshift decreases with increasing laser fluence and this is related to the increasing grain size of the laser annealed samples at higher laser fluence. The blueshift is not likely to be attributed to quantum confinement effect, as the size of the laser annealed samples is much larger than the Bohr exciton radius of Ga_2O_3 which is in the range from 2.5 to 5 nm. Hence, it would be more plausible that these changes come about due to the dispersive nature of the peaks in Ga_2O_3 due to crystallinity, internal stresses and even the intensity of the excitation source [218]. Upon further increase of the laser fluence to 100 mJ/cm^2 and 120 mJ/cm^2, a PL redshift of up to 46 meV is observed. Additional PL emission peaks at I_C (3.24 eV), I_D (2.66 eV) and a broad emission band ranging from 3.3 eV to 4.2 eV and are observed for samples laser annealed at 120 mJ/cm^2. The splitting of the emission band in the UV region might be associated with the relatively complex crystal structure of Ga_2O_3, which contains two crystallographic sites for gallium and three for oxygen.

It is hypothesized that laser annealing and heat trapping take place in the ensemble of Ga_2O_3 and would result in the thermal shift of the PL into lower emission energies. A similar redshift of the photoluminescence of the ensembles of GaN microcrystals due to UV laser heating was also reported by Bergman *et al.* [219]. In general, the temperature dependence of the PL energy in semiconductors can be approximated via the relation [220]:

$$E(T) = E(0) - \frac{2\alpha}{\exp(a/T) - 1} \quad . \tag{6.6}$$

This relationship represents the modification of a bandgap of a semiconductor due to electron-phonon interaction. In Equation (6.6), α is a measure of the strength of the interaction, and $a = E_p/k_B$, where E_p is the average phonon energy. From equation 6-6, it is deduced that at elevated temperature and high laser fluence, the PL energy shifts towards larger wavelengths or lower energies. Figure 6-5 presents linewidth broadening for I_A with increasing laser fluence after KrF excimer laser annealing. Emission broadening reveals a broad size distribution of nanoparticles or nanoclusters [221].

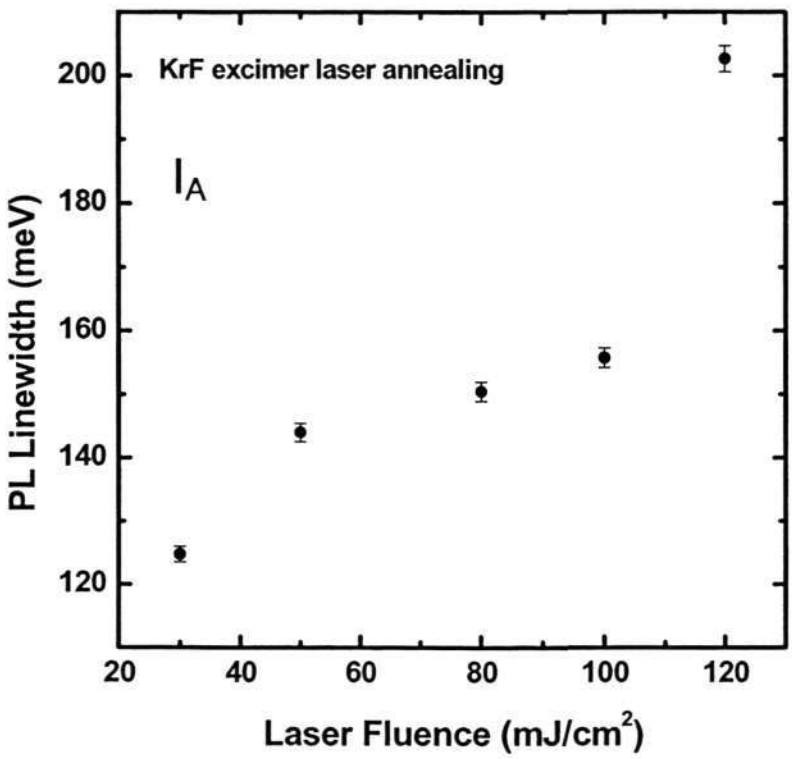

Figure 6-5 PL linewidth as a function of laser fluence for KrF excimer laser annealing.

Figure 6-6 shows the influence of multiple-pulse KrF laser annealing on the PL emission of Ga_2O_3 nanoparticles. After laser annealing at the laser fluence of 30 mJ/cm^2 and 50 mJ/cm^2, the PL intensities of the Ga_2O_3 samples are greatly enhanced with increasing pulse number from 1 to 5 but decreases with higher pulse number (see Fig 6.7). With increasing pulse number, there is also a greater PL redshift from 3.405 eV (thin film) to 3.35 eV (5 pulse), additional peaks at 3.24 eV and 2.66 eV are also clearly seen when 5 laser pulses were irradiated on the Ga_2O_3 samples at 30 mJ/cm^2. During the multiple shots, the increase in blue emission (2.66 eV) is because of the creation of oxygen vacancies. In Fig. 6-6(a), a broadband emission band ranging from 2.6 eV to 3.3 eV was observed when 3 laser pulses were employed. As discussed earlier, the complex crystal structure of Ga_2O_3 may have caused the splitting of the UV emission bands after laser 5 pulses was applied to the samples at 30 mJ/cm^2 and 50 mJ/cm^2. However, when more than 5 laser pulses are employed at laser fluence of 30 mJ/cm^2 and 50 mJ/cm^2, it resulted in laser ablation effects thereby resulting in a reduction in PL intensity (see Fig. 6-7). At the same time, absorptivity increases within the irradiated volume with increasing laser pulses. With an increase in energy absorption, it will result in a drop in threshold fluence and laser ablation of the material proceeds after a certain number of laser pulses which will cause material damage. Therefore, to achieve the best annealing effect, the number of laser pulses should be controlled before laser ablation begins.

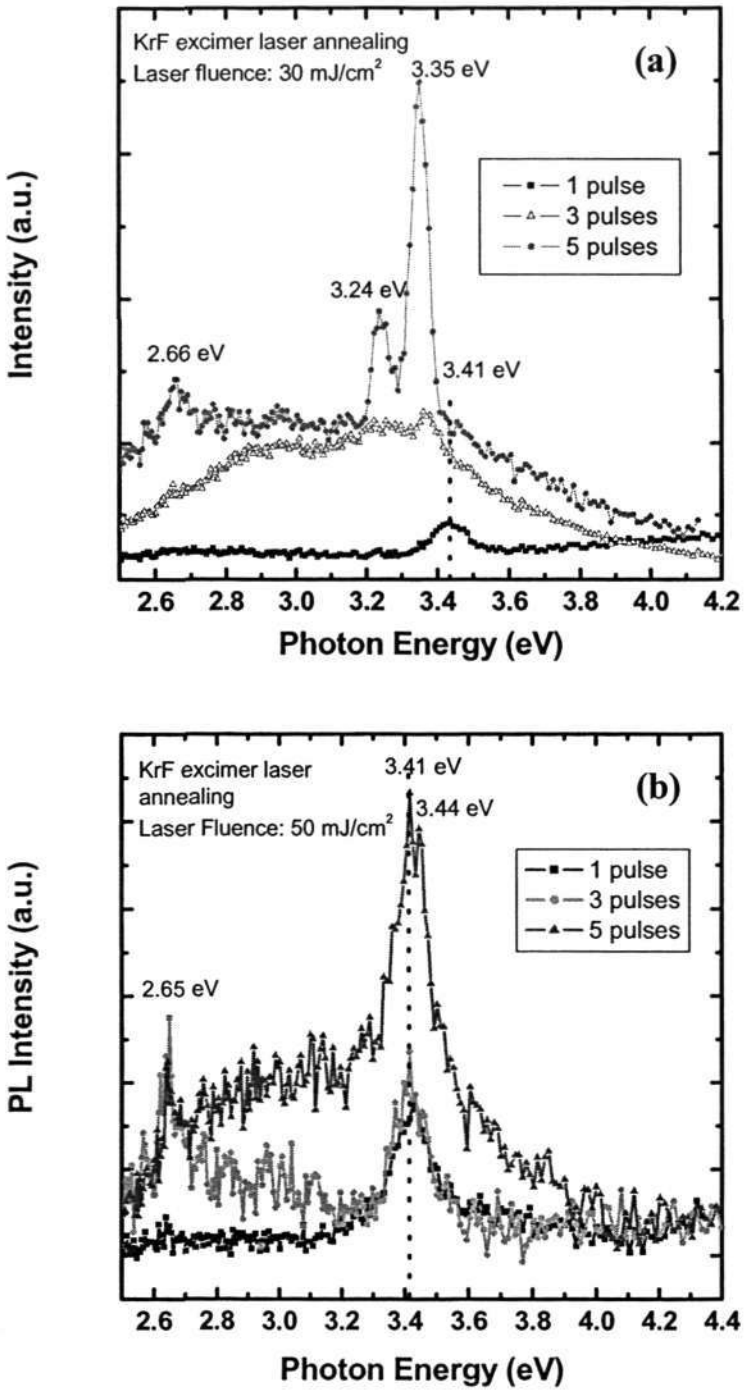

Figure 6-6 PL spectra recorded from the Ga_2O_3 nanoparticles after KrF excimer laser annealing with various laser pulses at laser fluence of (a) 30 mJ/cm^2 and (b) 50 mJ/cm^2.

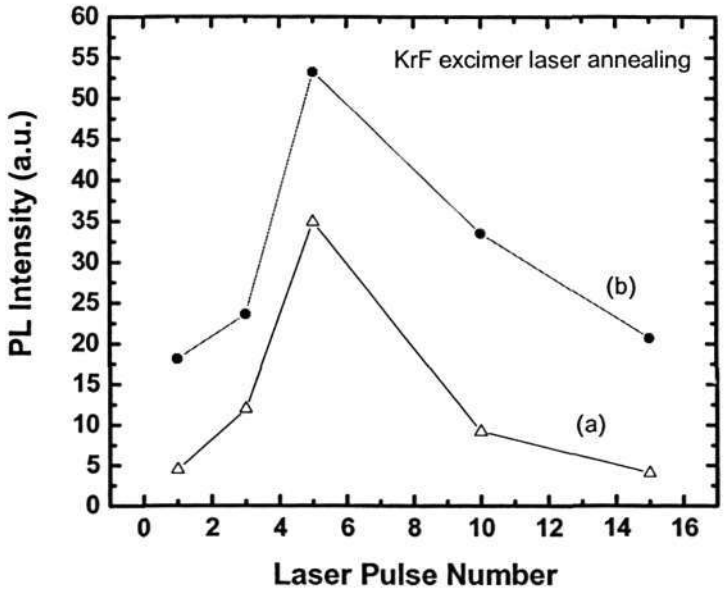

Figure 6-7 The dependence of PL peak intensity on laser pulse number at laser fluence of (a) 30 mJ/cm^2 and (b) 50 mJ/cm^2.

6.4 Summary

The influence of KrF excimer laser annealing on the crystallinity and photoluminescence improvement of Ga_2O_3 nanoparticles were investigated. In pulsed KrF excimer annealing, the surface morphology of the as-deposited Ga_2O_3 nanoparticle aggregates transformed to grain-like and film-like morphologies due to coalescence between the nanoparticles and surface melting with increasing laser fluence. However, after laser annealing at the laser fluence of 150 mJ/cm^2, a laser ablation effect was observed with significant removal of the as-deposited material from the substrate surface. On the other hand, the crystallinity of KrF excimer laser annealed samples improved when annealed at the laser fluence of 120 mJ/cm^2. Distinct diffraction peaks are observed at (104), ($\bar{2}$11) and (017). However, the sample suffered a loss in crystallinity when laser annealed at 150 mJ/cm^2. This clearly indicates that the as-deposited Ga_2O_3 nanoparticles were damaged after laser

annealing at 150 mJ/cm^2. Based on these findings, it is apparent that laser annealing at high fluence values, in the range of 150 mJ/cm^2, led to laser ablation effects as well as material damage, while in the range of 30 to 100 mJ/cm^2, the photon flux was not sufficient for to achieve good crystallinity of Ga_2O_3. In general, the PL intensity and linewidth increase with increasing fluences in KrF excimer laser-annealed samples. Linewidth broadening indicates a broad size distribution of nanoparticles which is consistent with larger grain growth at higher laser fluence. A larger redshift in the PL of the KrF excimer laser annealed samples was also observed at higher laser fluences. This is attributed to weaker quantum confinement effect as a result of grain growth. Lastly, the effect of multi-pulse KrF laser annealing on the PL emission of the Ga_2O_3 was also investigated. The PL intensities of the Ga_2O_3 samples are greatly enhanced with increasing pulse number from 1 to 5 but decreases with higher pulse number. When more than 5 laser pulses are employed at laser fluences of 30 mJ/cm^2 and 50 mJ/cm^2, laser ablation resulted in a reduction in the PL intensity. Hence, it is concluded that the crystallinity, blue and UV emission of the Ga_2O_3 nanomaterials can be greatly enhanced by performing laser annealing at optimum conditions (120 mJ/cm^2 $\leq$ laser fluence $<$ 150 mJ/cm^2 and laser pulses $\leq$ 5) for potential applications as blue or UV optical emitters.

CHAPTER 7

Synthesis of Ga_2O_3 Nanowires and Nanotubes by Pulsed Laser Ablation

7.1 Introduction

In recent years, one-dimensional nanoscale materials such as nanowires and nanotubes have drawn tremendous attention due to their novel physical properties and promising applications in electronic and optoelectronic nanodevices [222, 223]. Many binary oxide materials such as ZnO, In_2O_3, SnO_2, TiO_2 and Ga_2O_3 [224-228], have been widely synthesized as nanowires and nanotubes. A number of techniques for the synthesis of β-Ga_2O_3 nanowires have been reported including physical evaporation of Ga and Ga_2O_3 powders via the vapor-solid mechanism [229], oxide-assisted reaction between Ga_2O_3 and SiO_2 powders [230], thermal annealing of milled GaN powders in N_2 atmosphere [231], arc discharge of GaN powders in the presence of oxygen [232], heating of GaAs and Au [233] and laser ablation of Ga_2O_3 without the presence of catalyst [234]. Unfortunately, some of these techniques have severe drawbacks such as long processing time (2-15 hrs) and high annealing temperatures (800 to 1200°C) that lead to a very broad size distribution of β-Ga_2O_3 nanowires. It is also difficult to synthesize metal oxide nanowires by simply evaporating oxide powders because of their high melting point. Ga_2O_3 bulk powders require high processing temperatures to dissociate into Ga and O species to form nanomaterials. For the first time, this study introduces a novel and efficient synthesis route for the growth of β-Ga_2O_3 nanowires by pulsed laser ablation of GaN target with a suitable catalyst at temperatures from 400-800°C. Laser ablation of GaN generates activated Ga species that dissolve in the catalyst and react with oxygen to form β-Ga_2O_3 nanowires and nanotubes without

employing a high processing temperature. The synthesized β-Ga_2O_3 nanowires and nanotubes exhibit good dimension uniformity, high yield, blue and UV luminescence, which may find potential applications in nanoscale gas sensors and optoelectronic devices.

7.2 Experimental

β-Ga_2O_3 nanowires and nanotubes were grown on metal coated (5-20 nm) silicon (100) substrates by pulsed laser ablation of a 99.99% pure, pressed GaN target in a constant flow of nitrogen (99.9995%). A KrF excimer laser (Compex 102, LAMBDA PHYSIK) operating at a wavelength of 248 nm, pulse duration of 23 ns and pulsed energies ranging from 100 to 200 mJ per pulse was used to ablate the GaN target for 5 to 20 mins. The laser spot size on the target was approximately 0.04 cm^2. Before growth, N_2 gas was slowly introduced into the chamber to maintain the pressure at 10 Torr during laser ablation of GaN. A detailed explanation and schematic of the experimental setup can be found in Fig. 3-1. After the synthesis process, the brown products (wool-like) collected on the substrates were characterized using an X-ray diffractometer (XRD, Shimadzu 6000) with CuKα radiation, field emission scanning electron microscopy (FESEM, JOEL JSM 6340F), transmission electron microscopy (TEM, JEM 2010) equipped with an energy dispersive X-ray spectrometer (EDX). Photoluminescence measurements were carried out at room temperature with a fluorescence spectrophotometer (Shimadzu, RF-5301PC) to characterize the emission spectra of the β-Ga_2O_3 nanowires and nanotubes under the 266 nm UV fluorescent light excitation from a Xenon lamp.

7.3 Results and Discussion

7.3.1 Diameter Control of Ga_2O_3 Nanowires

7.3.1.1 Effect of Growth Temperature

To investigate the effect of growth temperature on the size dependence of Ga_2O_3 nanowires, various temperatures from 400 to 800°C were employed during the growth of Ga_2O_3 nanowires, via laser ablation of a pressed GaN target in N_2. The growth temperature for the synthesis of Ga_2O_3 nanowires is determined with the aid of the Au-Ga phase diagram (Fig. 2-2). The Au-Ga phase diagram exhibits a eutectic composition of 22.1% Ga at 282°C. The eutectic temperature limits the minimum temperature for nanowire synthesis because the kinetics and solubility of Ga in Au is limited at temperatures below eutectic temperatures and only a limited concentration of Ga will dissolve in Au. Therefore, based on the Au-Ga phase diagram, growth temperatures above the eutectic temperature of 282°C were selected for this study (400 to 800°C). Figures 7-1(a) to (e) present FESEM images of the synthesized products grown on Au-coated (10 nm) Si wafers at various growth temperatures. The FESEM images illustrate a strong correlation between the growth temperature with the morphology of the synthesized products. Dense and entangled formation of Ga_2O_3 nanowires are clearly apparent when synthesized at temperatures ≥ 600 °C. However, at 400°C and 500°C, no nanowires were formed and only hillock structures were observed on the Si substrates. Clearly, the diameter and size distribution of the nanowires were found to increase with increasing temperature (see Fig. 7-2). According to the VLS mechanism, the diameters of the initial catalysts on the substrates can have strong influence on the diameters of the nanowires [235]. In this study, the initial Au thin films on silicon substrates were deposited using e-beam evaporation under the same conditions. However, the Au thin films self-aggregate to

form Au nanoclusters or nanoparticles at elevated temperatures. To systematically study the correlation between the diameters of the nanowires and the size of the Au nanoparticles on the substrate prior to nanowires growth, the size distribution of the Au nanoparticles formed after annealing under N_2 ambient for 15 mins at 600°C and 800°C were analyzed. The FESEM and AFM images of the Au nanoparticles formed after annealing in N_2 at 600°C and 800°C are shown in Fig. 7-3. The size of the Au nanoparticles as a function of annealing temperature at 600°C and 800°C are 10 ± 2 nm and 20 ± 5 nm, respectively. It is therefore apparent that the average size of the Au nano-islands decreased when a lower growth temperature was adopted. Similarly, the diameter of the nanowires decreases with lower growth temperatures. Hence, it is proven that the initial diameter of the Au (catalyst) nanoparticles plays an important role in tuning the diameter of the nanowires. The detailed growth mechanism of the Ga_2O_3 nanowires will be discussed in the later sections.

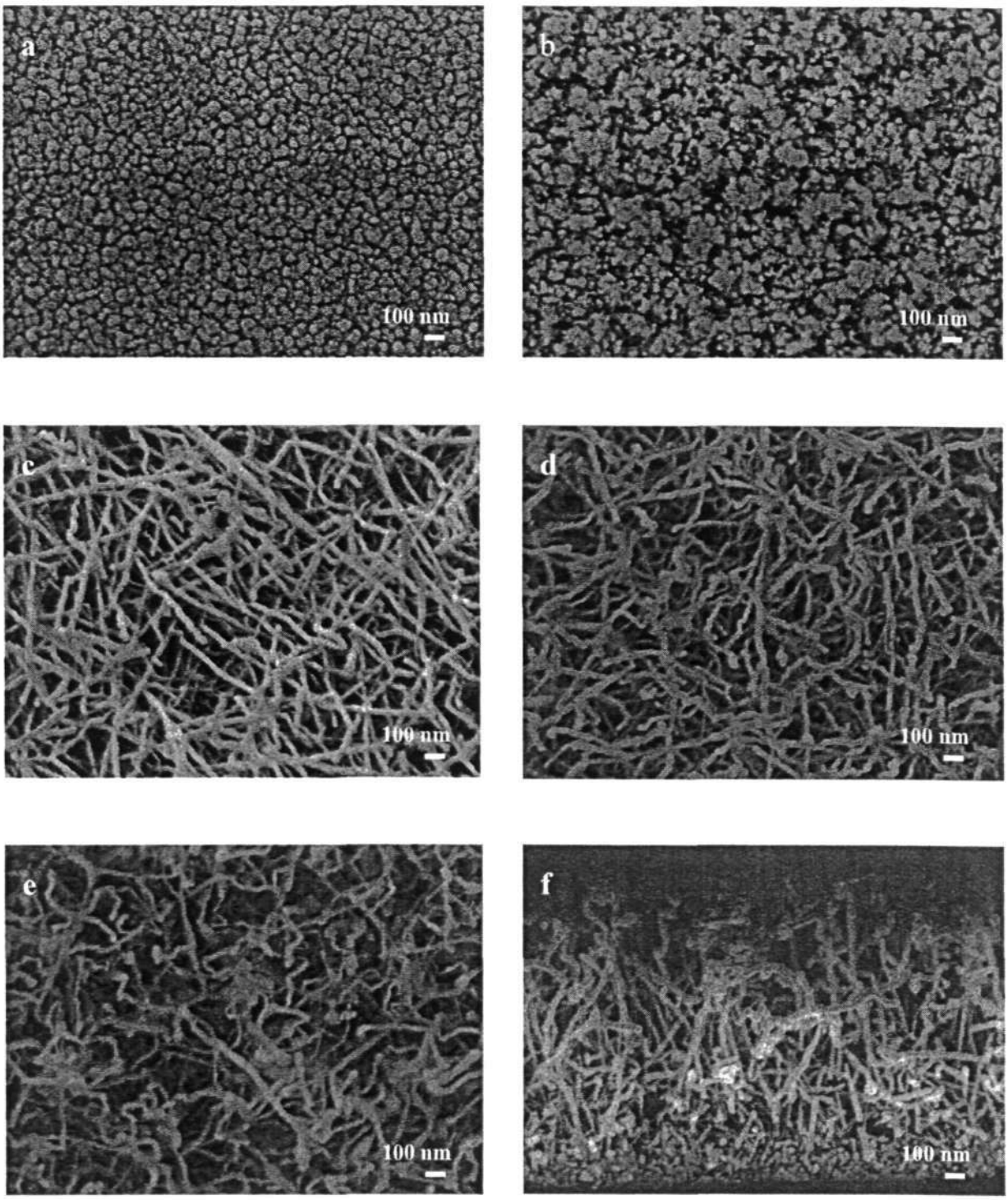

Figure 7-1 FESEM images of Ga_2O_3 nanoclusters and nanowires synthesized at (a) 400°C, (b) 500°C, (c) 600°C, (d) 700°C, (e) 800°C and (f) cross-section view of nanowires. The laser fluence employed was 1.5 J/cm^2 and the scale bar is 100 nm.

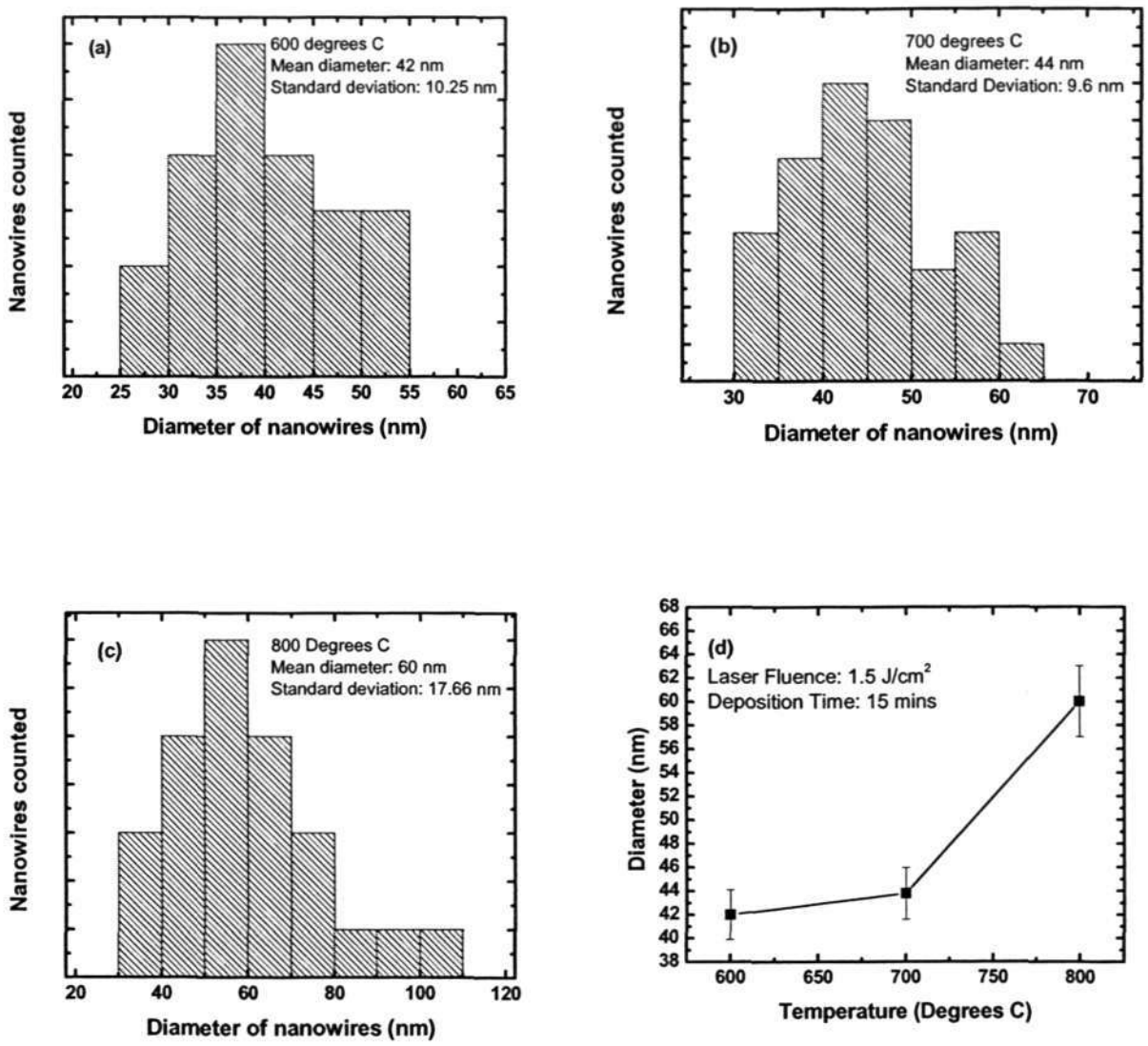

Figure 7-2 Size distributions of Ga_2O_3 nanowires synthesized at (a) 600°C, (b) 700°C, (c) 800°C and (d) diameter of Ga_2O_3 nanowires as a function of growth temperature.

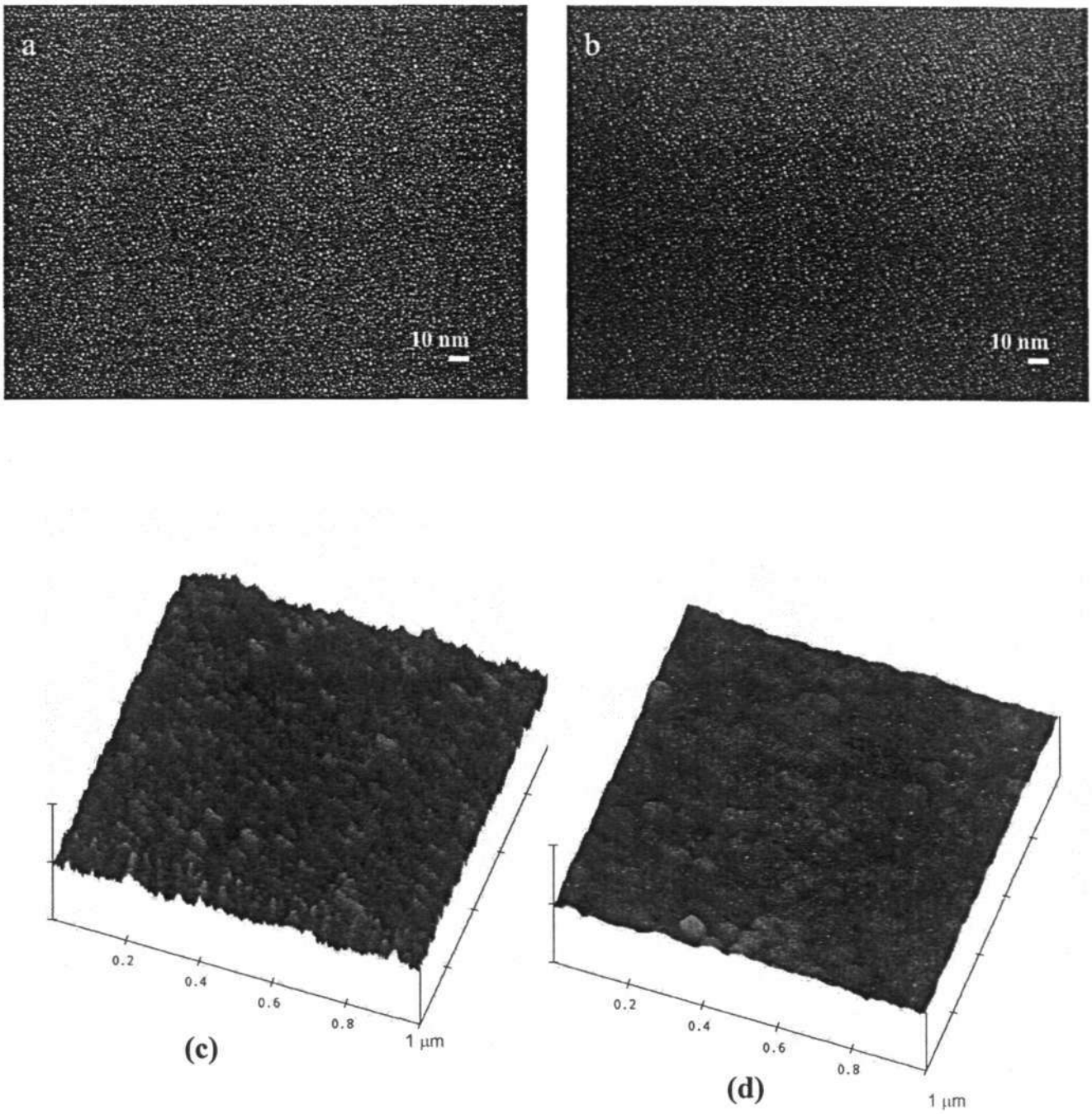

Figure 7-3 FESEM images of Au nanoparticles after annealing at (a) 600°C and (b) 800°C in nitrogen gas ambient for 15 mins. The scale bar is 100 nm. Corresponding surface roughness of Au nanoparticles annealed at (c) 600°C and (d) 800°C.

7.3.1.2 Effect of Growth Pressure

Figure 7-4 shows the FESEM micrographs of the Ga_2O_3 nanowires grown on Au-coated (10 nm) silicon substrates at 700°C and laser fluence of 1.5 J/cm^2 for 15 mins. The size dependence of Ga_2O_3 nanowires on different growth pressures have been evaluated at 0.01, 0.1 and 10 Torr of nitrogen. Figure 7-4 (b), (d) and (f) show the average diameters of the nanowires are 27 ± 15.5 nm, 35 ± 10.75 nm and 44 ± 18.2 nm when grown at 0.01, 0.1 and 10 Torr, respectively. Clearly, most of the synthesized nanowires have become wider with increasing growth pressure. From earlier observation, it was found that upon heating the sample to 700°C, Au thin film on the substrate surface self-aggregate to form Au nuclei with diameters of approximately 15 ± 2 nm. Here, it is assumed that the initial diameters of the Au nuclei are similar for all 3 samples before laser ablation began at 0.01, 0.1 and 10 Torr. This assumption is based on the fact that N_2 was only introduced into the processing chamber to maintain the deposition pressure at 0.01, 0.1 and 10 Torr when the synthesis temperature had reached 700°C. However after laser synthesis, it was found that the diameters of Ga_2O_3 nanowires have increased with increasing deposition pressure, they also possessed larger diameters as compared to the initial diameter of Au nuclei. Since the diameter of nanowires is related to the size of the catalyst droplet [236], clearly the initial diameter of Au nuclei has increased during the growth of Ga_2O_3 nanowires. Recently, Hannon *et al.* [237] has reported that during nanowires growth, Au preferentially migrates from smaller catalyst droplets to the larger ones to reduce the overall droplet surface area. Hence, it is likely that during the synthesis of Ga_2O_3 nanowires, Au in small catalyst droplet have diffused to larger catalyst droplets that led to an increase in the diameter of Ga_2O_3 nanowires. Furthermore during VLS growth, if supersaturation in each catalyst droplet is not met,

the precipitation of 1D-nanowire would be difficult. Whereas more and more Au in small catalyst droplets would migrate to form larger catalyst droplets. For instance, when the ambient gas pressure is high, collision rate between the ablated species and ambient gas molecules increases in the confinement region and lesser ejected species are able to reach the substrate surface. In other words, lesser ejected species would be absorbed by the Au nuclei. However, when the ambient gas pressure is low, more ejected species are able to reach the substrate surface which is due to lower probability in collision with the ambient gas molecules. These ablated materials, upon reaching the substrate would diffuse into the Au nuclei which serve as 3D nucleation sites for the growth of Ga_2O_3 nanowires via VLS growth mechanism. If more ejected species are able to reach the substrate surface and are quickly absorbed by the Au nuclei, the Au-catalyst droplet would take a lesser time to meet the supersaturation requirement for nanowires growth. Furthermore, the migration of Au to form larger catalyst droplet would be limited. Hence, it is proposed that the time to reach supersaturation of Ga vapor species in Au catalyst droplets at lower deposition pressure is shorter as compared to higher deposition pressure. Moreover, a shorter time to reach supersaturation would also limit migration of Au into the catalyst droplets and effectively control the final diameters of the catalyst droplets as well as Ga_2O_3 nanowires.

Table 7-1 Diameter dependence of Ga_2O_3 nanowires on the pressure of N_2.

	Growth Pressure		
	0.01 Torr	0.1 Torr	10 Torr
Average diameters of Ga_2O_3 Nanowires	27 ± 15.5 nm	35 ± 10.75 nm	44 ± 18.2 nm

It is also found that the density of the nanowires changes with the growth pressures. The growth density of the nanowires is higher when synthesized at lower growth pressures. As shown in Fig. 7-4, the density of the nanowires grown at 0.01 Torr is larger than that obtained at 0.1 Torr. In Fig. 7-4 (f), it can be seen clearly that the Ga_2O_3 nanowires synthesized at 10 Torr, exhibit a broader size distribution as compared to those deposited at 0.01 Torr (Fig 7-4b) and 0.1 Torr (Fig. 7-4d). Based on the above-mentioned results, it is obvious that the growth pressure plays an important role in controlling the diameter, density and size distribution of the Ga_2O_3 nanowires.

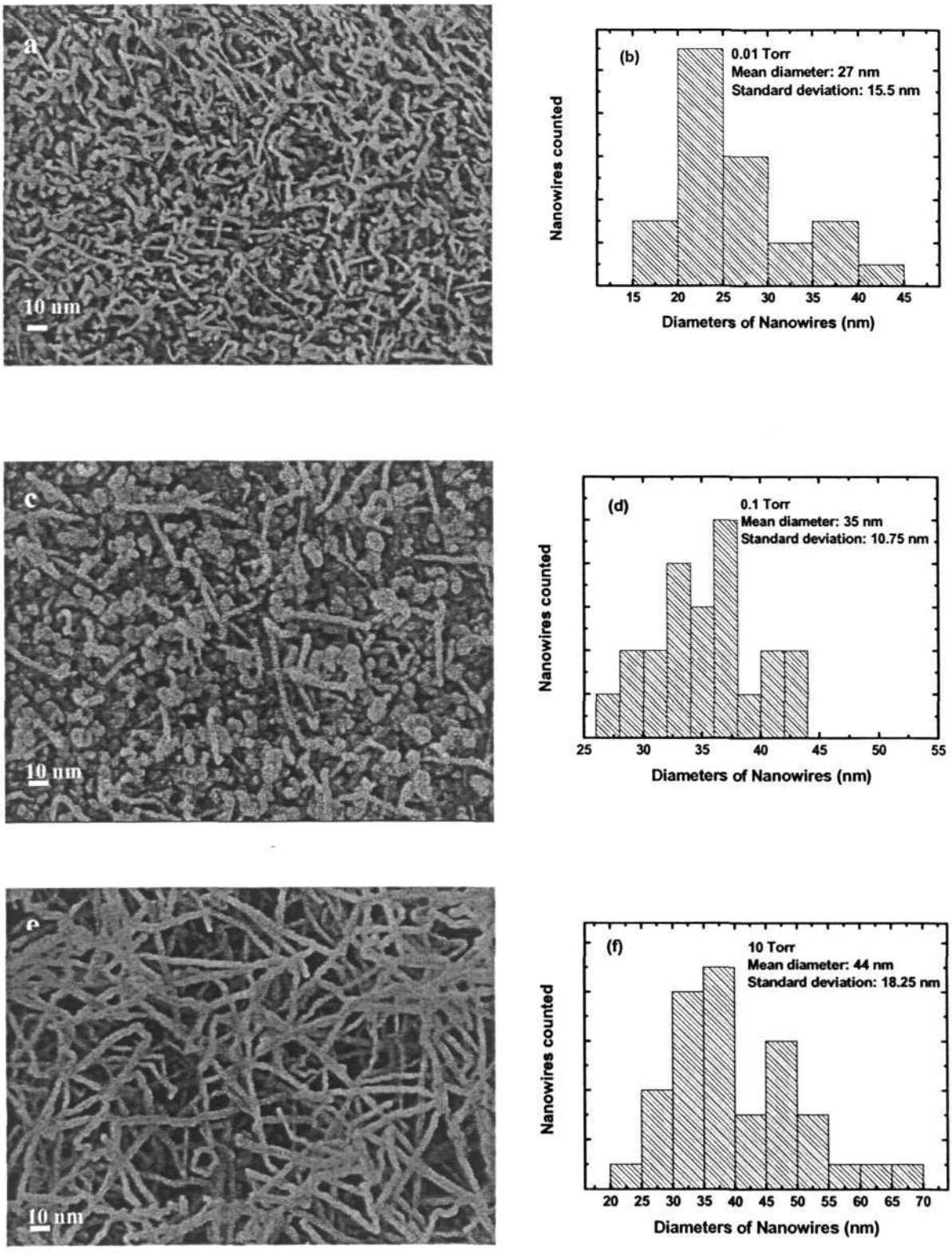

Figure 7-4 FESEM images of Ga_2O_3 nanowires synthesized on Au-coated Si substrates at a laser fluence of 1.5 J/cm^2 and 700°C for 15 min under various growth pressures: (a) 0.01, (c) 0.1 and (e) 10 Torr. The scale bar represents 10 nm.

7.3.1.3 Effect of Laser Fluence

Figure 7-5 shows the FESEM images of the Ga_2O_3 nanowires grown at laser fluence of (a) 1.5 J/cm^2 and 0.9 J/cm^2. At the laser fluence of 1.5 J/cm^2, nanowires have been observed. However, no nanowires and only hillock structures were observed when the lower laser fluence was employed for the growth. Clearly, there exists a minimum laser fluence for the formation of Ga_2O_3 nanowires. High laser fluence will result in high impingement flux of the evaporated species from the laser irradiated target whereby high impingement flux is essential for the control of supersaturation in obtaining 1D nanostructures which will be discussed further in section 7.6 . Therefore, high laser fluence is essential to generate enough Ga vapor species to exceed the saturation vapor pressure for supersaturation and to sufficiently supply enough flux to the substrate to meet the supersaturation requirement for nanowires growth. Hence it is obvious that the laser fluence directly controls the supersaturation factor to form 1D nanostructures.

In addition, the synthesis of Ga_2O_3 nanowires is related to the formation of 3D nucleation sites (Au nanoparticles) at the initial growth stage. These nucleation sites serve as energetically favorable sites for 3D growth mode as the surface energy of these nucleation sites is theoretically higher than that of a flat surface with no nucleation sites. Furthermore, these 3D nucleation sites can promote atomic adsorption and diffusion efficiently. Thus the formation of 3D nucleation sites at the initial growth stage is believed to play an important role in the synthesis of nanowires. The diameter of nanowires can be tuned accordingly by controlling the dimension of 3D nucleation sites through adjusting the growth parameters.

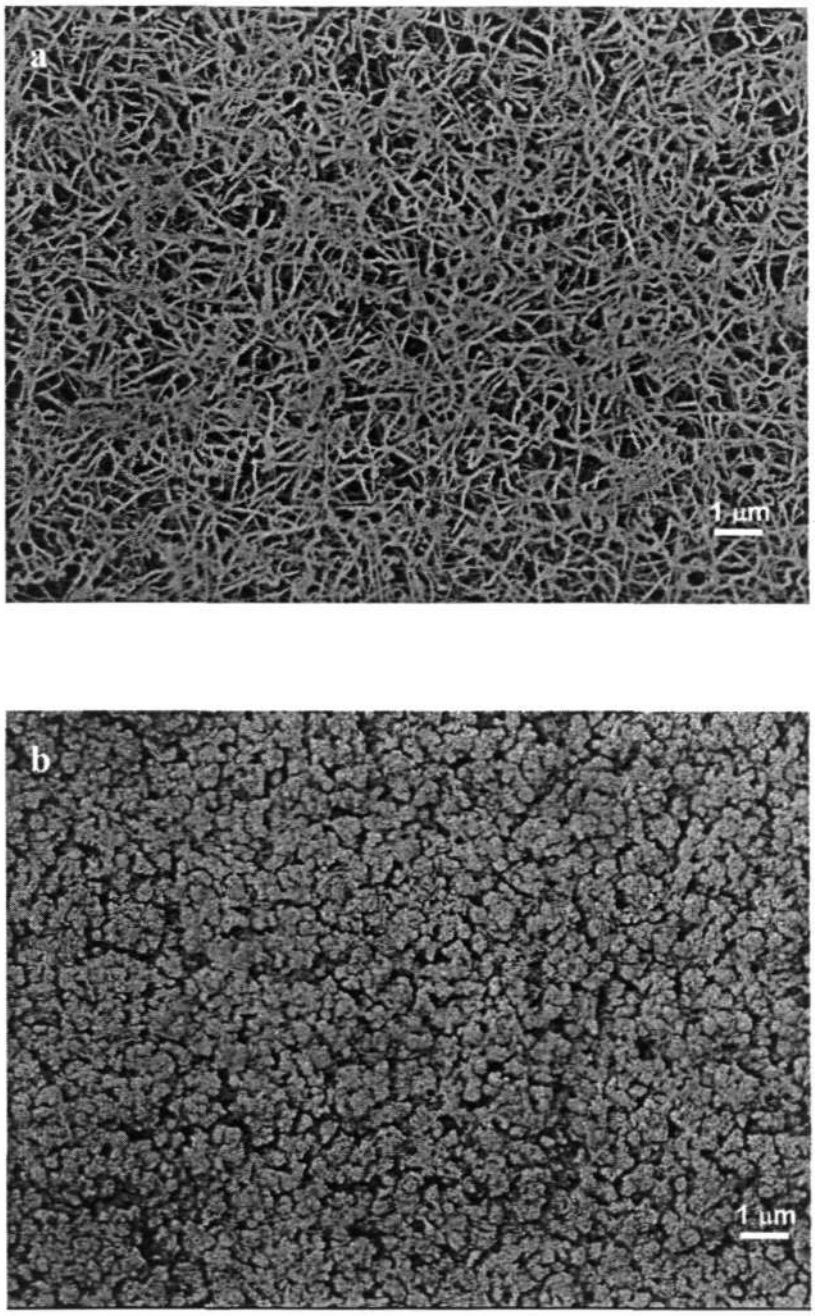

Figure 7-5 FESEM image of Ga_2O_3 nanowires synthesized at 10 Torr, 700°C and laser fluence of (a) 1.5 J/cm^2 and (b) 0.9 J/cm^2. The scale bar is 1 μm.

7.3.2 Structural Characterization of Ga_2O_3 Nanowires

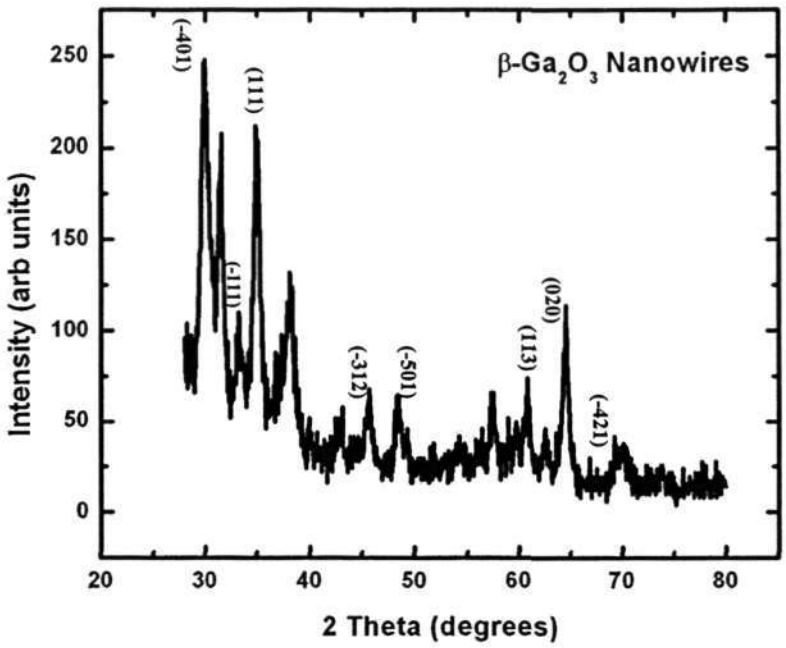

Figure 7-6 XRD pattern of β-Ga_2O_3 nanowires grown at 700°C on Au-coated Si substrates. The pressure during deposition was kept at 10 Torr and the laser fluence was set at 1.5 J/cm^2.

Figure 7-6 shows a typical XRD pattern of β-Ga_2O_3 nanowires deposited at 700°C. The diffraction peaks can be indexed as a monoclinic phase Ga_2O_3 (JCPDS card no. 41-1103). The lattice constants of the nanowires are a = 12.227 Å, b = 3.0389 Å, c = 5.8079 Å and β = 103.820°. No diffraction peaks of Ga or other impurities have been found in our samples, therefore indicating high purity and crystallinity of the nanowires. Further analysis of the structure, morphology and composition of the synthesized products have been characterized using TEM and selected area electron diffraction (SAED).

Figure 7-7 (a), (b) and (c) shows the typical TEM images of the β-Ga_2O_3 nanowires synthesized at 600°C, 700°C and 800°C respectively. Each nanowire has a

uniform diameter along its entire length and the typical diameters of the nanowires are in the range of 30-100 nm. From the TEM images, the diameter of the nanowires as a function of growth temperatures at 600°C, 700°C and 800°C are 30 ± 2 nm, 45 ± 3 nm and 100 ± 5 nm respectively. Clearly, the diameter of the nanowires is found to increase with higher growth temperature, which is consistent with the FESEM results. The inset in Fig. 7-7c depicts the selected area electron diffraction pattern of the nanowires. The SAED patterns were recorded with electron beam perpendicular to the long axis of the nanowire. The SAED pattern can be indexed for the [010] zone axis of crystalline β-Ga_2O_3, revealing the single crystal nature of the β-Ga_2O_3 nanowires. A spherical nanoparticle with diameter of 25 nm was observed at the end of the nanowires (shown in Fig. 7-7d). The surfaces of the wire terminate with thin (about 2 nm) and smooth amorphous layers. EDX measurement made on the terminal nanoparticle indicates that the nanoparticle consist of only Au and Ga with no presence of oxygen or silicon. The presence of the Au/Ga alloy nanoparticle at the end of the nanowires indicates that the growth of the β-Ga_2O_3 nanowires follows the vapor-liquid-solid mechanism. It is also evident that the Au/Ga nanoparticle alloy acts as a reactive site to direct and confine the growth of the β-Ga_2O_3 nanowires, since the diameter of the β-Ga_2O_3 nanowire is comparable to the diameter of the metal alloy nano-tip. Sharp kinks were also observed along the length of the nanowires and these kinks may be interpreted as defects such as twinnings and stacking faults that occurred during the growth of the β-Ga_2O_3 nanowires. Wang *et al.* [238] had previously reported that structure defects play a very important role in the formation of the nanowires. Kinks provide energetically favourable sites for incoming atoms and clusters to stack unidirectionally into the nanowires. In many cases, it was revealed that structural defects play important roles in the nucleation of triple, quadruple and

quintuplet junction points of microtwin variants that serve as nucleation centers to initiate the growth of silicon nanowires [239]. In addition, Zhang *et al.* demonstrated that twin defects play an important role in the growth of Ga_2O_3 nanowires by physical evaporation [240]. Figure 7-8(a) and (b) show lattice-resolved HRTEM images of individual Au/Ga alloy nanoparticle and β-Ga_2O_3 nanowire respectively. In Figure 7-8(b), lattice fringes of the $(\bar{2}01)$ planes with *d* spacing of 0.45 nm for the β-Ga_2O_3 nanowires can be clearly observed. It also reveals that the wire is single crystalline and the examined region is free from dislocation and stacking faults.

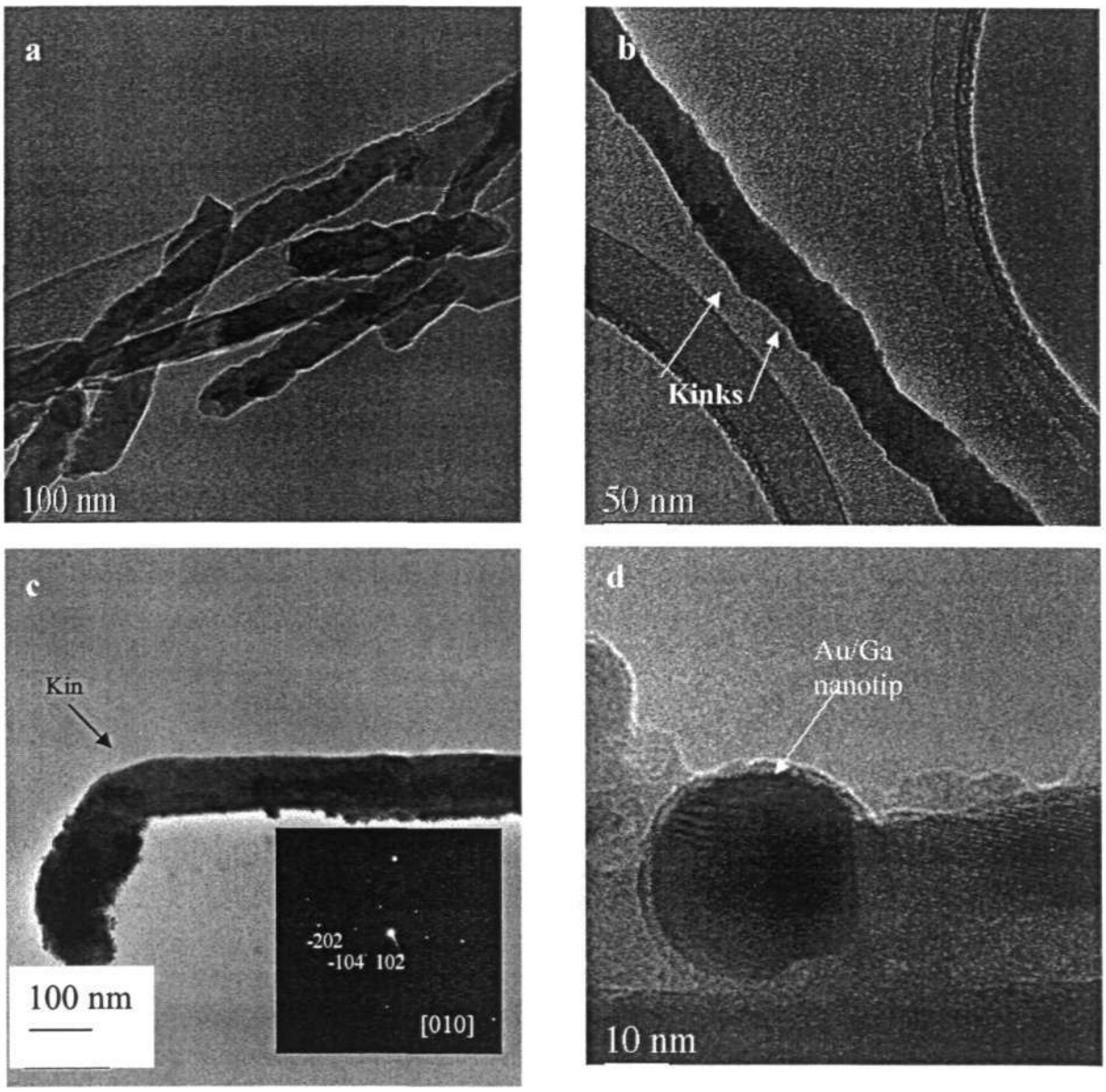

Figure 7-7 TEM images of Ga_2O_3 nanowires synthesized at 10 Torr, laser fluence of 1.5 J/cm^2, (a) 600°C, (b) 700°C and (c) 800°C for 15 mins. The corresponding selected area diffraction (SAED) pattern recorded along the [010] zone axis is shown in inset (c). (d) TEM image of Au/Ga catalyst nanoparticle terminated at the end of the Ga_2O_3 nanowire.

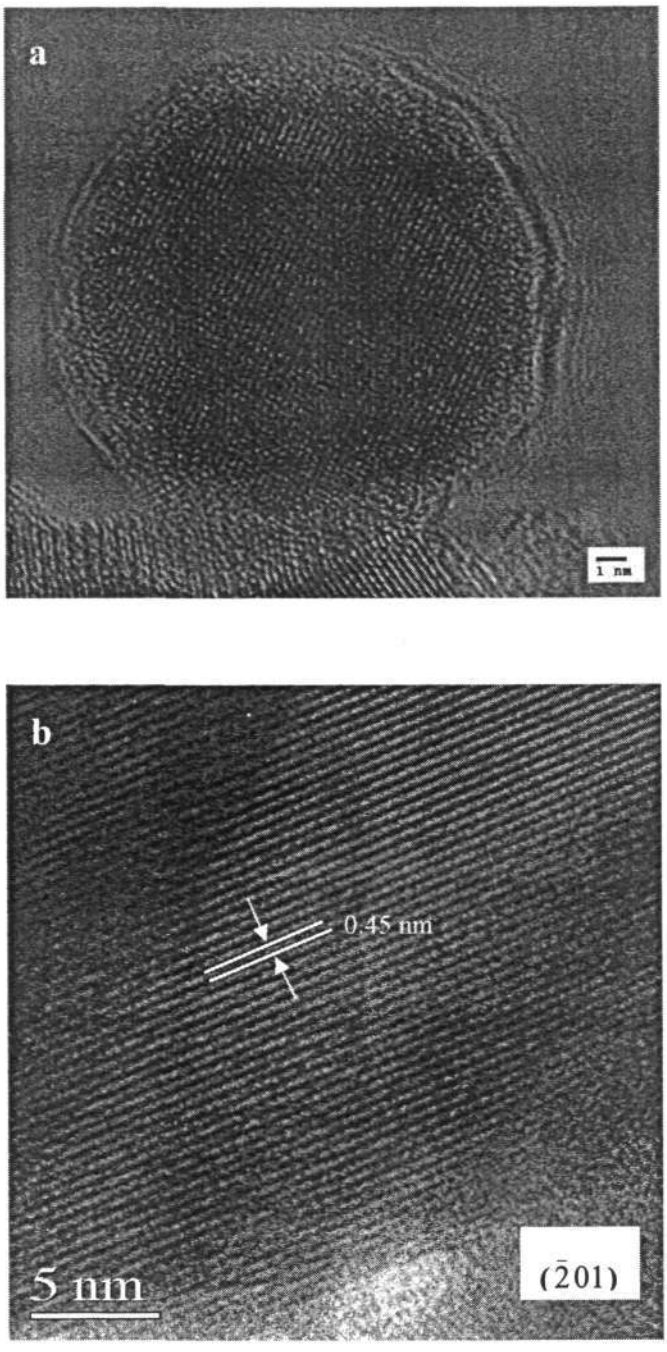

Figure 7-8 High resolution TEM images of (a) Au/Ga catalyst nanoparticle and (b) Ga_2O_3 nanowire synthesized at 10 Torr, 700°C and laser fluence of 1.5 J/cm^2 for 15 mins.

7.3.3 Length Control

To investigate the issue of length control, Ga_2O_3 nanowires were synthesized using 10 nm Au thin film as the catalyst, at 10 Torr in N_2 for a series of growth times. The growth temperature was kept at 700°C. Figure 7-9 presents the FESEM images of the nanowires products deposited for 2, 5 and 15 min. It is clearly observed that there is a strong correlation of growth time with nanowires length. Quantitative analysis of the wire lengths as a function of 2, 5, and 15 minutes growth times showed wire lengths of 0.5 ± 0.1, 0.8 ± 0.2, 4.2 ± 0.5 μm. Figure 7-9(d) depicts the systematic increase in the length of the nanowires with growth time and also shows that the distribution of lengths is small at shorter growth times. From the linear fit, it is postulated that the nucleation stage of the VLS process proceeds after 1.15 mins because a finite period of time is required for complete saturation of the alloy droplets. After this stage, it is believed that the wires elongate at a constant rate, resulting in longer wires when the growth time increases. Gudiksen *et al.* [130] also studied the effect of growth time on nanowire length. Similarly, he reported a systematic increase in nanowires length with growth time and established a well-defined and narrow length distribution of InP nanowires.

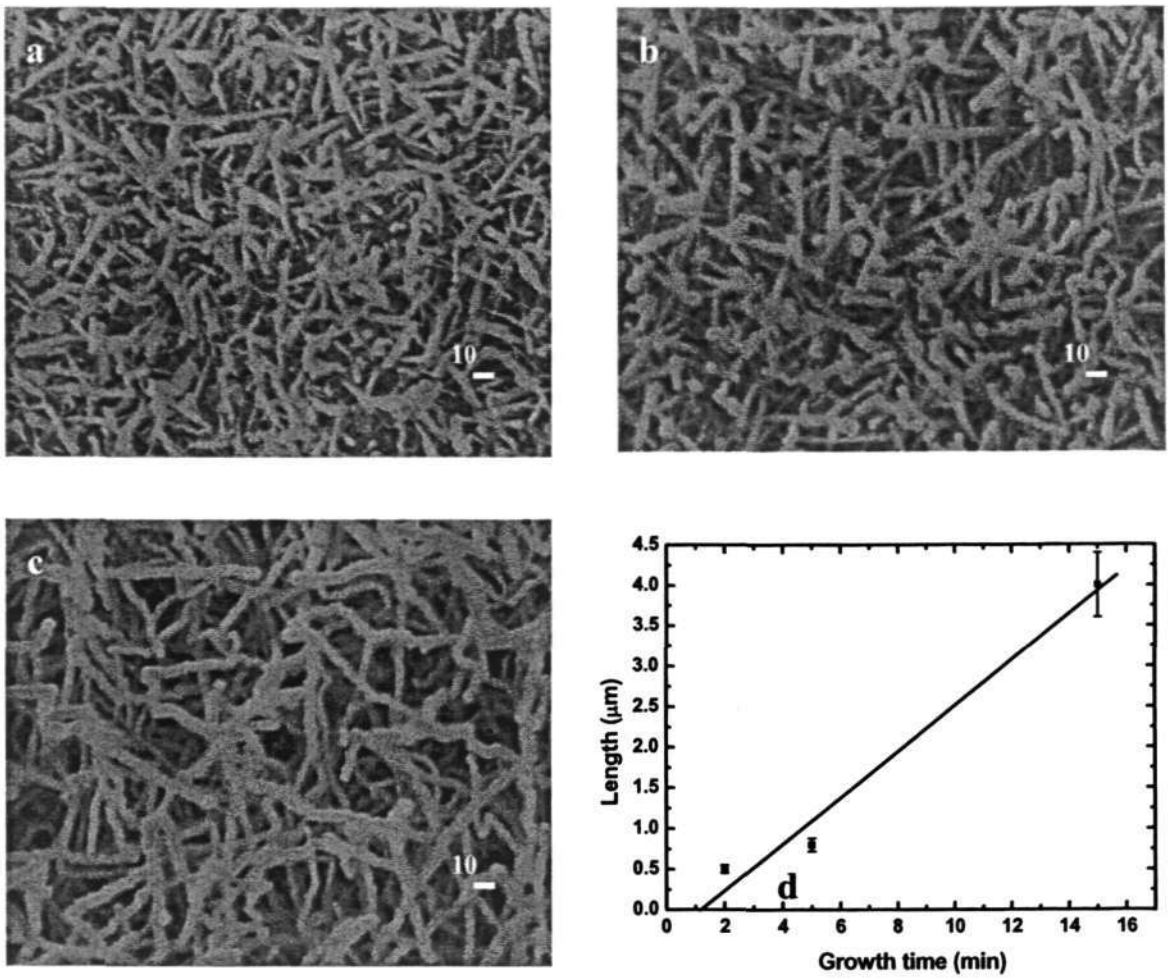

Figure 7-9 FESEM image of Ga_2O_3 nanowires synthesized at 10 Torr, 700°C and laser fluence of 1.5 J/cm^2 for (a) 2 mins, (b) 5 mins and (c) 15 mins. The scale bar is 10 nm.

7.3.4 Growth Mechanism of Ga_2O_3 Nanowires

The mechanism for nanowires growth is catalyst driven and is related to the vapor-liquid-solid (VLS) model reported for nanowires synthesis of other materials [241]. In the present work, the vapor-liquid solid (VLS) growth of the catalyst-assisted β-Ga_2O_3 nanowires may involve the following steps. Schematic illustration of the VLS growth is also depicted in Fig. 7-10. Firstly, the laser irradiation of the GaN target with a KrF excimer laser (λ=248nm) causes the decomposition of GaN to generate Ga species via a multiphoton absorption process. GaN dissociates via the following possible reactions **(I)**:

$$4GaN\ (s) \rightarrow 4Ga\ (g) + 2N_2\ (g) \qquad (1)$$

$$4Ga\ (g) + 3O_2\ (g) \rightarrow 2Ga_2O_3\ (s) \qquad (2)$$

It is proposed that multiphoton absorption of GaN from the 248 nm KrF laser beam (4.9 eV) resulted in the breaking of the chemical bonds between gallium and N_2 (~ 8.9 eV). Thereby, it led to the dissociation to form Ga and N_2 gas. The Ga vapor **(II)** is then transported to the Au/Si substrate. According to the Au/Ga phase diagram [116], Au becomes liquid at 600°C and therefore Ga vapor is able to dissolve into the nanometer-sized liquid Au catalyst on the silicon substrate, forming liquid Au/Ga metal alloy. Each liquid Au/Ga nanodroplet acts as a nucleus that is energetically favoured to absorb the incoming Ga vapor. When the droplets become supersaturated **(III)**, the metallic Ga precipitated out of the liquid alloy droplet and recombined with residual oxygen in the chamber to form Ga_2O_3 nanocrystals and further grow into nanorods or nanowires. The formation of Ga_2O_3 phase is favored as Ga atoms have greater affinity with O_2 than N_2. In addition, Ga having a better solubility of oxygen

than Au would result in O_2 atoms selectively dissolve in Ga atoms instead of Au atoms. The presence of O_2 in the chamber can be attributed to low vacuum degree and impure N_2 (99.995%) gas utilized in the experiment.

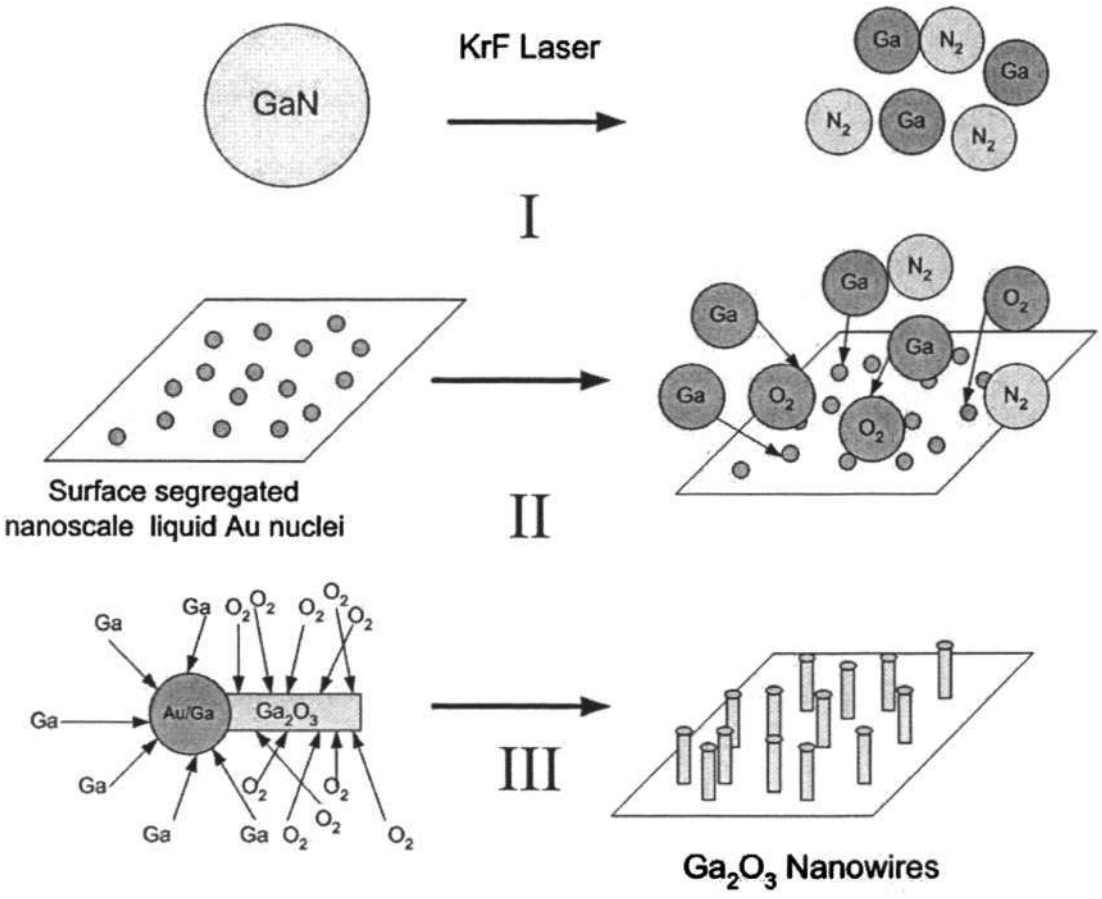

Figure 7-10 The proposed VLS growth mechanism for Ga_2O_3 nanowires.

7.3.5 Catalyst Effect on the Growth of Ga_2O_3 Nanowires

Previously, it has been demonstrated that Au is an effective catalyst suitable to mediate the growth of Ga_2O_3 nanowires via VLS mechanism. Several past studies have shown that the surface morphology and optical properties of the nanowires can be altered by utilizing different catalyst. To date, Au [242], Ir [243] and Pt [244] catalysts has been investigated with regard to their catalytic role in synthesizing 1D Ga_2O_3 nanostructures. To the best of our knowledge, the synthesis of Ga_2O_3 nanowires with Ag and Pd catalysts has not been reported so far. Therefore, in this section, Ga_2O_3 nanowires were synthesized by the VLS process using Pd and Ag thin films (10 nm) as catalysts sources at 10 Torr, in an N_2 ambient on Si substrates. The growth temperature was kept at 700°C for both syntheses. Figures 7-11 (a) and (b) present FESEM images of the Ga_2O_3 nanowires synthesized with Pd and Ag catalyst, respectively. Both FESEM images reveal a high density of nanowires grown on Si susbstrates with lengths up to a few microns. The FESEM results clearly indicate that there is no significant difference between the surface morphologies of the Pd-catalyzed, Ag-catalyzed and Au-catalyzed nanowires. However, Pd-catalyzed nanowires reveal thinner diameters as compared to Ag-catalyzed and Au catalyzed nanowires. This is correlated with the initial size of the Pd, Ag and Au nanoparticles before nanowires growth. Table 7-2 presents the initial diameters of the Pd, Ag and Au nanoparticles after annealing at 700°C for 15 mins in an N_2 ambient.

Table 7-2 Diameter of initial catalyst nanoparticles annealed in nitrogen at 700°C for 15 mins.

Catalyst	Diameter (nm)
Pd	15 ± 1
Ag	20 ± 3
Au	12 ± 0.5

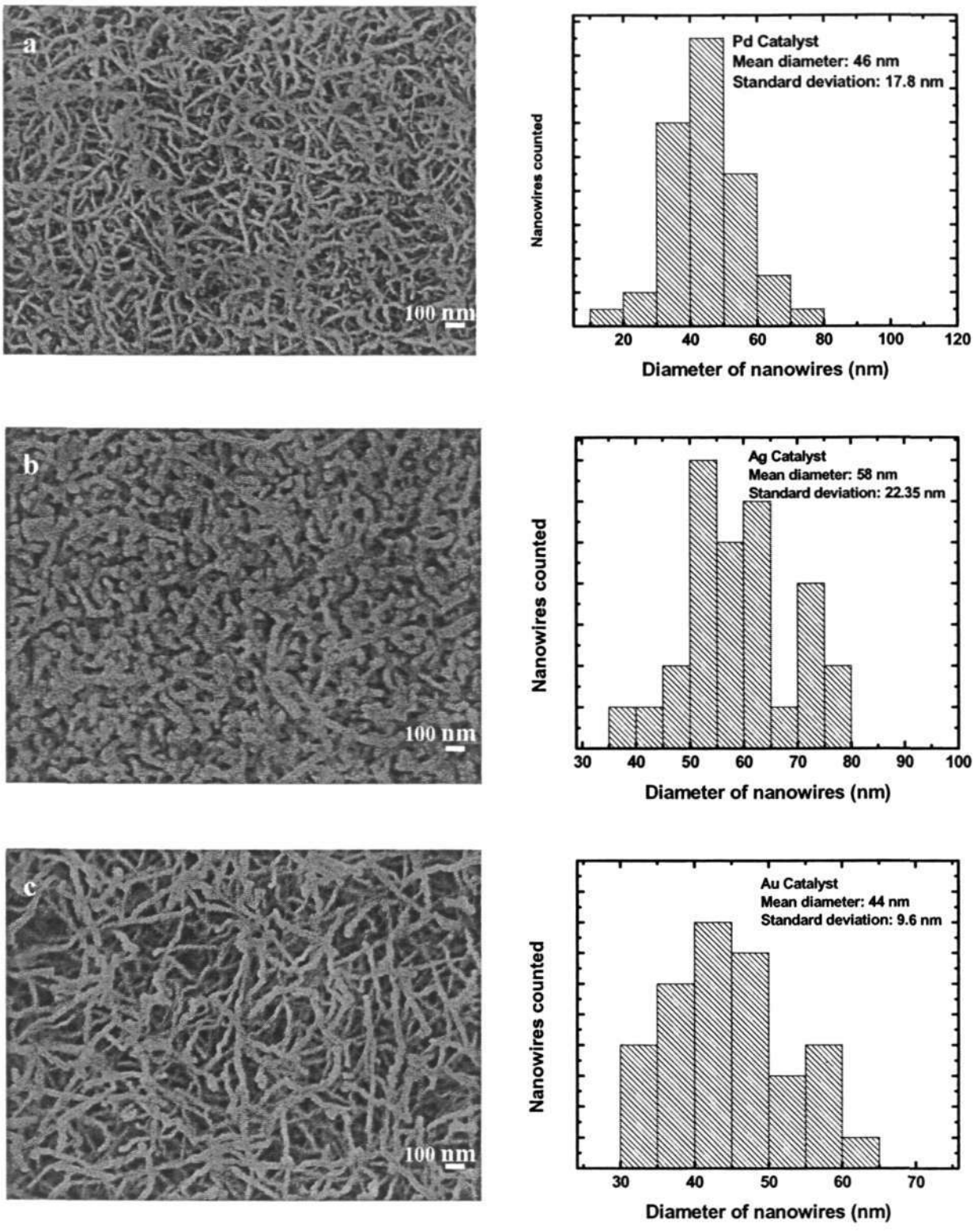

Figure 7-11 FESEM image of (a) Pd-catalyzed, (b) Ag-catalyzed and (c) Au-catalyzed Ga_2O_3 nanowires synthesized at 10 Torr, 700°C and laser fluence of 1.5 J/cm^2 for 15 mins. The scale bar is 100 nm.

From the FESEM images, it is found that the average diameters of the Pd-catalyzed, Ag-catalyzed and Au-catalyzed nanowires are approximately 46 ± 17.8 nm, 58 ± 22.35 nm and 44 ± 9.6 nm, respectively. Figure 7-12(a) and (b) presents low magnification TEM images of the Pd-catalyzed β-Ga_2O_3 nanowires synthesized at 10 Torr and growth temperature of 700°C in N_2 ambient, respectively. As seen in the TEM image, the Pd-catalyzed nanowires have uniform diameters along their entire lengths and the typical diameters of the nanowires are in the range of 20-50 nm. A spherical nanoparticle with diameter of ~ 4.8 nm, was observed at the end of the nanowires (shown in Fig. 7-12b). The EDX measurement made on the terminal nanoparticle indicates that the nanoparticle consists of only Pd and Ga, with no presence of oxygen. The presence of the Pd/Ga alloy nanoparticle at the end of the nanowire similarly indicates that the growth of the β-Ga_2O_3 nanowires follows the vapor-liquid solid mechanism. The presence of many kinks along the length of the nanowires is also observed. Figure 7-12(c) shows the lattice-resolved HRTEM image of the β-Ga_2O_3 nanowires. The HRTEM results further confirm the monoclinic nature of the Ga_2O_3 nanowires. The lattice spacing in the HRTEM images matched that for the monoclinic β-Ga_2O_3. Lattice fringes of the $(\bar{2}02)$ planes with *d* spacing of 0.36 nm for the β-Ga_2O_3 nanowires can be clearly observed. The ring pattern in the SAED image (Fig. 7-12d) confirms the polycrystalline nature of the nanowires.

Figure 7-13(a) depicts low magnification TEM images of the Ag-catalyzed β-Ga_2O_3 nanowires synthesized at 10 Torr and a growth temperature of 700°C in N_2 ambient. Similar to the Au- and Pd-catalyzed Ga_2O_3 nanowires, the Ag-catalyzed nanowires are straight and long with diameters of about 34 nm in the TEM image. However, unlike the Au- and Pd-catalyzed Ga_2O_3 nanowires, the Ag-catalyzed nanowires show lesser kinks along the length of the nanowires. The high-resolution

TEM image the box region of Fig. 7-13(a) is illustrated in Fig. 7-13(b). It reveals that the centre region (~ 4.1 nm) of the nanowires is hollow. The visible lattice fringes of (100) planes of the β-Ga_2O_3 structure with d spacing of 0.56 nm are observed. The TEM results indicate that using Ag catalysts has resulted in the formation of β-Ga_2O_3 nanotubes. To the best of our knowledge, this is the first time that Ga_2O_3 nanotubes are fabricated by UV pulsed laser ablation, with the aid of Ag catalysts. Wu *et al.* [245] has performed VLS growth of GaP nanotubes using Ga as catalyst. They have proposed that the formation of GaP nanotubes as follows: phosphous vapor diffused into the liquid Ga droplets to form GaP species within the droplets, when the GaP species reached a supersaturated level, GaP nanotubes precipitated out from the Ga droplets in the manner similar to VLS growth. Wu and co-workers had also found that GaP nanostructure is controlled by the competition of the crystal growth rate at the liquid-solid interface with the diffusion of GaP species in the droplet. High concentrations of GaP species in the droplet would provide adequate ingredients for the nucleation front at the liquid-solid interface via diffusion, hence the growth takes place at the entire liquid-solid junction, giving rise to GaP nanowires. However, when the concentration of GaP species in the droplet is low, inadequate supply of ingredients for the growth at the entire liquid-solid junction is resulted. As such, the growth becomes diffusion-limited and the nucleation front becomes ring-shaped at the liquid-solid interface, giving rise to the growth of GaP nanotubes.

Therefore, it can be deduced that during the growth of Ga_2O_3 nanotubes with Ag catalyst, low concentration of Ga species were present at the liquid-solid junction, giving rise to a diffusion-limited reaction which resulted in the growth of Ga_2O_3 nanotubes. On the contrary, the growth of Ga_2O_3 nanowires using Au and Pd catalysts could be attributed to high concentration of Ga species at the liquid-solid junction.

Since the growth conditions such as laser fluence (1.5 J/cm^2), growth pressure (10 Torr), growth temperature (700°C) and growth duration (15 mins) were consistent for the synthesis of Ga_2O_3 nanostructures with Au, Pd and Ag catalysts, the difference in the concentration of Ga species at the liquid-solid junction may be dependent on the solubility limits of Ga species in the various catalysts. Based on the Ga-Au, Ga-Pd and Ga-Ag phase diagrams, the required concentration of Ga species to form eutectic liquid alloys with Au, Pd and Ag at 700°C, is 19%, 71% and 13% respectively. Notably, the required Ga species to dissolve in Ag catalyst is the lowest as compared to Au and Pd, hence resulting in diffusion limited growth of Ga_2O_3 nanotubes. Similarly, Pei *et al.* has proposed defect-induced growth of hollow, bamboo-shaped SiC nanotubes. However, further investigation is required to fully understand the growth kinetics of metal oxide tubular nanostructures. Wang *et al.* has recently synthesized hollow Ga_2O_3 optical nanowires with single-mode optical waveguiding properties that are promising building blocks for future nano-photonic circuits and devices [246]. In conclusion, the use of different catalyst has successfully demonstrated the synthesis of various Ga_2O_3 nanostructures in this research.

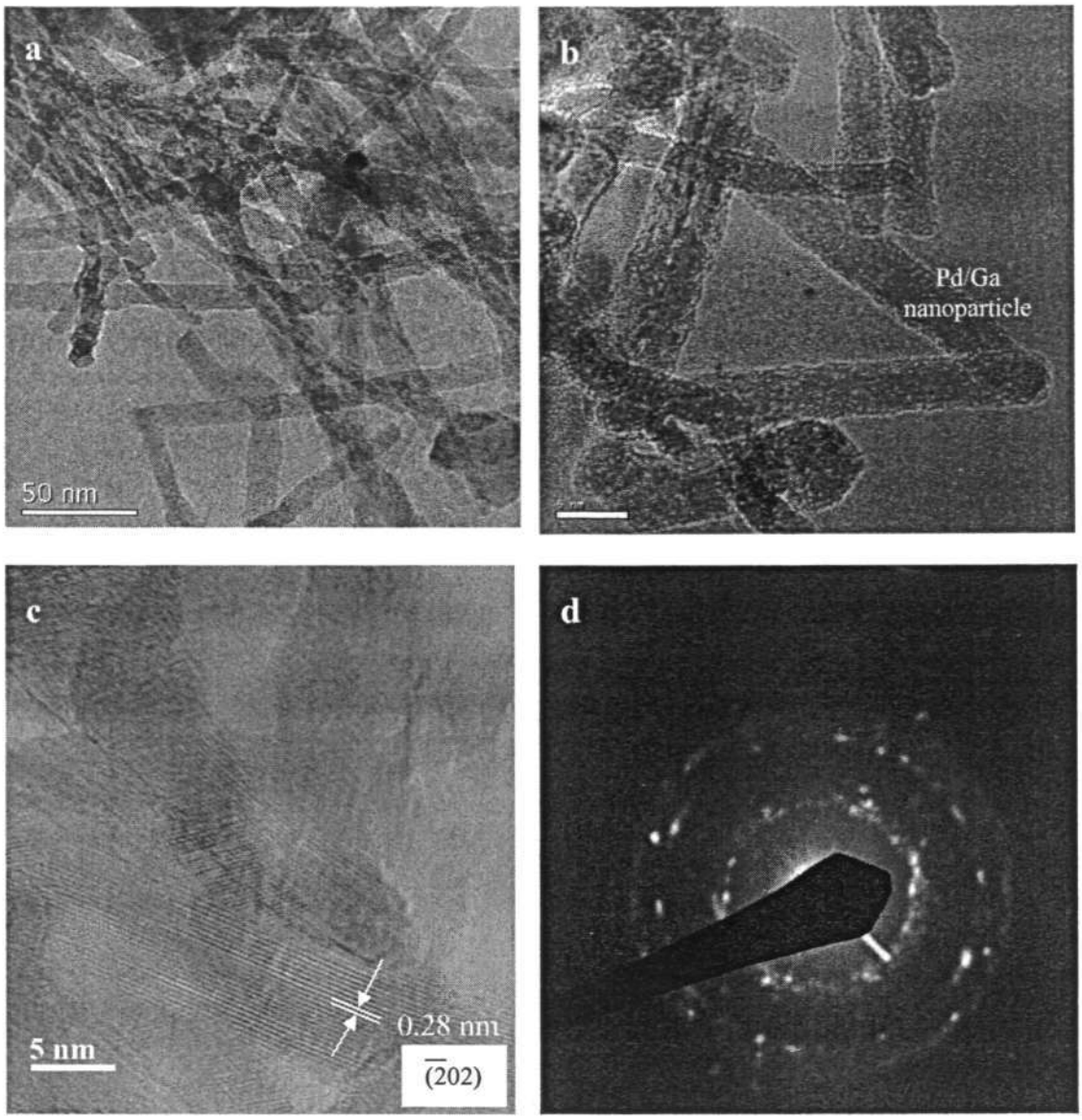

Figure 7-12 (a) TEM image of Pd-catalyzed Ga_2O_3 nanowires synthesized at 700°C, 10 Torr and laser fluence of 1.5 J/cm^2 for 15 mins. (b) Pd-Ga nanoparticle terminates at the end of the nanowires. (c) High-resolution TEM image (selected region shown in a.) of Pd-catalyzed Ga_2O_3 nanowires of the. (d) SAED pattern from the mass of nanowires shown in (a).

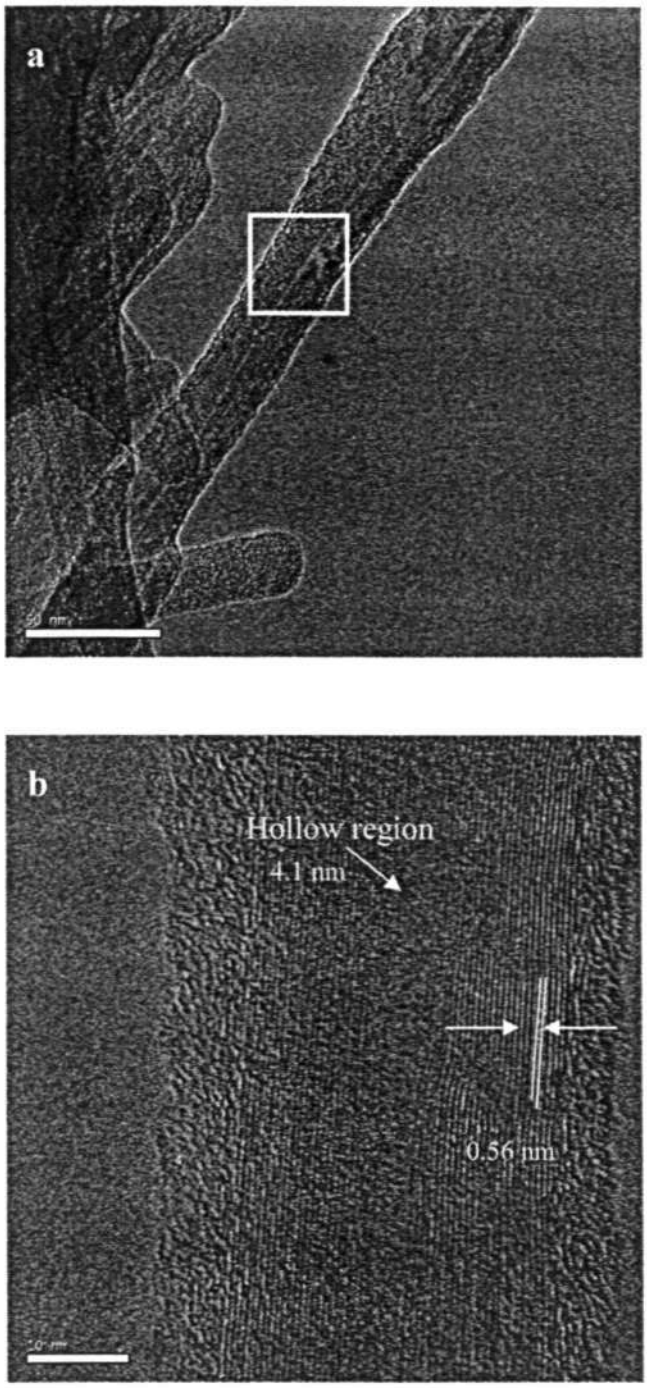

Figure 7-13 (a) TEM image of Ag-catalyzed Ga_2O_3 nanowires synthesized at 700°C, 10 Torr and laser fluence of 1.5 J/cm^2 for 15 mins. (b) High-resolution TEM image (selected region shown in a.) of Ag-catalyzed Ga_2O_3 nanowires.

7.3.6 Photoluminescence of Ga_2O_3 Nanowires

Figure 7-14(a) presents the photoluminescence (PL) spectra of Ga_2O_3 nanowires excited at a wavelength of 266 nm, at room temperature. The effect of growth temperature on the PL properties was studied. The blue emission around 2.65 eV is related to the recombination of an electron on a donor formed by oxygen vacancies or a hole on an acceptor formed by gallium vacancies or gallium-oxygen vacancy pairs [213, 214] while the UV emission around 3.42 ± 0.01 eV is due to the recombination of holes and electrons via a self-trapped exciton [215]. Clearly, the intensity of UV emission is found to increase with higher growth temperature. This may be explained by the fact that the surface-to volume-ratio becomes larger with decreasing size of the nanowires and smaller nanowires have larger non-radiative relaxation rates over the surface states, as explained previously. The non-radiative relaxation process occurring in the surface states will remarkably reduce the PL intensity with smaller size of nanowires. From the above discussions, it is considered that the stronger UV emission of Ga_2O_3 nanowires deposited at 800°C could be due to the larger diameter (~ 60 nm) that reduces non-radiative relaxation rates to enhance the UV emissions. Irrespective of the growth temperature, it is yet again evident that the UV emission of Ga_2O_3 nanowires are significantly stronger than the blue emission, and this is attributed to the fact that more electrons on the donors might be thermally detrapped to the conduction band, and more holes on acceptors might be thermally detrapped to form hole acceptors, recombining to emit a UV photon. Therefore, it is deduced that more holes and electrons in Ga_2O_3 nanowires contribute to emitting a UV photon than a blue photon.

Noticeably, the UV emission peaks exhibit a PL blueshift of up to 35 meV with respect to Ga_2O_3 thin film (3.405 eV) with increasing growth temperature. Greater PL

linewidth broadening at higher growth temperature is also observed in Fig. 7-14. Considering the large surface area-to-volume ratio in nanostructures, the broadening of the blue emission can be ascribed to surface defects. A large quantity of defects and impurities at the surface of Ga_2O_3 nanowires can provide new states which can contribute as visible luminescence centers and broaden the blue emission band [247].

Figure 7-14(b) depicts the photoluminescence of Ga_2O_3 nanowires deposited at 0.01 and 10 Torr in N_2, with the aid of Au catalysts at 700°C. Ga_2O_3 nanowires deposited at 0.01 Torr exhibit blue (2.64 eV) and UV emissions (3.42 eV). Similarly, the Ga_2O_3 nanowires synthesized at 10 Torr reveal emissions peaks at 2.65 eV (blue) and 3.43 eV (UV). However, both blue and UV emissions of Ga_2O_3 nanowires deposited at 10 Torr display high PL intensity. This again can be explained by the fact that Ga_2O_3 nanowires, having a larger diameter and smaller surface-to-volume ratio would significantly reduce non-radiative relaxation rates to greatly enhance its UV emission than thinner nanowires. It is also observed that Ga_2O_3 nanowires deposited at 0.01 Torr and 10 Torr exhibit blueshifts of approximately 15 meV and 25 meV respectively. The average diameter of Ga_2O_3 nanowires (see Fig. 7-14 b) obtained at various growth pressures is larger than the Bohr radius of Ga_2O_3 which is in the range between 2.6 to 5nm. Hence, quantum confinement effect does not work in this regime for Ga_2O_3 nanowires. It is not clear what causes the blueshift of the UV emissions, however it is plausible that strains in the nanowires may shift the UV peak positions to higher energies. Chao *et al.* has reported that strain in nanowires could affect the optical properties as it alters the electronic structure [248]. More work is required to account for the blueshift of the UV peak with larger nanowire size.

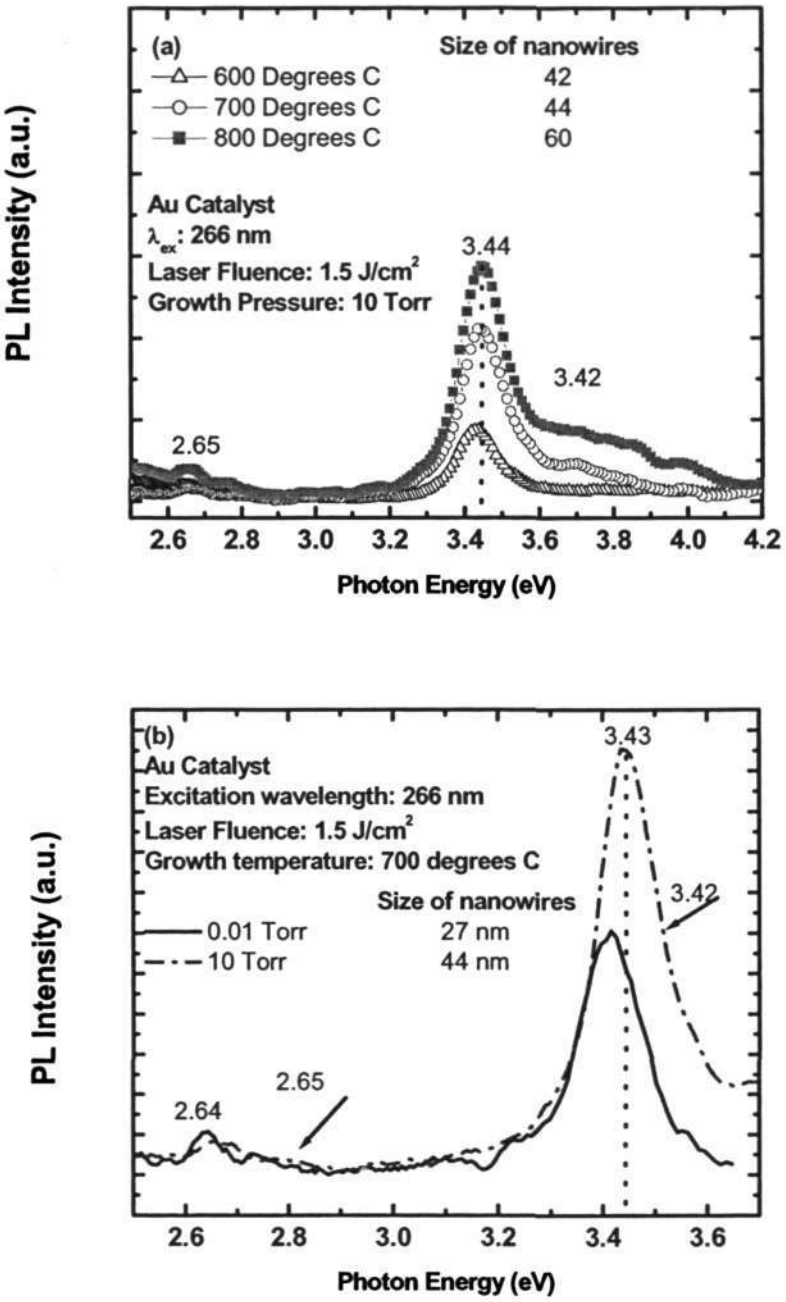

Figure 7-14 Room-temperature photoluminescence spectra of Ga_2O_3 nanowires synthesized at (a) various temperature (600 to 800°C). (b) Room-temperature photoluminescence spectra of Ga_2O_3 nanowires synthesized at (a) 0.01 Torr and (b) 10 Torr at 700 °C in N_2.

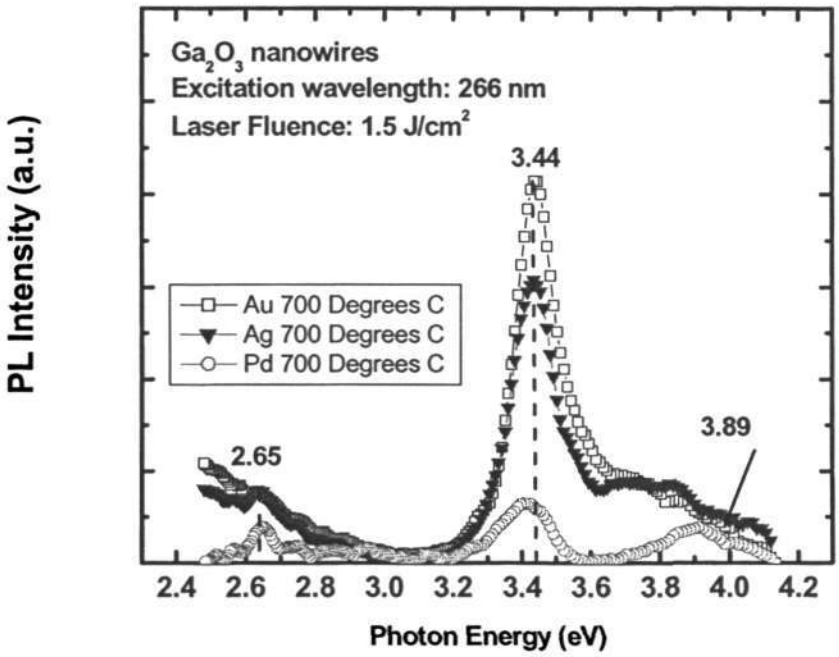

Figure 7-15 Room-temperature photoluminescence spectra of Ga_2O_3 nanowires with Pd, Ag and Au catalysts at 700 °C in N_2.

Figure 7-15 shows the photoluminescence of Ga_2O_3 nanowires deposited with the aid of Au, Ag and Pd catalysts at 700°C. Blue (2.65 eV) and UV (3.43 eV, 3.89eV) emission peaks are observed. Since the synthesizing temperature for the growth of Ga_2O_3 nanowires were kept constant at 700°C, it is apparent that nanowires synthesized with Au catalyst exhibit the highest blue and UV emissions, followed by Ag and Pd. The Au-catalyzed Ga_2O_3 nanowires, having the largest diameter and smallest surface-to-volume ratio would significantly reduce non-radiative relaxation rates to greatly enhance their UV emission, compared to thinner Ag-and Pd-catalyzed nanowires. Furthermore, Ga_2O_3 nanowires synthesized with Ag and Au catalyst exhibit UV emission at 3.43 eV. However, the UV luminescence of Pd synthesized nanowires is centered around 3.41 eV. It is also very interesting to note that a new

emission peak located at 3.89 eV is observed. Since the PL mechanism of Ga_2O_3 is related to defect band emission attributed to Ga vacancies, O vacancies or Ga-O vacancy pairs, the new emission band centered at 3.89 eV may be related to surface or sub-surface states.

7.4 Summary

In conclusion, the synthesis of monoclinic gallium oxide nanowires has been successfully demonstrated for the first time by pulsed laser ablation of GaN, using Au, Pd and Ag as catalysts. The resulting β-Ga_2O_3 nanowires have diameters ranging from 30 to 100 nm and lengths up to several microns. A nanoparticle alloy is typically observed at the end of the β-Ga_2O_3 nanowires, indicating that the growth of the β-Ga_2O_3 nanowires can be attributed to the vapor-solid-liquid mechanism. Due to the smaller Au nano-islands formed before nanowires growth, thinner Ga_2O_3 nanowires were deposited at 600°C, in comparison with those formed at 700°C and 800°C. Hence, the diameter of the initial catalysts on the substrates is determined to have a strong influence on the diameter of the nanowires. In addition, thinner Ga_2O_3 nanowires were synthesized at a low pressure of 0.01 Torr under the same growth temperature of 700°C and the diameter of the nanowires was found to increase with increasing growth pressure. Furthermore, the influence of different metal catalyst on the size, morphology and growth directions of the β-Ga_2O_3 nanowires has been studied and analyzed. Amongst Au, Pd and Ag, Pd-catalyzed β-Ga_2O_3 nanowires had the smallest diameters, while Ag catalysts aided in the formation of nanotubes. A dominant PL emission peak is located at ~ 3.44 eV (UV) for Ga_2O_3 nanowires. It is also apparent that the UV emission peak exhibits a PL blueshift with increasing growth temperature and pressure. The intensity of UV emission was also found to

increase with increasing growth temperature and pressure, which may be attributed to greater reduction of non-relative relaxation rates by larger nanowires. From the PL analysis, it is evident that the PL properties of Ga_2O_3 nanowires are dependent on the growth temperature, growth pressure and type of catalyst employed. All in all, this work demonstrates a fast and effective approach for the low-temperature synthesis of β-Ga_2O_3 nanowires, to fabricate Ga_2O_3 nanodevices such as chemical gas sensors and optoelectronic nanodevices in the future.

CHAPTER 8

Concluding Remarks and Recommendations

The general goal of this project was to develop a novel, fast, effective and low-temperature method for the growth of Ga_2O_3 nanomaterials via photo-dissociation of GaN by pulsed laser ablation technique. A systematic study on the growth and characterization of Ga_2O_3 nanomaterials via the pulsed laser ablation technique is presented in this thesis. The as-deposited and laser-annealed Ga_2O_3 nanoparticles, nanoclusters and nanowires were characterized using various techniques, including Field Emission Scanning Electron Microscopy (FESEM), X-ray diffraction (XRD), Transmission Electron Microscopy, Raman Spectrocopy, X-Ray Photoelectron Spectrocopy (XPS), Absorption and Photoluminescence Spectrocopy (PL). This Chapter summarizes all the results and important findings of this work and recommends some suggestions for future research.

The scope of this work focuses firstly on establishing the growth conditions for Ga_2O_3 nanoparticles, nanoclusters and nanowires deposited in a high vacuum chamber. A pulsed KrF excimer laser operating at a wavelength of 248 nm and was used to ablate the GaN (99.99%) target in N_2 or O_2. The dimensions, structural, crystallinity and optical properties of the as-deposited material were characterized with the abovementioned techniques.

A quick and novel synthesis method has been used to successfully synthesize monoclinic Ga_2O_3 nanoparticles and nanoclusters by pulsed laser ablation of GaN target in N_2 and O_2 ambient, at room temperature. EDX and XPS confirmed that the as-synthesized products were composed of only stoichiometric Ga_2O_3. The FESEM results clearly demonstrated that the diameter of the nanoparticles and degree of

aggregation increased when deposited at higher growth pressures. TEM results revealed that the aggregation of the nanoparticles proceeded one dimensionally to form chain-like nanostructures when synthesized at 10 to 100 Torr. TEM results also indicate that the spherical and ellipsoidal nanoparticles typically have diameters of 8.5 ± 1.75 nm and 6.5 ± 1.34 nm when synthesized at 10 Torr in N_2 and O_2, respectively. Also shown in the XRD results, Ga_2O_3 nanoparticles with higher crystallinity were achieved when deposited at higher growth pressures. It is believed that an increase in the excited species in the laser plume at higher background gas pressure enhances the formation of the monoclinic phase of the Ga_2O_3. Ga_2O_3 nanoparticles deposited at higher laser fluence generated bigger nanoclusters and nanoparticles with higher crystallinity. In addition, the strong Raman peak at 416 cm^{-1} in bulk Ga_2O_3 powder redshifted for samples synthesized in an N_2 ambient. The observed redshift may be related to the creation of oxygen vacancies during the deposition process. On the other hand, the same mid-frequency Raman peak at 416 cm-^{1} in bulk Ga_2O_3 powder blueshifted to 421 cm^{-1} and 426 cm^{-1} for samples synthesized at 1 and 10 Torr in O_2 respectively. The blueshift in phonon frequencies of low dimensional materials are often attributed to the quantum size-confinement effect. Based on these findings, it can be concluded that the size, shape, surface morphologies, degree of aggregation and crystallinity of the Ga_2O_3 nanoparticles and nanoclusters can be controlled accordingly by varying growth conditions such as growth pressure, laser fluence and deposition ambient.

Next, optical properties including photoluminescence and absorption of Ga_2O_3 nanoparticles, were investigated. It was found that Ga_2O_3 nanoparticles deposited at 10 Torr in both N_2 and O_2 exhibit both UV and blue emissions. Ga_2O_3 nanoparticles exhibited a blueshift of 40 meV for the blue emission located at 2.65 eV, as compared

to the PL emission feature of bulk Ga_2O_3 powders. On the other hand, a blueshift up to 35 meV was also observed for UV emission at around 3.41 to 3.44 eV. The PL blueshift is attributed to quantum confinement effects. Furthermore, upon some mathematical calculation, the average diameter of the Ga_2O_3 particles was determined to be 6 nm. The calculated value is in good agreement with the TEM results for the average diameter of Ga_2O_3 nanoparticles synthesized at 10 Torr in O_2 (6.5 nm), thus indicating that the blue shift exhibits weak confinement. In addition, the temperature dependence of the peak position and linewidth for both blue and UV emission bands of Ga_2O_3 nanoclusters and nanoparticles have been studied. The temperature-induced linewidth broadening and shift to longer wavelength were observed for the blue and UV emission bands. Due to electron-phonon coupling, the linewidth of the emission bands increases with higher temperature. Both UV and blue emission intensities also decrease with increasing temperature and this is related to the elimination of shallow traps. Lastly, the effect of deposition gas on the absorption of Ga_2O_3 nanoparticles was also investigated. A significant blueshift of the absorption edge was clearly observed for Ga_2O_3 nanoparticles deposited in both N_2 and O_2. It is proposed that the blueshift in the absorption edge is also related to strong quantum confinement effects.

The influence of KrF excimer laser annealing on the crystallinity and photoluminescence improvement of Ga_2O_3 nanoparticles was investigated. In pulsed KrF excimer annealing, the surface morphology of the as-deposited Ga_2O_3 nanoparticle aggregates transformed to grain-like and film-like morphologies due to coalescence of the nanoparticles and surface melting with increasing laser fluence. However, after laser annealing at the laser fluence of 150 mJ/cm^2, a laser ablation effect was observed, with significant removal of the as-deposited material from the substrate surface. On the other hand, the crystallinity of KrF-excimer-laser-annealed

samples improved when annealed at the laser fluence of 120 mJ/cm^2. Distinct diffraction peaks are observed at (104), ($\bar{2}11$) and (017). However, the sample suffered a loss in crystallinity when laser annealed at 150 mJ/cm^2. This clearly indicates that the as-deposited Ga_2O_3 nanoparticles were damaged after laser annealing at 150 mJ/cm^2. Based on these findings, it is apparent that laser annealing at high fluence values, in the range of 150 mJ/cm^2, led to a laser ablation effect as well as material damage, while in the range of 30 to 100 mJ/cm^2, the photon flux was not sufficient to achieve good crystallinity of Ga_2O_3. In general, the PL intensity and linewidth increase with increasing fluences in KrF-excimer-laser-annealed samples. Linewidth broadening indicates a broad size distribution of nanoparticles which is consistent with larger grain growth at higher laser fluence. A larger redshift in the PL of the KrF excimer laser annealed samples was observed at higher laser fluences. This is attributed to due weaker quantum confinement effect as a result of grain growth. Lastly, the effect of multi-pulse KrF laser annealing on the PL emission of the Ga_2O_3 was also investigated. The PL intensities of the Ga_2O_3 samples are greatly enhanced with increasing pulse number from 1 to 5 but decreases with higher pulse number. When more than 5 laser pulses are employed at a laser fluence of 30 mJ/cm^2 and 50 mJ/cm^2, laser ablation resulted in a reduction in PL intensity. Hence, it is concluded that the crystallinity, blue and UV emission of the Ga_2O_3 nanomaterials can be greatly enhanced or degraded by performing laser annealing at optimum conditions (120 mJ/cm^2 $\leq$ laser fluence$<$ 150 mJ/cm^2 and laser pulses $\leq$ 5) for potential applications as blue or UV optical emitters.

Lastly, the synthesis of monoclinic gallium oxide nanowires has been successfully demonstrated for the first time by pulsed laser ablation of GaN, using Au, Pd and Ag as catalysts. The resulting β-Ga_2O_3 nanowires have diameters ranging from 10 to 100

nm and lengths up to several microns. A nanoparticle alloy is typically observed at the end of the β-Ga_2O_3 nanowires, indicating that the growth of the β-Ga_2O_3 nanowires occurs through the vapor-solid-liquid mechanism. Due to the smaller Au nano-islands formed before nanowires growth, thinner Ga_2O_3 nanowires were grown at 600°C, in comparison with those formed at 700°C and 800°C. Hence, the diameter of the initial catalysts on the substrates is determined to have strong influence on the diameter of the nanowires. In addition, thinner Ga_2O_3 nanowires were synthesized at a low pressure of 0.01 Torr under the same growth temperature of 700°C and the diameter of the nanowires was found to increase with increasing growth pressure. Furthermore, the influence of different metal catalyst on the size, morphology and growth directions of the β-Ga_2O_3 nanowires has been studied and analyzed. Amongst Au, Pd and Ag, Pd-catalyzed β-Ga_2O_3 nanowires displays the smallest diameters, while Ag catalysts aided in the formation of nanotubes. A dominant PL emission peak is located at ~ 3.44 eV (UV) for Ga_2O_3 nanowires. It is also apparent that the UV emission peak exhibits a PL blueshift with increasing growth temperature and pressure. The intensity of UV emission was also found to increase with increasing growth temperature and pressure which may be attributed to greater reduction of non-relative relaxation rates by larger nanowires. From the PL analysis, it is evident that the PL properties of Ga_2O_3 nanowires depended on the growth temperatures, growth pressure and type of catalyst employed. All in all, this work demonstrates a fast and effective approach for the low-temperature synthesis of β-Ga_2O_3 nanowires, to fabricate Ga_2O_3 nanodevices such as chemical gas sensors and optoelectronic nanodevices in the future.

Indeed, these findings pave the way to elucidate other connections between gas-phase chemistry and the properties of Ga_2O_3 nanomaterials, if combined with other relevant experiments. Even though the project's focus is Ga_2O_3, it is clear that the

method developed in this work can be applied to pulsed laser ablation growth of any other multi-component nanomaterials of interest. In conclusion, this study has successfully demonstrated that pulsed laser ablation of GaN in an N_2 or O_2 ambient is a novel and viable route for the growth of Ga_2O_3 nanoparticles, nanoclusters and nanowires for applications in the exciting new field of nanodevices such as UV detectors and gas sensors.

In addition, some recommendations for future research are listed below:-

- **Anodic Aluminium Oxide (AAO) Template Growth of Ga_2O_3 nanowires**

As seen in Chapter 7, since Ga_2O_3 nanowires are deposited randomly across the substrate, it is recommended that an anodic aluminium oxide template be used to exercise greater diameter control on the growth of Ga_2O_3 nanowires. In addition, an AAO template should be effective in directing an upward growth of Ga_2O_3 nanowires from the substrate. With the success in achieving well-aligned carbon nanotubes and GaN nanowires, it will be worthwhile to combine laser synthesis and AAO template to control and direct the growth of Ga_2O_3 nanowires.

- **Time-resolved Photoluminescence measurements**

A study of the time-resolved photoluminescence of the Ga_2O_3 nanoparticles, nanoclusters and nanowires is recommended for future research as it can provide useful information on the change in carrier lifetime in Ga_2O_3 nanomaterials with different growth conditions established in this work.

- **Fabrication of Gas Sensors**

Due to time constraints and unforeseen circumstances, it is a pity that fabrication of Ga_2O_3 gas sensors could not be performed. The benefit of nanowires is the enhanced surface to volume ratio which provides extreme sensitivity to changes in surface conditions and this could be very useful in sensor applications. So far, Ga_2O_3 has been proven to be an effective gas sensor material for detecting gases like oxygen, hydrogen, ethane and CO.

AUTHOR'S PUBLICATIONS

1. S. Yuan, H. M. Lam, S. G. Ma, *Handbook of Semiconductor Nanostructures and Nanodevices*, Chapter 37 (2005).

2. H. M. Lam, M. H. Hong, S. Yuan and T. C. Chong, *Appl. Phys. A*, 79, 2099-2102 (2004).

3. H. M. Lam, T. S. Ong, C. L. Gan, *Appl Phys. A* (submitted).

4. G. X. Chen, M. H. Hong, T. S. Ong, H. M. Lam, W. Z. Chen, H. I. Elim, W. Ji and T. C. Chong, *Carbon*, 42 (12-13), 2735-2737 (2004).

5. H. M. Lam, M. H. Hong, C. L. Gan and T. C. Chong, *Proceedings of the 5th International Symposium on Laser Precision Microfabrication*, 62-66 (2004).

6. G. X. Chen, M. H. Hong, Z. B. Wang, H. I. Elim, W. Z. Chen, H. M. Lam, Proceedings of the 5th International Symposium on Laser Precision Microfabrication 71-76 (2004).

7. H. M. Lam, S. Yuan, M. H. Hong, D. J. Wu and T. C. Chong, *International Conference on Materials for Advanced Technologies* (2003) – Poster Presentation

8. H. M. Lam, M. H. Hong, S. Yuan and T. C. Chong, *3rd International Symposium on Laser Precision Microfabrication*, 4830, 114-118 (2002).

9. M. H. Hong, B. Luk'yanchuk, H. M. Lam, Z. B. Wang, S.M. Huang, D.J. Wu and T.C. Chong, *The First European Femtosecond Laser Applications in Materials Science* (2002) - Invited talk

References

1. J. M. Villas-Boas, S. E. Ulloa, A. O. Govorov, Physica E **34**, 333-335 (2006).

2. C. H. Lu, L. M. Qi, J. H. Yang, L. Tang, D. Y. Zhang, J. M. Ma, Chemical Commun. **33**, 3551 (2006).

3. Y. L. Lai, C. P. Liu, Y. H. Lin, T. H. Hseuh, R. M. Lin, D. Y. Lyu, Z. X. Peng, T. Y. Lin, Nanotechnology **17**, 3734 (2006).

4. M. R. Maschmann, A. D. Franklin, P. B. Amama, D. N. Zakharov, E. A. Stach, T. D. Sands, T. S. Fisher, Nanotechnology **17**, 3925 (2006).

5. G. Q. Ding, W. Z. Shen, M. J. Zheng, Z. B. Zhou, Appl. Phys. Lett. **89**, 063113 (2006).

6. D. Y. Jeon, K. H. Kim, S. J. Park, J. H. Huh, H. Y. Kim, C. Y. Yim, G. T. Kim, Appl. Phys. Lett. **89**, 023108 (2006).

7. B. Mandl. J. Stangl, T. Martensson, A. Mikkelsen, J. Eriksson, L. S. Karlsson, G. Bauer, L. Samuelson, W. Seifert, Nano Lett. **6**, 1817 (2006).

8. Y. R. Uhm, W. W. Kim, C. K. Rhee, Physica Status Solidi A **201**, 1934 (2004).

9. G. M. Hao, Y. N. Lu, W. R. Xue Y. W. Zeng, Rare Metal Mater. and Eng. **32**, 624 Suppl. 1 (2003).

10. T. Miyao, K. Minoshima, S. Naito, J. of Mater. Chem. **15**, 2268 (2005)

11.S. Lee, D. W. Shin, W. M. Kim, B. K. Cheong, T. S. Lee, K. S. Lee, S. Cho, Thin Solid Films **514**, 296 (2006).

12. G. J. Xian, Z. Zhang, K, Friedrich, J. of App. Polymer Sci. **101**, 1678 (2006).

13. C. M. Chen, Y. M. Dai, J. G. Huang, J. M. Jehng, Carbon **44**, 1808 (2006).

14. C. Li, D. H. Zhang, S. Han, X. L. Liu, T. Tang, C. W. Zhou, Adv. Mater. **15**, 143 (2003).

15. S. D. Hersee, X. Y. Sun, X. Wang, Nano Lett. **6**, 1808 (2006).

16. Y. D. Wang, K, Y. Zang, S. J. Chua, S. Tripathy, P. Chen C. G. Fonstad, App. Phys. Lett. **87**, 251915 (2005).

17. T. Ghoshal, S, Kar, S. Chaudhuri, J. of Cryst. Growth **293**, 438-446 (2006).

18. V. M. Goldschmidt, T. Barth, G, Lunde, Skr. Norske Ved. Akad. Oslo Mater. **5**, 1 (1925).

19. W. A. Roth, G. Becker, Z. Phys. Chem. **A159**, 1 (1932).

20. L. M. Foster, H. C. Stumpf, J. Am. Chem. Soc. **73**, 1590 (1951).

21. R. Roy, V. G. Hill, E. F. Osborn, J. Am. Chem. Soc. **74**, 719 (1952).

22. R. Roy, V. G. Hill, E. F. Osborn, Ind. Eng. Chem. **45**, 819 (1953).

23. S. Geller, J. Chem. Phys. **33**, 676 (1960).

24. E. G. Villora, K. Shimamura, Y. Yoshikawa, K. Aoki, N. Ichinose, J. Cryst. Growth **270**, 420 (2004).

25. G. Katz, R. Roy, J. Am. Chem. Soc. **49**, 168 (1966).

26. Z. R. Dai, Z. W. Pan, Z. L. Wang, J. Phys. Chem. B **106**, 902 (2002).

27. G. S. Park, W. B. Choi, J. M. Kim, Y. C. Choi, Y. H. Lee, C. B. Lim, J. Cryst. Growth **220**, 494 (2000).

28. M. Zinkevich, F. Aldinger, J. Am. Chem. Soc. **87**, 683 (2004).

29. M. Passlack, E. F. Schubert, W. S. Hobson, M. Hong, N. Moriya, S. N. G. Chu, K. Konstadinidis, J. P. Mannaerts, M. L. Schnoes, G. J. Zydzik, J. Appl. Phys. **77**, 686 (1995).

30. M. R. Lorentz, J. F. Woods, R. J. Gambino, J. Phys. Chem. Solids **28**, 403 (1967).

31. T. Harwig, G. J. Dirksen, Solid State Commun. **18**, 1223 (1976).

32. L. Binet, D. Gourier, J. Phys. Chem. Solids **59**, 1241 (1998).

33. N. Ueda, H. Hosono, R. Waseda, H. Kawazoe, Appl. Phys. Lett. **70**, 3561 (1997).

34. E. G. Villora, T. Atou, T. Sekiguchi, T. Sugawara, M. Kikuchi, T. Fukada, Solid State Commun. **120**, 455 (2001).

35. A. B. Chase, J. Am. Ceram. Soc. **47**, 470 (1964).

36. M. Fleischer, H. Meixner, J. Vac. Sci. Technol. A **17**, 1866 (1999).

37. Y. Li, A. Trinchi, W. Wlodarski, K. Galatsis, K. Kalantarzadeh, Sens. Actuators, B **93**, 431 (2003).

38. A. C. Lang, M. Fleischer, H. Meixner, Sens. Actuators B **66**, 80 (2000).

39. P. P. Macri, S. Enzo, G. Sberveglieri, S. Groppelli, C. Perego, Appl. Surf. Sci. **65/66,** 277 (1993).

40. M. Ogita, K. Higo, Y. Nakanishi, Y. Hatanaka, Appl. Surf. Sci. **175-176**, 721 (2000).

41. M. Orita, H. Hiramatsu, H. Ohta, M. Hirano, H. Hosono, Thin Solid Films **411**, 134 (2002).

42. M. Passlack, M. Hong, J.P. Mannaerts, Appl. Phys. Lett. **68**, 1099 (1996).

43. M. Valet, D.M. Hoffman, Chem. Mater. **13**, 2135 (2001).

44. C. Huang, A. Ludviksson, R.M. Martin, Surf. Sci. **265,** 314 (1992).

45. H. W. Kim, N. H. Kim, Mater. Sci. and Eng. B **110**, 34 (2004).

46. H. W. Kim, N. H. Kim, C. Lee British Ceramic Transactions **103**, 187 (2004).

47. Z. Ji, J. Du, J. Fan, W. Wang, Optical Materials **28**, 415 (2006).

48. T. Xiao, A.H. Kital, G. Liu, A. Nakua, Appl. Phys. Lett. **72** 3356 (1998).

49. M. Ogita, H. Ohta, M. Hirano, H. Hosono, Appl. Phys. Lett. **77**, 4166 (2000).

50. M. Rebein, W. Henrion, M. Hong, J. P. Mannaerts, M. Fleischer, Appl. Phys. Lett. **81**, 250 (2002).

51. M. Bartic, Y. Toyoda, C. L. Baban, M. Ogita, Jap. J. of Appl. Phys. Part 1, **45**, 5186 (2006).

52. M. Fleischer and H. Meixner, Sens. Actuators B **6**, 257 (1992).

53. F. Reti, M. Fleischer, H. Meixner , J. Giber, Sens. Actuators B **18–19**, 573 (1994).

54. M. Fleischer and H. Meixner, Sens. Actuators B **52**, 179 (1998).

55. M. Fleischer and H. Meixner, Sens. Actuators B **4**, 437 (1991).

56. M. Ogita, N. Saika, Y. Nakanishi and Y. Hatanaka, Appl. Surf. Sci. **142**, 188 (1999).

57. K. Matsuzaki, H. Yanagi, T. Kamiya, H. Hiramatsu, K. Nomura, M. Hirano, Hideo Hosono, Appl. Phys. Lett. **88**, 092106 (2006).

58. F. Zhu, Z. X. Yang, W. M. Zhou, Y. F. Zhang, Physica Status Solidi A **203**, 2024 (2006).

59. F. Zhu, Z. X. Yang, W. M. Zhou, Y. F. Zhang, Physica E **33**, 151 (2006).

60. P. Feng, J. Y. Zhang, Q. H. Li, T. H. Wang, Appl. Phys. Lett. **88**, 153107 (2006).

61. M. Mitome, S. Kohiki, K. Hori, M. Fukuta, Y. Bando, J. Cryst. Growth **286**, 240 (2006).

62. S. Ohira, T. Sugawara, K. Nakajima, T. Shishido, J. Alloys and Compounds **402**, 204, (2005).

63. N. H. Kim, H. W. Kim, App. Surf. Sci. **242**, 29 (2005).

64. N. H. Kim, H. W. Kim, Adv. In Appl. Ceramics **105**, 84 (2006).

65. N. H. Kim, H. W. Kim, C. Seoul, C. Lee, Mater. Sci. and Eng. B **111**, 131 (2004).

66. K. Suzuki, Y. Kuroki, T. Okamoto, M. Takata, Electroceramics in Jap. VIII **301**, 181 (2005).

67. J. Zhang, Z. G. Liu, C. K. Lin, J. Lin , J. Cryst. Growth **280**, 99 (2005).

68. J. Q. Hu, Q. Li, X. M. Meng, C. S. Lee, S. T. Lee, J. Phys. Chem. B **106**, 9536 (2002).

69. N. H. Kim, H. W. Kim, Appl. Phys. A **81**, 763 (2005).

70. J. Zhang, F. H. Jiang, Y. D. Yang, J. P. Li, J. Phys. Chem. B **109**, 13143 (2005).

71. H. W. Kim, N. H. Kim, C. Lee, J. of the Korean Physical Soc. **47**, S539 (2005).

72. N. H. Kim, H. W. Kim, Appl. Phys. A **80**, 537 (2005).

73. J. S. Lee, K. Park, S. Nahm, S. W. Kim, S. Kim, J. Cryst. Growth **244**, 287 (2002).

74. C. F. Klingshirn, *Semiconductor Optics*, Springer (1995).

75. P. F. Trwoga, A. J. Kenyon, C. W. Pitt, J. Appl. Phys. **83**, 3789 (1998)

76. P. Nguyen, Masters of Science Thesis, San José State University (2003).

77. A. I. Ekimov, A. L. Efros, M. G. Ivanov, A. A. Onushcenko, S. K. Shummilov, Solid State Communications **69**, 565 (1989).

78. A. I. Ekimov, A. L. Efros, A. A. Onushcenko Solid State Communications **56**, 921(1985).

79. R. Rossetti, S. M. Beck, L. E. Brus, J. Am. Chem. Soc. **104**, 7322 (1982).

80. A. P. Alivisatos, J. Phys. Chem. **100**, 13226 (1996).

81. J. Zuo, C. Xu, X. Liu, X. Wang, C. G. Wang, Y. Hu, Y. Qian, J. App. Phys. **75**, 1835 (1994).

82. J. Z. Jortner, Phys. D. **24**, 247 (1992).

83. A. Henglein, Chem. Rev. **89**, 1861 (1989).

84. W. P. Kirk. M. A. Rheed, *Nanostructures and Mesoscopic Systems*, Academic Press: Boston (1992).

85. T. Ogawa, Y. Kanemitsu, *Optical Properties of Low Dimensional Materials*, World Scientific: Singapore, New Jersey, London and Hong King (1995).

86. U. Woggen, *Optical Properties of Semiconductor Quantum Dots*: Springer: Berlin (1997).

87. P. V. Kamat, Chem. Rev. **93**, 267 (1993)

88. M. R. Hoffmann, S. T. Martin, W. Choi, D. W. Bahnemann, Chem. Rev. **95**, 69 (1995).

89. M. Natasi, D. M. Parkin, H. Gleiter, *Mechanical Properties and Deformation Behavior of Materials Having Ultra-fine Microstructures,* Kluwer: Dordrecht and Boston (1993).

90. H. Matsumoto, T. Sakata, H. Mori, H. Yoneyama, J. Phys. Chem. **100**, 13781 (1996).

91. A. P. Alivisatos, Science **271**, 933 (1996).

92. R. L. Holtz, V. Provenzano, M. A. Imam, Nanostruct. Materials **7**, 259 (1996).

93. A. C. Zettlemayer, *Nucleation*, Marcel Dekker: New York (1969).

94. F. F. Abraham, *Homogeneous Nucleation Theory*, Academic Press: New York and London (1974).

95. S. Iijima, Nature **354**, 56 (1991).

96. R. Martel, T. Schmidt, H. R. Shea, T. Hertel, P. Avouris, Appl. Phys. Lett. **73**, 2447 (1998).

97. J. C. Johnson, H. J. Choi, K. P. Knutsen, R. D. Schaller, P. Yang and R. J. Saykally, Nature Mater. **1**, 106 (2002).

98. R. S. Wagner and W. C. Ellis, Appl. Phys. Lett. **4**, 89 (1964).

99. Y. Wu and P. Yang, J. Am. Chem. Soc. **123**, 3165 (2001).

100. M. H. Huang, Y. Wu, H. Feick, N. Tran, E. Weber, P. Yang, Adv. Mater. **13**, 113 (2001).

101. Y. C. Choi, W. S. Kim, Y. S. Park, S. M. Lee, D. J. Bae, Y. H. Lee, G. S. Park, W. B. Choi, N. S. Lee, J. M. Kim, Adv. Mater. **12**, 746 (2000).

102. W. C. Liu, C. L. Mak, K. H. Wong, D. Y. Wangm H. L. W. Chan, J. of Appl. Phys. **100**, 033507 (2006).

103. J. W. Kim, H. S. Kang, J. H. Kim, S. Y. Lee, J. K. Lee, M. Nastasi, J. of Appl. Phys **100**, 033701 (2006).

104. M. Liu, B. Y. Man, C. S. Xue, H. Z. Zhuang, H. C. Zhu, X. Q. Wei, C. S. Chen, Appl. Phys. A **85**, 83 (2006).

105. X. P. Zhu, T. Suzuki, T. Nakayama, T. Suematsu, W. H. Jiang, K. Niihara, Chem. Phys. Lett. **427**, 127 (2006).

106. Y. J. Choi, I. S. Hwang, J. H. Park, S. Nahm, J. G. Park, Nanotechnology **17**, 3775 (2006)

107. D. Grojo, M. BoyoMo-Onana, A. Cros, P. Delaporte, Appl. Surf. Sci. **252**, 4786 (2006).

108. R. Bohme, S. Pissadakis, D. Ruthe, K. Zimmer, Appl. Phys. A **85**, 75 (2006).

109. P. Tejedor, P. S. Domínguez, Appl. Surf. Sci. **89**, 271 (1995).

110. S. A. Bakhramov, S. D. Paiziev, Optics and Spectroscopy **100**, 400 (2006).

111. M. D. Shirk, P. A. Molian, J. Laser. Applications **10**, 18 (1998).

112. T. Götz, M. Stuke, App. Phys. A **64**, 539 (1997).

113. J. C. Miller, R. F. Haglund, *Laser Ablation and Desorption*, Academic Press, 225 (1998).

114. J. C. Miller, *Laser Ablation*, Berlin: Springer, 167 (1994).

115. J. C. Miller, *Laser Ablation*, Berlin: Springer, 168 (1994).

116. Chief Editor, B. Thassdeus, Editors, O. Hiroaki, P. R. Subramanian, L. Kacprzak, '*Binary Alloy Phase Diagram*', ASM International, Materials Park, Ohio (1990).

117. C. J. Phys. F: Met. Phys. 2, 441 (1972).

118. T. Castro, R. Reifenberger, E. Choi, R. P. Andres, Phys. Rev. B 42, 8548 (1990).

119. A. N. Goldstein, C. M. Echer, A. P. Alivisatos, Science 256, 1425 (1992).
120. K. K. Nanda, F. E. Kruis, H. Fissan, Phys. Rev. Lett. 89, 256103 (2002).

121. X. Duan, C. M. Lieber, J. Am. Chem. Soc. **122**, 188 (2000).

122. H. W. Seo, S. Y. Bae, J. Park, H. Yang, K. S. Park and S. Kim, J. Chem. Phys. **116**, 9492 (2002).

123. Q. Gu, H. Dang, J. Cao, J. Zhao, S. Fan, Appl. Phys. Lett. **76**, 3020 (2000).

124. D. Zhang, D. N. McIlroy, Y. Geng, M. G. Norton, J. Mater. Sci. Lett. **18**, 349 (1999).

125. D. N. McIlroy, D. Zhang, Y. Kranov, M. G. Norton, App. Phys. Lett. **79**, 1540 (2001).

126. C. C. Tang, S. S. Fan, H. Y. Dang, P. Li, Y. M. Liu, Appl. Phys. Lett. **77**, 1961 (2000).

127. Y. C. Kong, D. P. Yu, B. Zhang, W. Fang, S. Q. Feng, App. Phys. Lett. **78**, 407 (2001).

128. D. N. McIlroy, D. Zhang, Y. Kranov, H. Han, A. Alkhateeb, M. G. Norton, Mater. Res. Sym. Proc. **739**, 164 (2003).

129. K. A. Jackson and R. S. Wagner, J. Appl. Phys. **36**, 2132 (1965).

130. M. S. Gudiksen, J. Wang, C. M. Lieber, J. Phys. Chem. B **105**, 4062 (2001).

131. C. C. Chen, C. C. Yeh, Adv. Mater. **12**, 738 (2000).

132. C. C. Chen, C. C. Yeh, C. H. Chen, M. Y. Yu, H. L. Liu, J. J. Wu, K. H. Chen, L. C. Chen, J. Y. Peng, Y. F. Chen, J. Am. Chem. Soc. **123**, 2791 (2001).

133. M. H. Huang, Y. Wu, H. Feick, N. Tran, E. Weber, P. Yang, Adv. Mater. **12**, 113 (2001).

134. Y. Wu, P. Yang, Chem. Mater. **12**, 605 (2000).

135. S. –L. Zhang, B. -F. Zhu, F. Huang, Y. Yan, E. –Y. Shang, S. Fan, W. Han, Solid State Commun. **111**, 647 (1999).

136. W. Eberhardt, Surf. Sci. **500**, 242 (2002).

137. K. H. Meiwes-Broer, *Metal Clusters at Surfaces: Structure, Quantum Properties, Physical Chemistry*, Springer-Verlag: Berlin (2000).

138. C. T. Campbell, Surf. Sci. Rep. **27**, 1 (1997).

139. J. Eckert, J. C. Holzer, C. E. Krill, W. L. Johnson, J. Mater. Res. **7**, 1751 (1992).

140. A. Huczko, Appl. Phys. A **70**, 365 (2000).

141. C. J. Brinker, G. W. Scherer, *Sol-Gel Science*, Academic Press: Boston (1990).

142. H. Hahn, Nanostruct. Mater. **9**, 3 (1997).

143. D. H. Lowndes, D. B. Geohegan, A. A. Puretzky, D. Norton, C. M. Rouleau, Science **273**, 898 (1996).

144. D. B. Chrisey, G. K. Hubler, *Pulsed Laser Deposition of Thin Film*, Wiley: New York (1994).

145. A. M. Serventi, M. A. El Khakani, R. G. Saint-Jacques, D. G. Rickerby, J. Mater. Res. **16**, 2336 (2001).

146. T. Yoshida, Y. Yamada, J. Appl. Phys. **83**, 5427 (1998).

147. R. Dolbec, E. Irissou, M. Chaker, D. Guay, F. Rosei, M. A. Khakani, Phys. Rev. B **70**, 201406 (2004).

148. K. –M. Lee, D. –J, H. Ahn, Mater. Lett. **58**, 3122 (2004).

149. L. Fu, Z. Liu, Y. Liu, B. Han, J. Wang, P. Hu, L. Cao, D. Zhu, J. Phys. Chem. B **108**, 13074 (2004).

150. H. C. Le, R. W. Dreyfus, W. Marine, M. Sentis, I. A. Movtchan, Appl. Surf. Sci. **96/98**, 164 (1996).

151. S. K. Friedlander, *Smoke Dust and Haze, Fundamentals of Aerosol Dynamics*, Oxford University Press (2000).

152. T. Nagata, Y. –Z. Yoo, P. Ahmet, T. Chikyow, Jap. J. of Appl. Phys. **44**, 7896 (2005).

153. Y. Nakata, J. Muramoto, T. Okada, M. Maeda, J. Appl. Phys. **91**, 1640 (2002).

154. B. Luk'yanchuk and W. Marine, Appl. Surf. Sci. **154-155**, 314 (2000).

155. International Centre for Diffraction Data, Powder Diffraction File No. 41-1103.

156. S. M. Oh, J. G. Gong, D. W. Park, J. Chem, Eng. Jpn. **34**, 283 (2001).

157. M. Capitelli, F. Capitelli, A. Eleskii, Spectrochim. Acta B **55**, 559 (2000).

158.R. Rao, A. M. Rao, B. Xu, J. Dong, S. Sharma, M. K. Sunkara, J. Appl. Phys. **98**, 094312 (2005).

159. D. Dohy, G. Lucazeau, A. Revcolevschi, J. of Solid State Chemistry **45**, 180 (1982).

160. S. Geller, J. Chem. Phys. **33**, 676 (1960).

161. S. L. Zhang, B. F. Zhu, F. Huang, Y. Yan, E. Shang, S. Fan, W. Han, Solid State Commun. **111**, 647 (1999).

162. L. Dai, X. L. Chen, X. N. Zhang, A. Z. Lin, T. Zhou, B. Q. Hu, Z. Zhang, J. Appl. Phys. **92**, 1062 (2002).

163. T. C. Damen, S. P. S. Porto, B. Tell, Phys. Rev. **142**, 570 (1966).

164. I. H. Campbell, P. M. Fauchet, Solid State Commun. **58**, 739 (1986).

165. H. Shen, F. H. Pollak, Appl. Phys. Lett. **45**, 692 (1984).

166. T. Yoshida, S. Takeyama, Y. Yamada, K. Mutoh, Appl. Phys. Lett. **68**, 1772 (1996).

167. T. Sasaki, S. Terauchi, N. Koshizaki, H. Umehara, AIChE J. **43**, 2636 (1997).

168. F. Di Fonzo, A. Bailini, V. Russo, A. Baserga, D. Cattaneo, M. G. Beghi, P. M. Ossi, C. S. Casari, A. Li Bassi, C. E. Bottani, Catalysis Today **116**, 69 (2006).

169. S. H. Shim, K. B. Shim, J. –W. Yoon, Y. Shimizu, T. Sasaki, N. Koshizaki, Thin Solid Films **472**, 11 (2005).

170. M.Q. Chu, X.Y. Shen, G.J. Liu, Nanotechnology **17**, 444 (2006).

171. Q. Cao, X.Y. Li, J. of Adv. Mater. **37**, 77-80 (2005).

172. T. W. Kim, S.M. Abrarov, S.U. Yuldashev, Y.H. Kwon, T.W. Kang, J. of Crys. Growth **286,** 300-305 (2006).

173. X. Xiang, C.B. Cao, Y.J. Xu, H.S. Zhu, Nanotechnology **17**, 30-34 (2006).

174. M.H.M. van Weert, O. Wunnicke, A.L. Roest, T.J. Eijkemans, A. Yu Silov, J.E.M. Haverkort, G.W. 't Hooft, E.P.A.M. Bakkers, App. Phys. Lett. **88**, 043109 (2006)

175. A.P. Alivisatos, J. Phys. Chem. **100**, 13226 (1996).

176. A.P. Alivisatos, Science **271**, 933 (1996).

177. H. S. Zhou, I. Honma, K. H. Kim, H. Komiyama, H. Sasabe, J. W. Haus, Surf. Rev. and Lett. **3**, 133 (1996).

178. W. I. Park, J. Yoo, D. W. Kim, G.C. Yi, M. Kim, J. of Phys. Chem. B **110**, 1516 (2006).

179. M. Bruno, M. Palummo, A. Marini, R. Del Sole, V. Olevano, A. N. Kholod, S. Ossicini, Phys. Rev. B **72**, 153310 (2005).

180. T. Harwing, F. Kellendouk, J. Solid State Chem. **24**, 255 (1978).

181. J. Zhang, F. Jiang, Chem. Phys. **289**, 243 (2003).

182. V. I. Vasil'tasiv, Y. M. Zakharko, Y. I. Prim, Ukr. Fiz. Zh. **33**, 1320 (1988).

183. L. Binet, D. Gourier, J. Phys. Chem. Solids, **59**, 1241-1249 (1998).

184. J. Zhang, F. Jiang, L. Zhang, Phys. Lett. A **322**, 363 (2004).

185. A.D. Yoffe, Advances in Physics, **42**, 173 (1993).

186. Hamberg and C.G. Granqvist, J. App. Phys. **60**, R123 (1986).

187. H. Zhou, W. Cai, L. Zhang, Appl. Phys. Lett. **75**, 495 (1999).

188. W. Q. Han, P. Kohler-Redlich, F. Ernst, M. Rühle: Solid State, Commun. **115**, 527 (2000).

189. Y.P. Varshni, Physica **34**, 149 (1967).

190. V.I. Vasil'tasiv, Y. M. Zakharko, Sov. Phys. Solid State **25**, 72 (1983).

191. C. C. Tang, S. S. Fan, H. Y. Dang, P. Li, Y. M. Liu, Appl. Phys. Lett. **77**, 1961 (2000).

192. T. Xiao, A.H. Kital, G. Liu, A. Nakua, Appl. Phys. Lett. **72** 3356 (1998).

193. K. W. Mah, E. McGlynn, J. G. Lunney, J. P. Mosnier, D. O. Mahony, M. O. Henry, J. Cryst. Growth **222**, 497 (2001).

194. M. Orita, H. Ohta, M.Hirano, H. Meixner, Sens. Actuators B **26/27**, 85 (1995).

195. I. Ozerov, A. V. Bulgakov, D. K. Nelson, R. Castell, W. Marine, Appl. Surf. Sci. **247**, 1 (2005).

196. Y. F.Zhang, Y. H. Tang, C. S.Lee, I. Bello, S. T. Lee: Phys. Rev. **61B**, 4518 (1999).

197. J. I. Pankove, *Optical Processes in Semiconductors*, Dover: New York (1971) 201.

198. N. Ueda, H. Hosono, R. Waseda, H. Kawazoe, Appl. Phys. Lett. **71**, 933 (1997).

199. G. Allan, C. Delerue, M. Lannoo, Phys. Rev. Lett. **78**, 3161 (1997).

200. Y. Ohmura, T. Shigematsu, R. Nakayama, Physica Status Solidi A-Applied Research, **56**, 225 (1979).

201. K. R. Bradley, T. E. Luke, R. L. Hengehold, P. M. Hemenger, Y. S. Park, Bulletin of the American Physical Society **25**, 462 (1980).

202. I. Ozerov, M. Arab, VI Safarov, W. Marine, S. Giorgio, M. Sentis, L. Nanai, Applied Surf. Sci. **226**, 242 (2004).

203. D. Bauerle, *Laser Processing and Chemistry, 3rd edition*, Springer-Verlag: New York Chapter 23 (1996).

204. S. Whelan, A. La Magna, V. Privitera, G. Mannino, M. Italia, C. Bongiorno, G. Fortunato, L. Mariucci, Physical Rev. B **67**, 075201 (2003).

205. R.T Young, J. Narayan, W.H. Christie, G.A. Van der Leeden, J. I. Levatter, L. J. Cheng, Solid State Technol. **26**, 183 (1983).

206. T. Sameshima and S. Usui, J,App. Phys. **70**, 1281 (1991).

207. D.H. Lowndes, Phys. Rev. Lett. **48**, 267 (1982).

208. N. Paulter, P.S. Peercy, Phys. Rev. Lett. **48**, 33 (1982).

209. B. C. Larson, C.W. White, T.S. Noggle, D. Mills, Phys. Rev. Lett. **48**, 337 (1982).

210. D.J. Kim, S.E. Park, H.J. Kim, J. K. Ryu, B. O, S.S. Pak, Jpn, J. Appl. Phys. **42**, 7349 (2003).

211. J. M. Poate, *Laser Annealing of Semiconductors*, Academic press: New York, Chapter 4 (1982).

212. G. A. Battison, R. Gerbasi, M. Porchia, Thin Solid Films **279**, 115 (1996).

213. T. Harwing, F. Kellendonk, J. Solid State Chem. **24**, 255 (1978).

214. V. I. Vasilstiv, Y. M. Zakharko, Y. I. Prim, Ukr. Fiz. Zh. **33**, 1320 (1998).

215. X. C. Wu, W. H. Song, W. D. Huang, M. H. Pu, B. Zhao, Y. P. Sun, J. J. Du, Chem. Phys. Lett. **328**, 5 (2000).

216. I. Ozerov, A. V. Bulgakov, D. K. Nelson, R. Castell, W. Marine, Appl. Surf. Sci. **247**, 1 (2005).

217. H. W. Kim, N. H. Kim, C. Lee, British Ceramic Transactions **103**, 187 (2004).

218. K. B. McGuire, *Synthesis and Characterization of Nanomaterials: Nanotubes, Nanowires and Nanobelts*, PhD Thesis, Clemson University (2003).

219. L. Bergman, X. B. Chen, J. Feldmeier, Appl. Phys. Lett. **83**, 764 (2003).

220. L. Vina, S. Logothetidis, M. Cardona, Phys. Rev. B **30**, 1979 (1984).

221. Y. G. Cao, X. L. Chen, J. Y. Li, Y. C. Lan, J. K. Liang, App. Phys. A **71**, 229 (2000).

222. R. Martel, T. Schmidt, H. R. Shea, T. Hertel, P. Avouris, Appl. Phys. Lett. **73**, 2447 (1998).

223. J. C. Johnson, H. J. Choi, K. P. Knutsen, R. D. Schaller, P. Yang and R. J. Saykally, Nature Mater. **1**, 106 (2002).

224. M. H. Huang, Y. Wu, H. Feick, N. Tran, E. Weber, P. Yang, Adv. Mater. **13**, 113 (2001).

225. C. Li, D. Zhang, S. Han, X. Liu, T. Tang, C. Zhou, Adv. Mater. **15**, 143 (2003).

226. Z. R. Dai, Z. W. Pan, Z. L. Wang, Solid State Commun. **118**, 351 (2001).

227. X. Y. Zhang, L. D. Zhang, W. Chen, G. W. Meng, M. J. Zheng, L. X. Zhao, Chem. Mater. **13**, 2511 (2001).

228. H. Z. Zhang, Y. C. Kong, Y. Z. Wang, X. Du, Z. G. Bai, J. J. Wang, D. Y. Yu, Y. Ding, Q. L. Hang, S. Q. Feng, Solid State Commun. **109**, 677 (1999).

229. J. Zhang, F. Jiang, L. Zhang, Phys. Lett. A **322** (2004) 363.

230. B. Geng, L. Zhang, G. Meng, T. Xie, X. Peng, Y. Lin, J. Cryst. Growth **259**, 291 (2003).

231. J. -S. Lee, K. Park, S. Nahm, S. -W. Kim, S. Kim, J. Cryst. Growth **244**, 287 (2002).

232. Y. C. Choi, W. S. Kim, Y. S. Park, S. M. Lee, D. J. Bae, Y. H. Lee, G. S. Park, W. B. Choi, N. S. Lee, J. M. Kim Adv. Mater. **12**, 746 (2000).

233. C. H. Liang, G. W. Meng, G. Z. Wang, Y. W. Wang, L. D. Zhang, Appl. Phys. Lett. **78** 3202 (2001).

234. J. Q. Hu, Q. Li, X. M. Meng, C. S. Lee, S. T. Lee, J. Phys. Chem. B **106**, 9536 (2002).

235. Y. Wu, P. Yang, J. Am. Chem. Soc. **123**, 3165 (2001).

236. J. B. Hannon, S. Kodambaka, F. M. Ross, R. M. Tromp, Nature 440, 69 (2006).

237. C. Wang, B. Wang, Y. Yang, G. Yang, Chen, J. Phys. Chem. B **109**, 9966 (2005).

238. Y. Wang, J. Xu, R. M. Wang, D. P Yu, Micron **35**, 447 (2004).

239. G. W. Zhou, Z. Zhang, Z. G. Bai, S. Q. Feng, D. P. Yu, Appl. Phys. Lett. **73**, 677 (1998).

240. H. Z. Zhang, Y. C. Kong, Y. Z. Wang, X. Du, Z. G. Bai, J. J. Wang, D. P. Yu, Y. Ding, Q. L. Hang, S. Q. Feng, Solid State Commun. **109**, 677 (1999).

241. N. H. Kim, H. W. Kim, App. Phys. A **81**, 763 (2005).

242. N. H. Kim, H. W. Kim, App. Phys. A **80**, 537 (2005).

243. H. W. Kim, N. H. Kim, C. Lee, J. of the Korean Physical Soc. **47**, S539 (2005).

244. Y. Suda, K, Utaka, M. A. Bratescu, Y. Sakai, J. Tsujina, K. Suzuki, Appl. Phys. A **79**, 1331 (2004).

245. Q. Wu, Z, Hu, C. Liu, X. Wang, Y. Chen, J. Phys. Chem. B **109**, 19719 (2005).

246. F. Wang, Z. Han, L. Tong, Physica E 30, 150 (2005).

247. Y. Tong, Y. Liu, C. Shao, Y. Liu, C. Xu, J. Zhang, Y. Lu, D. Shen, X. Fan, J. Phys. Chem. B **110**, 14714 (2006).

248. C. –K. Chao, H. –S Chang, T.-M. Hsu, C. –N. Hsiao, C. –C Kei, S. -Y. Kuo, J. –I. Chyi, Nanotechnology **17**, 3930 (2006).

APPENDIX A

LASER ABLATION OF GAN/SAPPHIRE LED STRUCTURES

A study of the laser ablation of GaN thin film and GaN/Sapphire LED structures for the application of light emitting diodes (LEDs) is demonstrated in this section. Edge quality and surface roughness of the specimens are compared using scanning electron microscopy (SEM) and non-contact surface profiler after laser processing by the 3rd harmonic Nd:YAG laser (355 nm), KrF excimer laser (248 nm) and Ti:Sapphire femtosecond laser (800 nm). Dependence of laser ablation rate and ablated depth on the processing parameters, such as laser fluence, laser scanning speed and pulse repetition rate are investigated. Device characteristics of the LED specimens after the laser microprocessing are also analyzed.

A.1 Ablation Depth Determination by Surface Profiling Measurement

Figure A.1.1 to A.1.3 depict the ablated depth of the GaN samples by 3rd Harmonic Nd:YAG, KrF excimer and Ti:Sapphire femtosecond lasers respectively. The Alpha-Step stylus profiler was used to measure the surface and ablated depth readings after laser irradiations. In all three figures, the depressions in between the two plateaus indicate the laser ablated area and the ablated depth is measured. On the other hand, the two plateaus show the areas on the samples that are unexposed to laser irradiation.

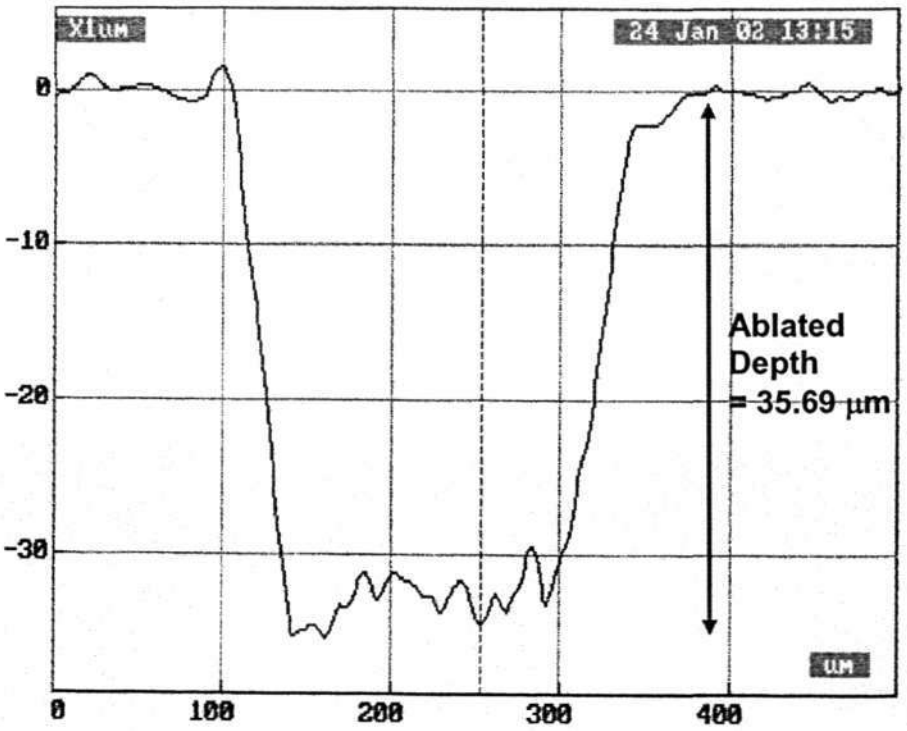

Fig. A.1.1 Surface and depth profiles of GaN sample after 3rd Harmonic Nd:YAG laser irradiation at laser fluence of 1.9 J/cm^2 and repetition rate of 5000 Hz.

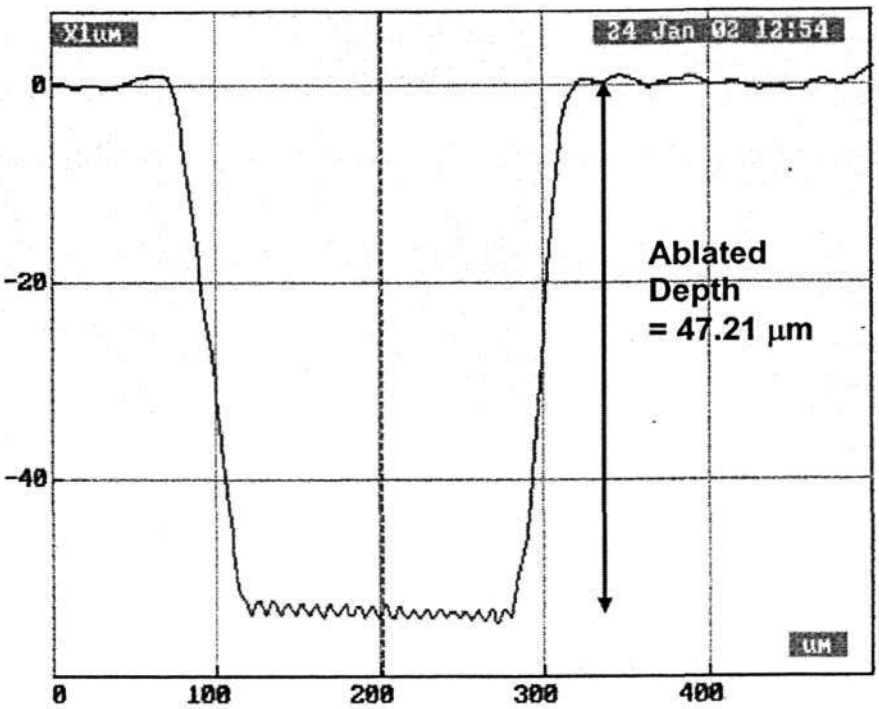

Fig. A.1.2 Surface and depth profiles of GaN sample after KrF excimer laser irradiation at laser fluence of 0.76 J/cm^2, repetition rate of 1 Hz and 300 laser pulses.

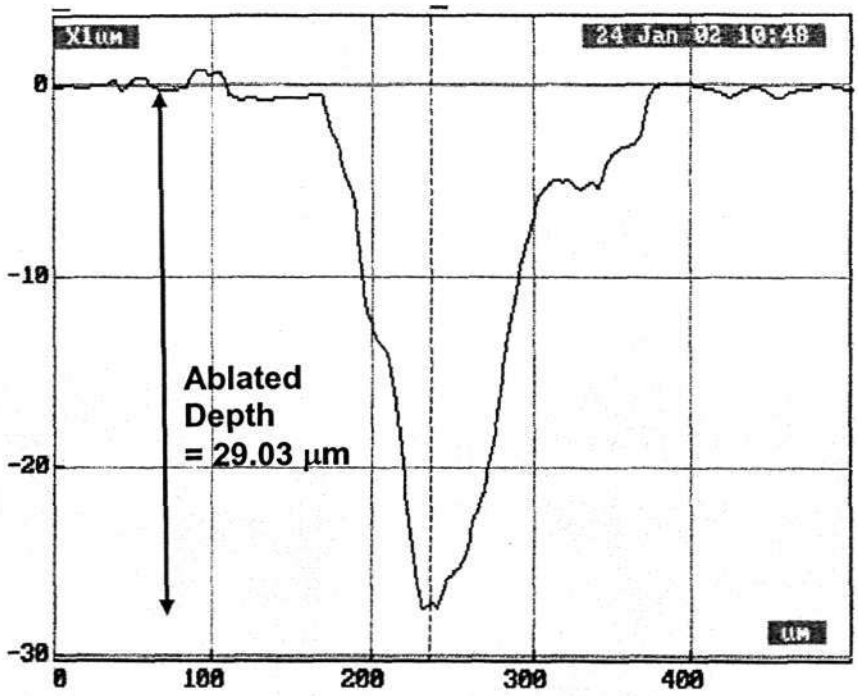

Fig. A.1.3 Surface and depth profiles of GaN sample after Ti:Sapphire femtosecond laser irradiation at laser fluence of 0.76 J/cm^2 and repetition rate of 1000 Hz.

A.2 Optical Images of GaN after KrF Excimer Irradiation

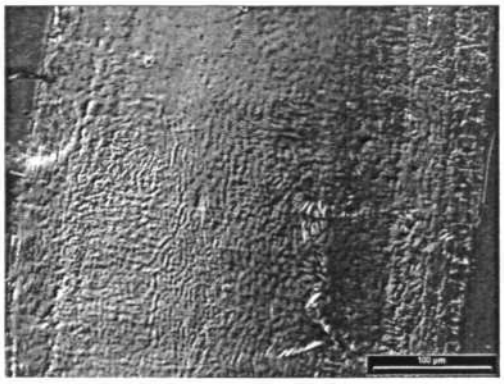

(a)

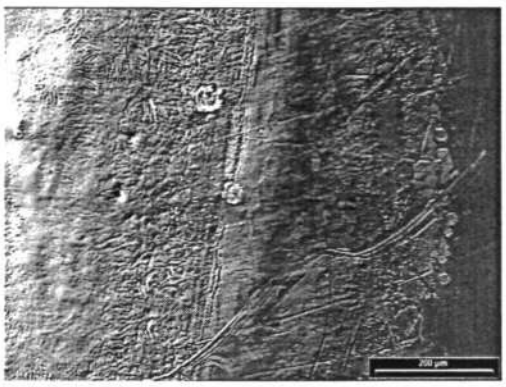

(b)

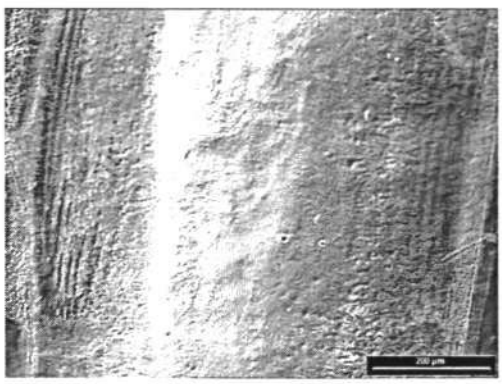

(c)

Fig. A.2.1 Optical microscopic images of GaN surface after 5 pulses of KrF excimer laser irradiation with laser energy of (a) 5 mJ/pulse, (b) 29 mJ/pulse and (c) 60 mJ/pulse.

Figure A.2.1 and A.2.2 show the optical images of the surface of GaN after KrF excimer laser ablation. Formation of Ga and Ga oxide residue (silver substance) were observed after laser ablation. KrF excimer laser has nanosecond pulses, their diffusion length is usually longer than the absorption length of GaN. Hence upon laser irradiation onto GaN thin film, due to high thermal heat generation, GaN decomposes to Ga metal and N_2. These material deposits are contributed by laser induced thermal decomposition of GaN by long pulsed UV lasers [1] and they were removed using 10% hydrochloric acid before measurement of ablation depth. It was also observed that as the laser energy per pulse and the number of laser pulses increase, surface roughness and ablation depth of GaN increases. More significant ablation was observed at higher laser fluence and when more laser pulses were irradiated at the sample surface.

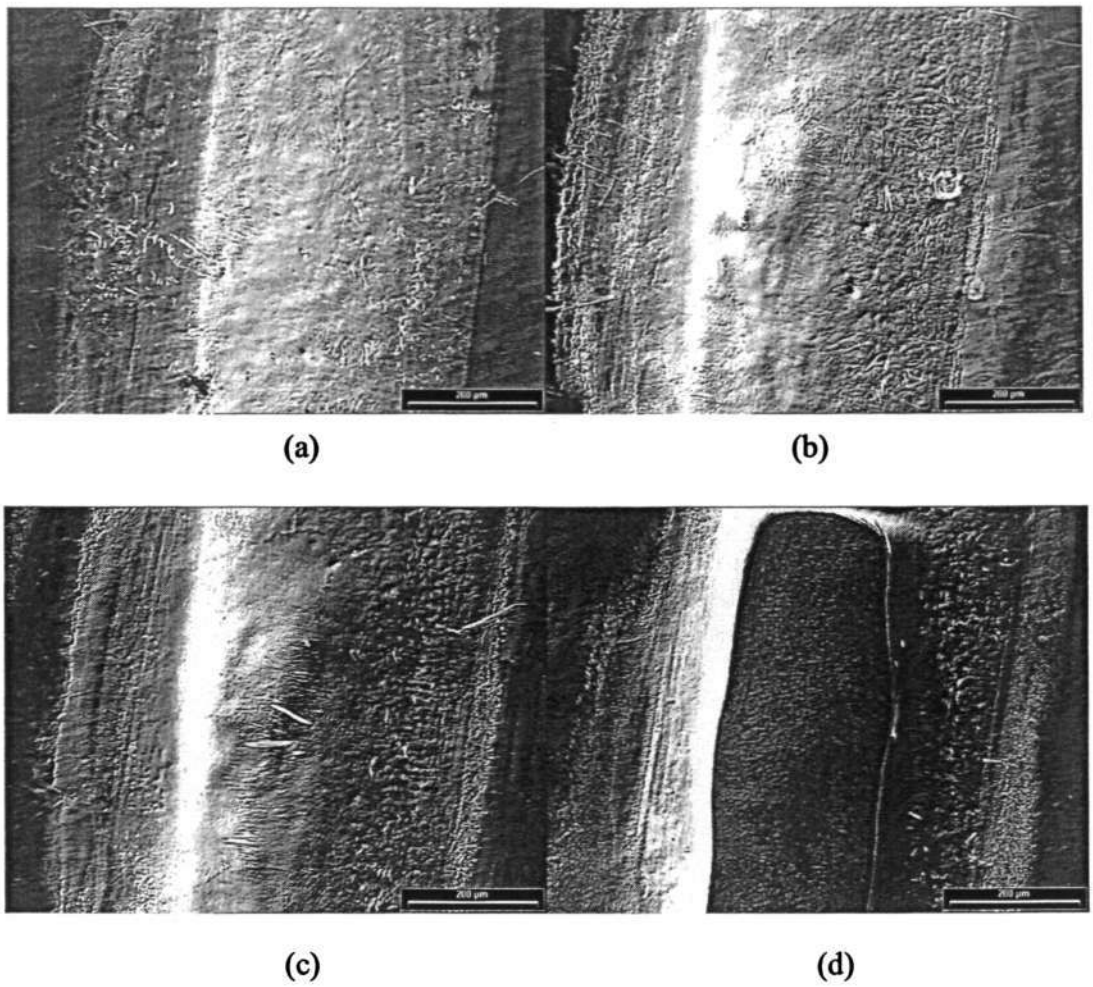

Fig. A.2.2 Optical microscopic images of GaN surface after KrF excimer laser irradiation with laser energy of 29 mJ/pulse (a) 1 pulse, (b) 5 pulses and (c) 10 pulses (d) 20 pulses.

A.3 Optical Images of GaN after 3rd Harmonic Nd:YAG Laser Irradiation

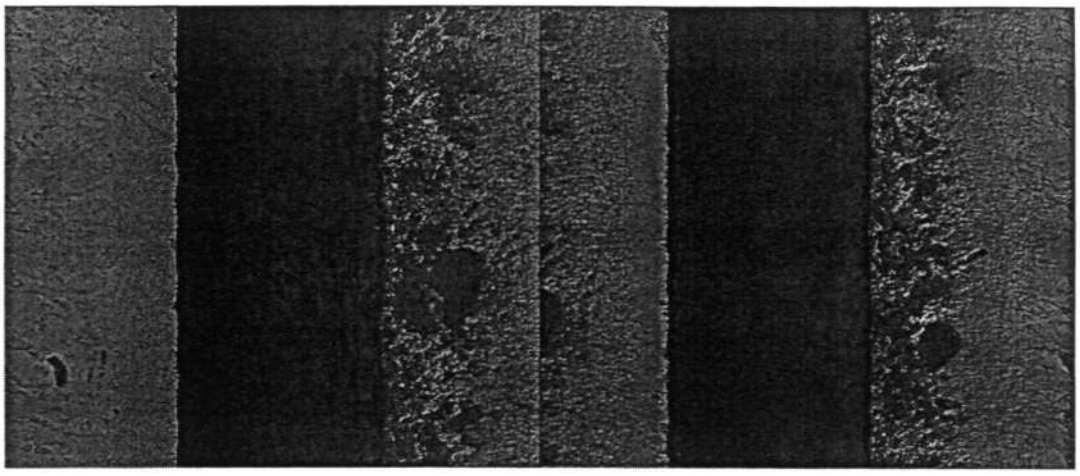

(a) (b)

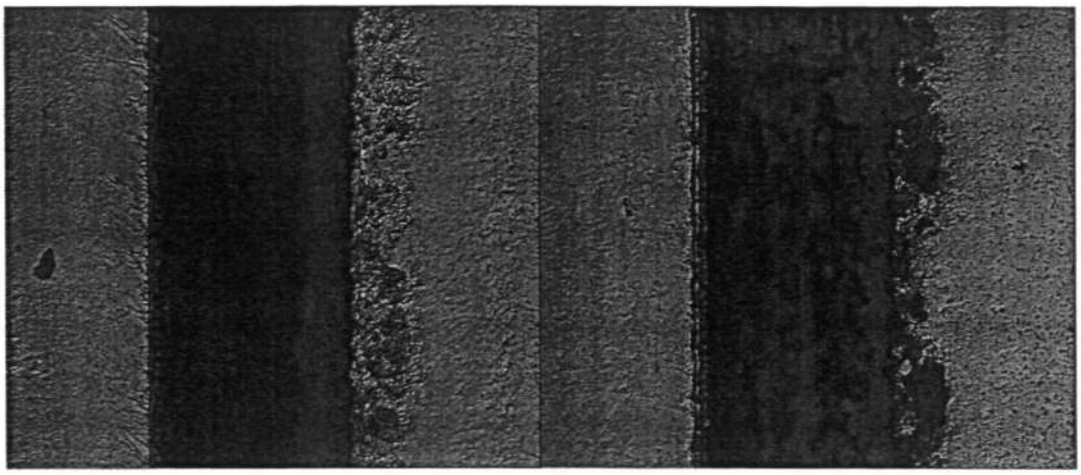

(c) (d)

Fig. A.3.1 Optical microscopic images of GaN surface after 3rd Harmonic Nd:YAG laser ablation with laser scanning speed of 4 mm/s and repetition rate of (a) 3000 Hz, (b) 5000 Hz and (c) 10, 000 Hz (d) 20, 000 Hz.

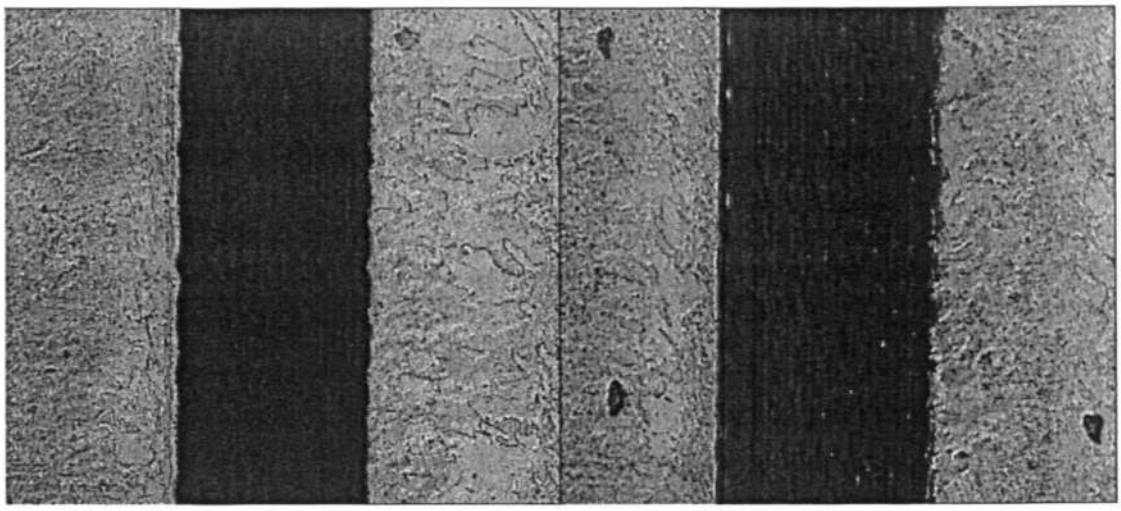

(a) (b)

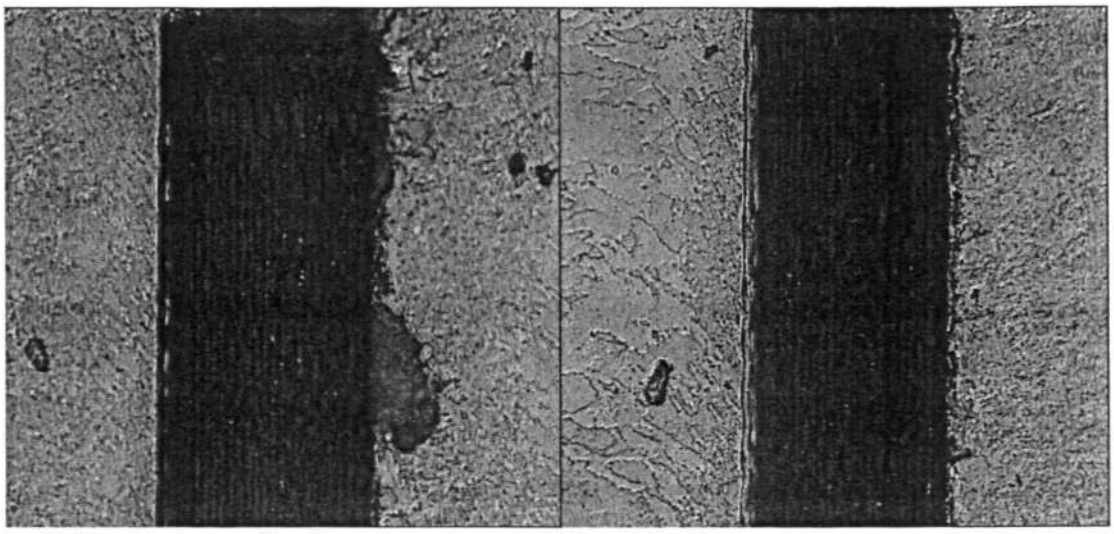

(c) (d)

Fig. A.3-2 Optical microscopic images of GaN surface after 3rd Harmonic Nd:YAG laser ablation with laser scanned speed of 4 mm/s and laser fluence of (a) 0.32 J/cm^2, (b) 2.0 J/cm^2 and (c) 2.04 J/cm^2 (d) 2.1 J/cm^2.

Figure A.3.1 and A.3.2 show the optical images of the surface of GaN after 3rd Harmonic Nd:YAG laser ablation. Formation of Ga and Ga oxide residue were not significantly observed after laser ablation as compared to KrF excimer laser ablation. The ablated surfaces showed surface melting and burning more significantly in the case of 3rd Harmonic Nd:YAG laser ablation. Similarly as repetition rates and laser fluences increase, the ablated depth also increases. Greater surface melting was also observed at higher laser fluence and repetition rate. The observation of the surface melting of GaN can be explained by the fact that the 3rd Harmonic Nd: YAG laser ablation with nanosecond pulses operates in the ns laser ablation regime. And the ns ablation mechanisms are based on the selective melting and vaporizing of the material, hence there is enough time for the thermal energy of the laser to propagate into the GaN material to create the melting effect.

A.4 Dependence of Ablation Depth on Laser Fluence

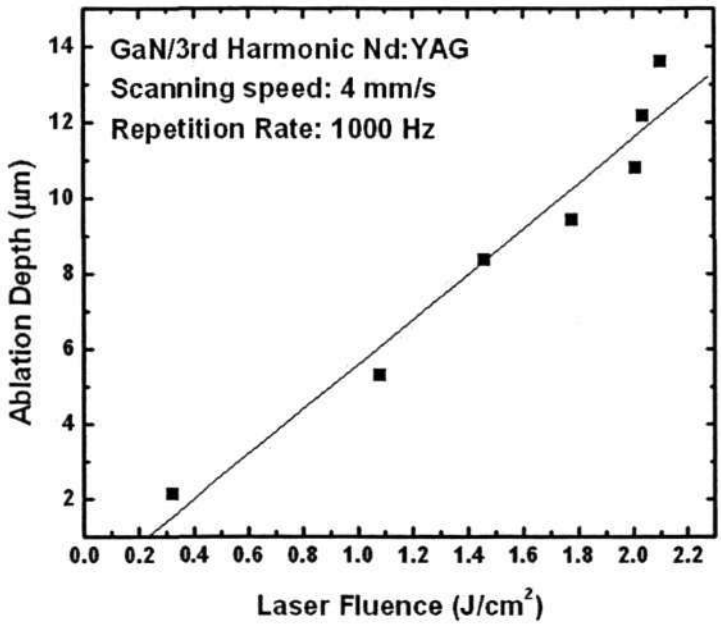

Fig. A.4.1 Plot of ablation depth as a function of laser fluence for the 3rd Harmonic Nd:YAG laser

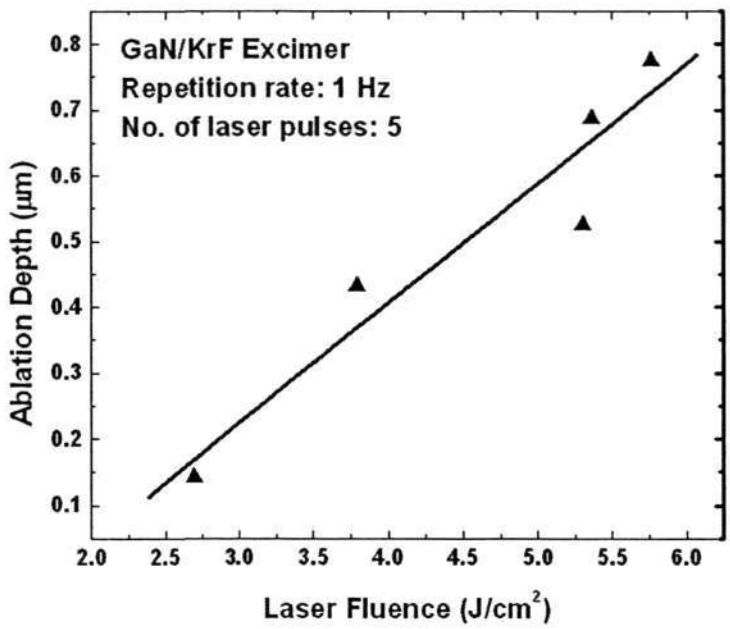

Fig. A.4.2 Plot of ablation depth as a function of laser fluence for the KrF excimer laser

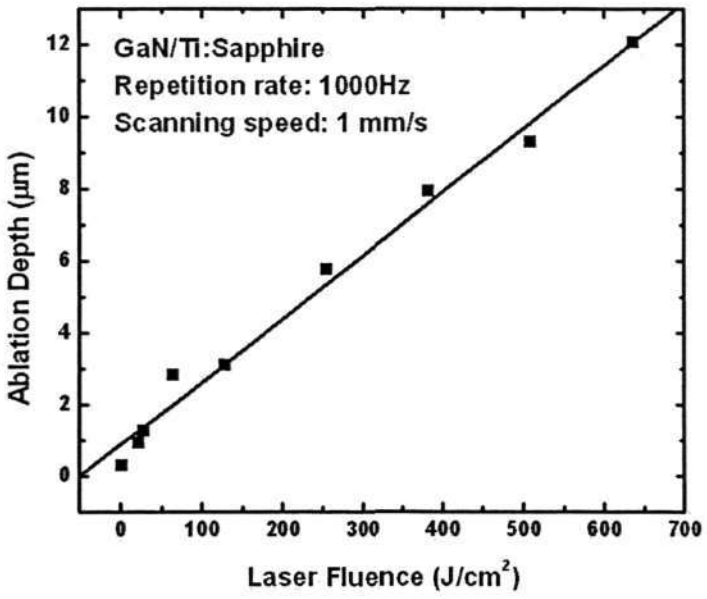

Fig. A.4.3 Plot of ablation depth as a function of laser fluence for the Ti:Sapphire laser

Figure A.4.1 to A.4.3 show the ablation depth as a function of laser fluence for 3rd Harmonic Nd:YAG, KrF excimer and Ti:Sapphire lasers respectively. From the figures, it was found that in all 3 cases, ablation depth varies linearly with laser fluence. At higher laser fluence, more significant ablation was observed, with greater ablated depth. Since laser fluence is calculated by laser energy per unit area of laser beam spot, the higher the laser energy is absorbed by the material, greater laser ablation and removal of the material would be resulted.

A.5 Dependence of Ablation Rate on Laser Fluence

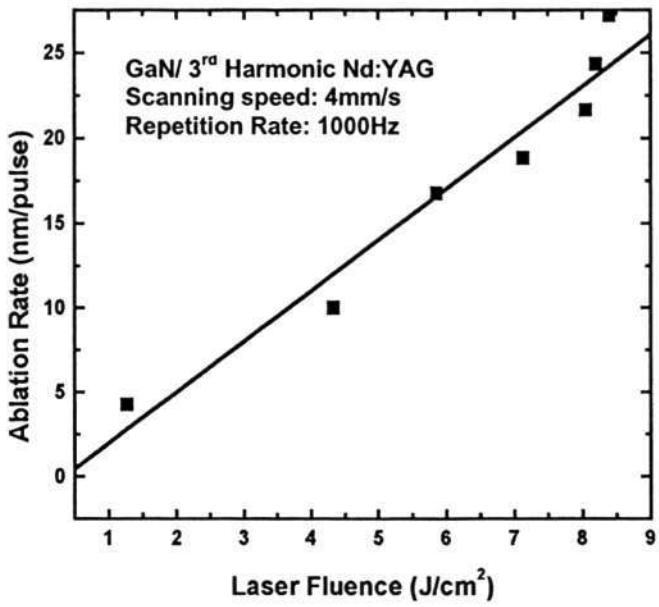

Fig. A.5.1 Plot of ablation rate as a function of laser fluence for the 3rd Harmonic Nd:YAG laser

A plot of laser ablation etch rate per pulse as a function of laser fluence of the 3rd Harmonic Nd:YAG laser is depicted in Fig. A.5.1. The laser fluence was varied between 1.2 to 8.5 J/cm^2. It was shown that ablation rate increases with increasing laser fluence. Hence, at the laser fluence of 8 J/cm^2, approximately 200 laser pulses is able to remove the 4 μm thick GaN thin film.

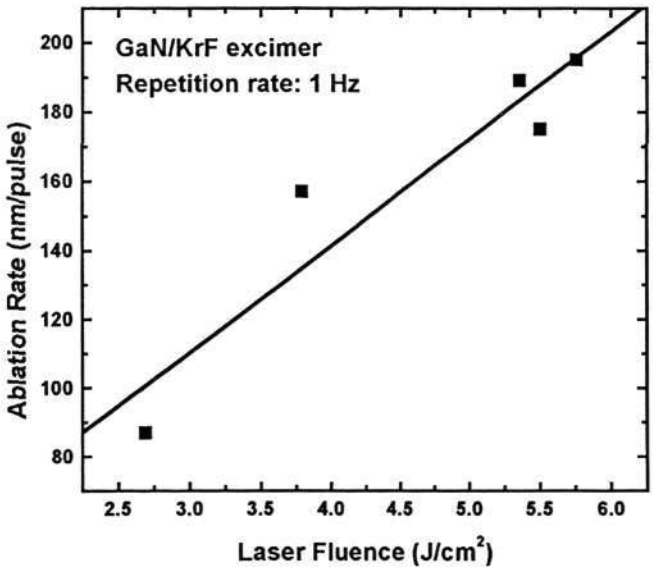

Fig. A.5.2 Plot of ablation rate as a function of laser fluence for KrF pulsed excimer laser.

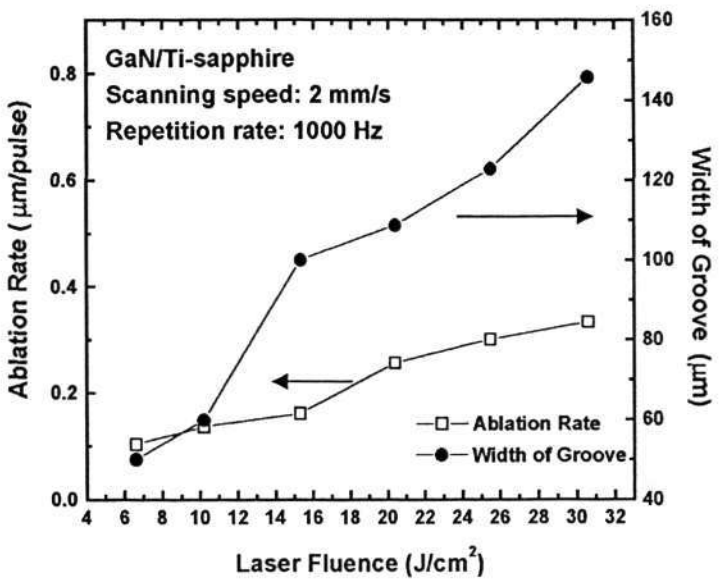

Fig. A.5.3 Plot of ablation rate as a function of laser fluence for Ti-sapphire fs laser.

Figures A.5.2 & A.5.3 show the dependence of ablation rate as a function of laser fluence using KrF excimer laser and Ti-sapphire laser respectively. In the case of KrF excimer laser ablation, 20 laser pulses will be adequate to remove 4 μm thick GaN thin film when employing the laser fluence of 5.5 J/cm^2. Here, the KrF excimer laser ablation shows higher ablation rate as compared to the 3rd Harmonic Nd:YAG laser ablation. GaN has bandgap (E_g) of 3.45 eV at room temperature, a single photon of KrF excimer laser of 4.99 eV has higher energy for photonic bond breaking of GaN compared to a single photon of the 3rd Harmonic Nd:YAG laser of 3.93 eV. This resulted in higher ablation rate by the KrF excimer laser ablation. It is also shown in Fig. 6 that as laser fluence increases, ablation rate and width of the groove increase in Ti:Sapphire laser ablation. At the laser fluence of 18 J/cm^2, 8 laser pulses will be able to totally ablate the 4 μm thick GaN layer. From these experimental results, it can be observed that Ti:Sapphire laser has the highest ablation rate, followed by the KrF excimer laser and 3rd Harmonic Nd:YAG laser ablation. Ti:Sapphire laser has pulse duration in hundreds of femtosecond scale, which is significantly shorter than the nanosecond pulse durations of the 3rd Harmonic Nd:YAG laser and KrF excimer laser. Ultrashort-pulse laser ablation of the Ti:Sapphire laser has the ability to produce higher laser intensity ($> \sim 10^{16}$ W cm^{-2}), which induces non-linear absorption in the GaN material, hence this resulted in higher ablation rate.

A.6 Dependence of Ablation Depth on Laser Pulse Number

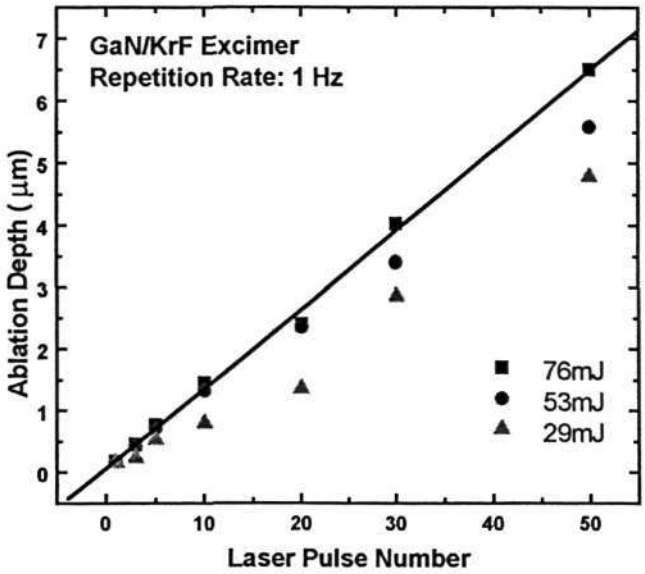

Fig. A.6.1 Plot of ablation depth as a function of laser pulse number for KrF excimer laser.

Figure A.6.1 depicts the ablation depth of GaN as a function laser pulse number after irradiation by KrF excimer laser. Three laser energies of 29 mJ/pulse, 53 mJ/pulse and lastly 76 mJ/pulse were adopted. From the figure, it can be seen that ablation depth of GaN varied linearly with the number of laser pulses. As the number of laser pulses increase, ablation depth also increases. It is also shown that as laser pulse energy increases, ablation depth is higher.

A.7 Cross-section of GaN/Sapphire structure

Cross-sections of the GaN/Sapphire structure after laser singulation were observed by scanning electron microscope (SEM). Figure A.7.1(a) & (b) show the SEM images of the GaN/Sapphire surfaces after the 3rd Harmonic Nd:YAG and Ti:Sapphire laser ablation respectively. It can be observed in Fig. A.7.1(a) that melting and cracking are evident on both the sapphire substrate and GaN thin film after laser ablation of the GaN/Sapphire LED structures using the 3rd Harmonic Nd:YAG laser at repetition rate of 5000 Hz and laser fluence of 30 mJ/cm^2. This indicates that laser induced thermal decomposition of sapphire and GaN had taken place during the laser ablation process. Similar melting and cracking effects were also observed on both sapphire and GaN thin film at other laser fluence. On the other hand, no melting and cracking effect was observed on both the sapphire substrate and GaN thin film after femtosecond laser ablation at a repetition rate of 1 kHz and 600 mW/cm^2. Since femtosecond laser ablation is initiated by multi-phonon absorption, ablation does not induce any thermal decomposition and hence no melting or cracking can occur. Hence, for better surface morphology and to minimize heat effect to the GaN LED, fs laser ablation should be adopted.

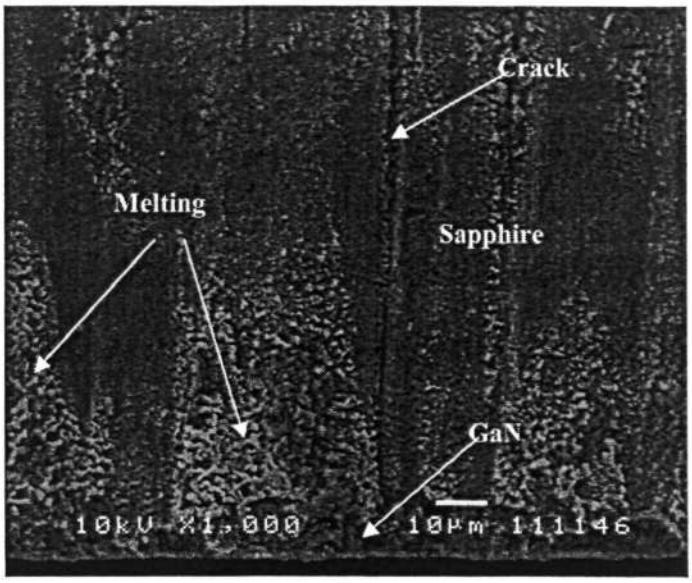

(a)

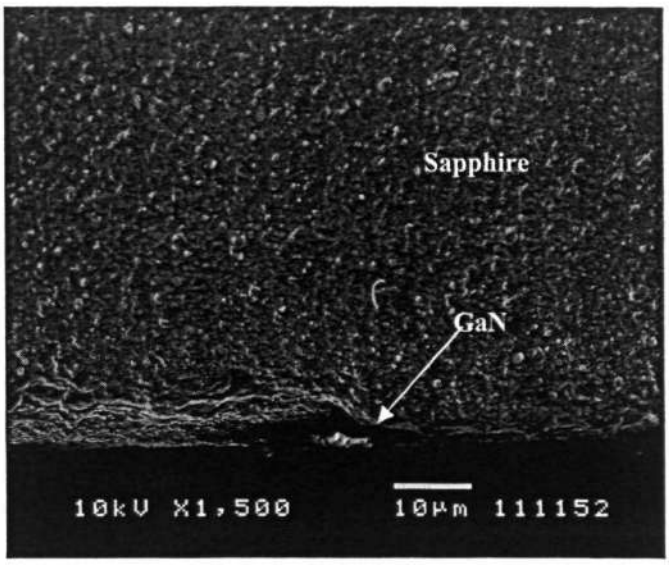

(b)

Fig. A.7.1 SEM images of GaN/Sapphire LED samples processed by the (a) 3rd Harmonic Nd:YAG laser and (b) Ti:Sapphire laser.

A.8 Surface roughness of GaN/Sapphire structure

Surface roughness measurements of the laser-ablated samples were measured using ZYGO non-contact profiler. The average surface roughness values of the samples after laser ablation using the 3rd Harmonic Nd:YAG laser and Ti:Sapphire laser are 0.89 μm and 4.13 μm respectively. Figure A.8.1(a) and (b) depicts the surface roughness plots of the 3rd Harmonic Nd:YAG laser and Ti-sapphire fs laser respectively. It was observed that the surface roughness (R_a) of the sample by the 3rd Harmonic Nd:YAG laser ablation lower R_a compared to Ti:Sapphire laser ablation. This may be attributed to greater lateral heat conduction in the GaN and sapphire materials by the 3rd Harmonic Nd:YAG laser ablation, which causes the greater melting and planarization effect. Lesser or no lateral heat conduction had occurred during femtosecond laser ablation, hence there was no planarization of the surface material and hence in the case of Ti:Sapphire laser ablation, GaN and sapphire surfaces showed higher roughness.

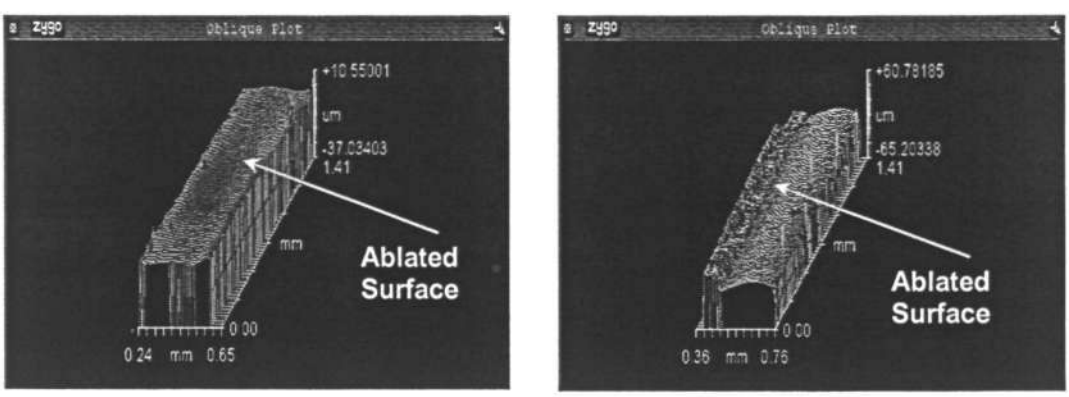

(a) (b)

Fig. A.8.1 ZYGO Oblique plots of the surface roughness of GaN/Sapphire LED samples after laser ablation by the (a) 3rd Harmonic Nd:YAG laser and (b) Ti-sapphire fs laser.

A.9 Device characteristics of GaN LED

The samples after laser ablation by the 3rd Harmonic Nd:YAG laser and femtosecond laser were subsequently used to fabricate GaN LED. Optical lithography was performed for P and N-type ohmic contacts. E-beam evaporation of Pd/Ni/Au and Ti/Al/Au were carried for P-type and N-type ohmic contacts respectively. To evaluate whether laser ablation will affect the p-n junction of the GaN LED, current-voltage (I-V) characteristics of the samples were investigated. A typical I-V curve (Fig. A.9.1) was obtained which did not show any breakdown. However, a low turn-on voltage of 1 V was obtained as compared to a typical turn-on voltage of 2.5 to 3 V of a normal LED. The low turn-on voltage could be due to the occurrence of leakage current in the device. At the same time, this result also shows that laser cutting has not damaged the p-n junction of the GaN LED and this process can be applied for GaN LED processing with better control in the fabrication process to reduce the leakage current in the device. In order to further evaluate the quality of GaN LED fabricated by laser processing, more data such as photoluminescence and electroluminscence of the samples have to be carried out.

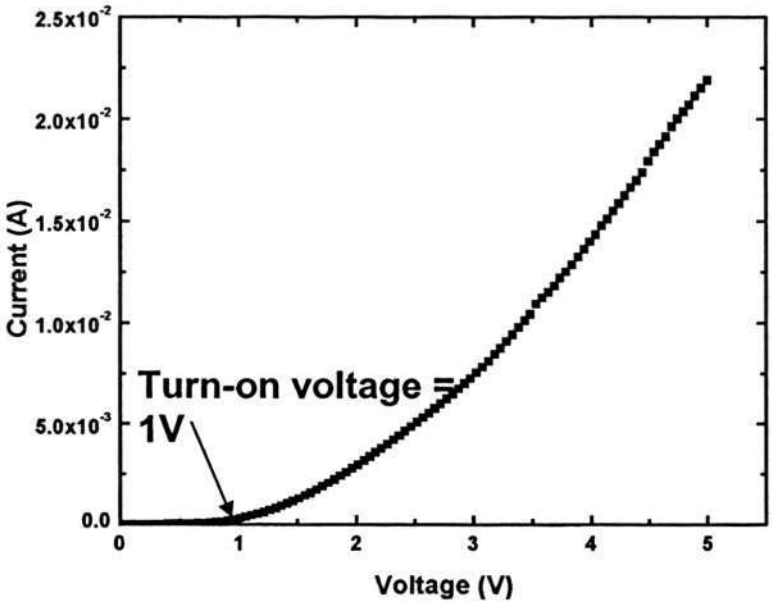

Fig. A.9.1 I-V characteristics for an InGaN (MQW) LED structure. The turn-on voltage is 1 V.

A.10 Summary

The 3rd harmonic Nd:YAG laser, KrF excimer laser and Ti:Sapphire laser ablation of GaN/Sapphire structure have been investigated and comparatively studied. Ga and Ga oxide were found after laser ablation by the 3rd harmonic Nd:YAG laser and KrF excimer laser microprocessing. This shows thermal decomposition of GaN by 3rd harmonic Nd:YAG laser and KrF excimer laser ablation. Conversely, Ti:Sapphire laser ablation indicates a non-thermal laser ablation process. In addition, Ti:Sapphire laser ablation has also showed the highest ablation rate of GaN followed by the KrF excimer laser then 3rd harmonic Nd:YAG laser. Greater surface roughness of GaN due to no lateral heat conduction and planarization effect was also observed in the Ti:Sapphire laser ablation as compared to the 3rd harmonic Nd:YAG laser ablation. Device characteristics are also subsequently investigated after the fabrication of GaN LED and a typical I-V curve of the GaN LED was obtained. This indicates that laser ablation by both the 3rd harmonic Nd:YAG laser and Ti:Sapphire laser had not affected the p-n junction of the GaN LED. Hence, pulse laser ablation proves to be viable for laser processing in microelectronics and optoelectronics applications. For higher ablation rate, better edge quality, and to minimize thermal effects to the device, Ti:Sapphire femtosecond laser ablation should be employed.